

UNIVERSITY OF ILLINOIS
AT CHICAGO

Department of Physics (MC 273)
845 West Taylor Street, Room 2236
Chicago, Illinois 60607-7059

(312) 996-4868 (Voice)
(312) 996-8824 (Fax)
e-mail: rhodes@uic.edu

11 December 2000

Mrs. Sylvia Hall
U.S. Army Research Office
P.O. Box 12211
Research Triangle Park, NC 27709-2211
Attn: AMSRL-RO-RI (Hall)

Memorandum

Re: DAAD 19-99-97-1-0052

Dear Ms. Hall:

Herein please find our Final Progress Report for the contract cited above, "Advanced Computational Physics Instrumentation," awarded from 03/01/99 to 08/31/99.

Very truly yours,



Charles K. Rhodes

bp/CKR
enc

DTIC QUALITY INDEX 4

20010116 132

UIC

Phone (312) 996-3400 • Fax (312) 996-9016

REPORT DOCUMENTATION PAGE

Form Approved
OMB NO. 0704-0188

Public reporting burden for this collection of information is estimated to average 1 hour per response, including the time for reviewing instructions, searching existing data sources, gathering and maintaining the data needed, and completing and reviewing the collection of information. Send comment regarding this burden estimate or any other aspect of this collection of information, including suggestions for reducing this burden, to Washington Headquarters Services, Directorate for Information Operations and Reports, 1215 Jefferson Davis Highway, Suite 1204, Arlington, VA 22202-4302, and to the Office of Management and Budget, Paperwork Reduction Project (0704-0188), Washington, DC 20503.

1. AGENCY USE ONLY (Leave blank)		2. REPORT DATE 11 December 2000	3. REPORT TYPE AND DATES COVERED FINAL 01 MAR 99 – 31 AUG 00
4. TITLE AND SUBTITLE ADVANCED COMPUTATIONAL PHYSICS INSTRUMENTATION		5. FUNDING NUMBERS DAAD19-99-1-0052	
6. AUTHOR(S) Dr. Charles K. Rhodes			
7. PERFORMING ORGANIZATION NAMES(S) AND ADDRESS(ES) UNIVERSITY OF ILLINOIS AT CHICAGO Physics Department (m/c 273) 845 West Taylor Street Chicago, IL 60607-7059		8. PERFORMING ORGANIZATION REPORT NUMBER 2-5-30911 (If not, call John Ward at 312-996-5958)	
9. SPONSORING / MONITORING AGENCY NAME(S) AND ADDRESS(ES) U.S. Army Research Office P.O. Box 12211 Research Triangle Park, NC 27709-2211		10. SPONSORING / MONITORING AGENCY REPORT NUMBER ARO 39347.1-PH-RIP	
11. SUPPLEMENTARY NOTES The views, opinions and/or findings contained in this report are those of the author(s) and should not be construed as an official Department of the Army position, policy or decision, unless so designated by other documentation.			
12a. DISTRIBUTION / AVAILABILITY STATEMENT Approved for public release; distribution unlimited.		12 b. DISTRIBUTION CODE	
13. ABSTRACT (Maximum 200 words) An advanced program in Computational Physics can conduct research in physics, educate students in broad areas of physics and computational technology, and be responsive to needs of the Department of Defense. The first serves the Departmental mission, the second gives the preparation for careers in physics or in informational technology (IT), and the third advances our military preparedness. We note that the IT sector currently has approximately one million unfilled opportunities in the United States. Three areas of computationally based research have been selected with these criteria. They are (1) power compression technology, specifically the study of ultrahigh ($\sim 10^{21}$ W/cm ³) power densities, (2) basic physical interactions, which has potential applications to navigation and code-breaking, and (3) protein dynamics, an area related to new potentialities in defense against biological attack. The computational equipment associated with this program have yielded results on (A) the stability of self-trapped plasma channels produced with intense femtosecond ultraviolet (248 nm) pulses, (B) the mechanism of gamma-ray bursts, (C) the fusion of the concepts of mass and space, and (D) the potential existence of a new organizing principle in biology that has a direct physical counterpart in the group structure of elementary particle states.			
14. SUBJECT TERMS Computational Physics Plasmas X-rays Cosmology			15. NUMBER OF PAGES
			16. PRICE CODE
17. SECURITY CLASSIFICATION OR REPORT UNCLASSIFIED	18. SECURITY CLASSIFICATION OF THIS PAGE UNCLASSIFIED	19. SECURITY CLASSIFICATION OF ABSTRACT UNCLASSIFIED	20. LIMITATION OF ABSTRACT UL

MEMORANDUM OF TRANSMITTAL

U.S. Army Research Office
ATTN: AMSRL-RO-RI (Hall)
P.O. Box 12211
Research Triangle Park, NC 27709-2211

Reprint (Orig + 2 copies) Technical Report (Orig + 2 copies)
 Manuscript (1 copy) Final Progress Report (Orig + 2 copies)
 Related Materials, Abstracts, Theses (1 copy)

CONTRACT/GRANT NUMBER: DAAD 19-99-97-1-0052

REPORT TITLE: ADVANCED COMPUTATIONAL PHYSICS INSTRUMENTATION

is forwarded for your information.

SUBMITTED FOR PUBLICATION TO (applicable only if report is manuscript):

**DO NOT REMOVE LABEL BELOW
FOR IDENTIFICATION PURPOSES**

Sincerely,



Dr. Charles K. Rhodes
Dept. of Physics (MC 273)
University of Illinois at Chicago
845 West Taylor St., Room 2236
Chicago, IL 60607-7059

11 December 2000

FINAL PROGRESS REPORT

DAAD 19-99-97-1-0052

Advanced Computational Physics Instrumentation

Award Dates: 01 March 1999 – 31 August 1999

(3) LIST OF APPENDICES

1. "Bifurcation Mode of Relativistic and Charge-Displacement Self-Channeling," A. B. Borisov, S. Cameron, T. S. Luk, T. R. Nelson, A. Van Tassle, J. Santoro, W. A. Schroeder, Y. Dai, J. W. Longworth, K. Boyer, and C. K. Rhodes, submitted to *J. Phys. B*, May, 2000.
2. "Gamma-Ray Bursts and the Particle Mass Scale," Yang Dai, Alex B. Borisov, James W. Longworth, Keith Boyer, and Charles K. Rhodes. *Proceedings of the International Conference on Electromagnetics in Advanced Applications*, edited by R. Graglia (Politecnico di Torino, Torino, Italy, 1999) p. 3.
3. "Computation with Inverse States in a Finite Field F_{p_a} : The Muon Neutrino Mass, the Unified Strong-Electroweak Coupling Constant, and the Higgs Mass," Y. Dai, A. B. Borisov, K. Boyer, and C. K. Rhodes, Sandia National Laboratories, Report SAND2000-2043, August, 2000.
4. "An Efficient, Selective Collisional Ejection Mechanism for Inner-Shell Population Inversion in Laser Driven Plasmas," W. A. Schroeder, T. R. Nelson, A. B. Borisov, J. W. Longworth, K. Boyer, and C. K. Rhodes, *J. Phys. B*, in press.
5. "L-shell Emission from High Z-solid Targets by Selective Inner-shell Collisional Electron Ejection," T. R. Nelson, A. B. Borisov, K. Boyer, S. Cameron, J. W. Longworth, T. S. Luk, A. McPherson, W. A. Schroeder, J. Santoro, A. Van Tassle, and C. K. Rhodes submitted to *J. Phys. B*, December, 2000.

(4) STATEMENT OF PROBLEM STUDIED

Three computationally intensive problem area were studied. They are (A) power compression in materials, particularly self-trapped plasma channels [1], (B) the phenomenon of γ -ray bursts [2] and the relationship to the particle mass spectrum [3], and (C) the potential role of a new organizing principle in the regulation of biological processes.

(5) SUMMARY OF THE MOST IMPORTANT RESULTS

A. Power Compression (See Appendix 1).

Stable self-channeling of ultra-powerful ($P_0 \sim 1 \text{ TW} - 1 \text{ PW}$) laser pulses in dense plasmas is a key process for many applications requiring the controlled compression of power at high levels. Theoretical computations predict that the transition zone between the stable and highly unstable regimes of relativistic/charge-displacement self-channeling is well characterized by a form of weakly unstable behavior that involves bifurcation of the propagating energy into two powerful channels. Recent observations of channel instability with femtosecond 248 nm pulses reveal a mode of bifurcation that corresponds well to these theoretical predictions. It is further experimentally shown that the use of a suitable longitudinal gradient in the plasma density can eliminate this unstable behavior and restore the efficient formation of stable channels.

B. Gamma-Ray Bursts and Elementary Particle States

1. Gamma-Ray Burst Analysis (See Appendix 2).

A mode of detonation for neutron stars is derived based on a physically defined power residue counting system used to construct a particle mass scale that reflects supersymmetric fermion/boson pairing. Neutron stars with specific mass values (M_n) can become unstable toward decay into an ensemble of highly energetic pairs of supersymmetric particles with an energy release whose upper bound can approach the rest mass energy of the original body. The subsequent scattering of these particles provides a way to account for (1) the high radiative yield ($\sim 10^{43}$ - 10^{47} J) of gamma-ray bursts, (2) the large variability of their observed energy, and (3) the expected collateral production of ultrahigh energy cosmic rays. The joint action of (a) supersymmetric classification and (b) a new arithmetic selection rule designated as congruence conservation governs the condition of instability and the dynamic participation of the magnetic monopole obviates baryon number conservation. The decay patterns of certain elementary particles and putative supermassive forms of cosmological dark matter may be subject to similar conditions. Specifically, the analysis predicts the existence of a super-light boson neutrino ν_1 that plays a fundamental role in weak interactions and it is conjectured that the phenomenon of lepton number conservation is isomorphic to the supersymmetric conservation of congruence. The ν_1 boson also provides (i) a potential basis for the CP violation observed in K_L^0 decay and (ii) an alternative description of the attribute of strangeness. These interpretations support the conclusion that the observations of gamma-ray bursts signal the existence of a radically new organizing principle of physical interactions that defines a general condition of stability for massive particles and expresses the unstable case with the copious production of energetic emissions.

2. Elementary Particle States (See Appendix 3).

The construction of inverse states in a finite field F_{P_α} enables the organization of the mass scale with fundamental octets in an eight-dimensional index space that identifies particle states with residue class designations. Conformance with both CPT invariance and the concept of supersymmetry follows as a direct consequence of this formulation. Based on two parameters (P_α and g_α) that are anchored on a concordance of physical data, this treatment leads to (1) a prospective mass for the muon neutrino of ~ 27.68 meV, (2) a value of the unified strong-electroweak coupling constant $\alpha^* = (34.26)^{-1}$ that is physically defined by the ratio of the electron neutrino and muon neutrino masses, and (3) a seesaw congruence connecting the Higgs, the electron neutrino, and the muon neutrino masses. Specific evaluation of the masses of the corresponding supersymmetric Higgs pair reveals that both particles are superheavy ($> 10^{18}$ GeV). No renormalization of the Higgs masses is introduced, since the calculational procedure yielding their magnitudes is intrinsically divergence-free. Further, the Higgs fulfills its conjectured role through the seesaw relation as the particle defining the origin of all particle masses, since the electron and muon neutrino systems, together with their supersymmetric partners, are the generators of the mass scale and establish the corresponding index space. Finally, since the computation of the Higgs masses is entirely determined by the modulus of the field P_α , which is fully defined by the large-scale parameters of the universe through the value of the universal gravitational constant G and the requirement for perfect flatness ($\Omega = 1.0$), the seesaw congruence fuses the concepts of mass and space and creates a new unified archetype. On the basis of new data from the Super-Kamiokande Collaboration [4], this analysis has been extended to give prospective values for the electron, muon, and tau neutrinos as given below.

Tau Neutrinos Favored over Sterile Neutrinos in Atmospheric Muon Neutrino Oscillations

S. Fukuda,¹ Y. Fukuda,¹ M. Ishitsuka,¹ Y. Itow,¹ T. Kajita,¹ J. Kameda,¹ K. Kaneyuki,¹ K. Kobayashi,¹ Y. Koshio,¹ M. Miura,¹ S. Moriyama,¹ M. Nakahata,¹ S. Nakayama,¹ Y. Obayashi,¹ A. Okada,¹ K. Okumura,¹ N. Sakurai,¹ M. Shiozawa,¹ Y. Suzuki,¹ H. Takeuchi,¹ Y. Takeuchi,¹ T. Toshito,¹ Y. Totsuka,¹ S. Yamada,¹ M. Earl,² A. Habig,^{2,*} E. Kearns,² M. D. Messier,² K. Scholberg,² J. L. Stone,² L. R. Sulak,² C. W. Walter,² M. Goldhaber,³ T. Barszczak,⁴ D. Casper,⁴ W. Gajewski,⁴ W. R. Kropp,⁴ S. Mine,⁴ L. R. Price,⁴ M. Smy,⁴ H. W. Sobel,⁴ M. R. Vagins,⁴ K. S. Ganezer,⁵ W. E. Keig,⁵ R. W. Ellsworth,⁶ S. Tasaka,⁷ A. Kibayashi,⁸ J. G. Learned,⁸ S. Matsuno,⁸ D. Takemori,⁸ Y. Hayato,⁹ T. Ishii,⁹ T. Kobayashi,⁹ K. Nakamura,⁹ Y. Oyama,⁹ A. Sakai,⁹ M. Sakuda,⁹ O. Sasaki,⁹ M. Kohama,¹⁰ A. T. Suzuki,¹⁰ T. Inagaki,¹¹ K. Nishikawa,¹¹ T. J. Haines,^{12,4} E. Blaufuss,¹³ B. K. Kim,¹³ R. Sanford,¹³ R. Svoboda,¹³ M. L. Chen,¹⁴ J. A. Goodman,¹⁴ G. Guillian,¹⁴ G. W. Sullivan,¹⁴ J. Hill,¹⁵ C. K. Jung,¹⁵ K. Martens,¹⁵ M. Malek,¹⁵ C. Mauger,¹⁵ C. McGrew,¹⁵ E. Sharkey,¹⁵ B. Viren,¹⁵ C. Yanagisawa,¹⁵ M. Kirisawa,¹⁶ S. Inaba,¹⁶ C. Mitsuda,¹⁶ K. Miyano,¹⁶ H. Okazawa,¹⁶ C. Saji,¹⁶ M. Takahashi,¹⁶ M. Takahata,¹⁶ Y. Nagashima,¹⁷ K. Nitta,¹⁷ M. Takita,¹⁷ M. Yoshida,¹⁷ S. B. Kim,¹⁸ T. Ishizuka,¹⁹ M. Etoh,²⁰ Y. Gando,²⁰ T. Hasegawa,²⁰ K. Inoue,²⁰ K. Ishihara,²⁰ T. Maruyama,²⁰ J. Shirai,²⁰ A. Suzuki,²⁰ M. Koshiiba,²¹ Y. Hatakeyama,²² Y. Ichikawa,²² M. Koike,²² K. Nishijima,²² H. Fujiyasu,²³ H. Ishino,²³ M. Morii,²³ Y. Watanabe,²³ U. Golebiewska,²⁴ D. Kielczewska,^{24,4} S. C. Boyd,²⁵ A. L. Stachyra,²⁵ R. J. Wilkes,²⁵ and K. K. Young^{25,†}
(Super-Kamiokande Collaboration)

The previously published atmospheric neutrino data did not distinguish whether muon neutrinos were oscillating into tau neutrinos or sterile neutrinos, as both hypotheses fit the data. Using data recorded in 1100 live days of the Super-Kamiokande detector, we use three complementary data samples to study the difference in zenith angle distribution due to neutral currents and matter effects. We find no evidence favoring sterile neutrinos, and reject the hypothesis at the 99% confidence level. On the other hand, we find that oscillation between muon and tau neutrinos suffices to explain all the results in hand.

PACS numbers: 14.60.Pq, 96.40.Tv

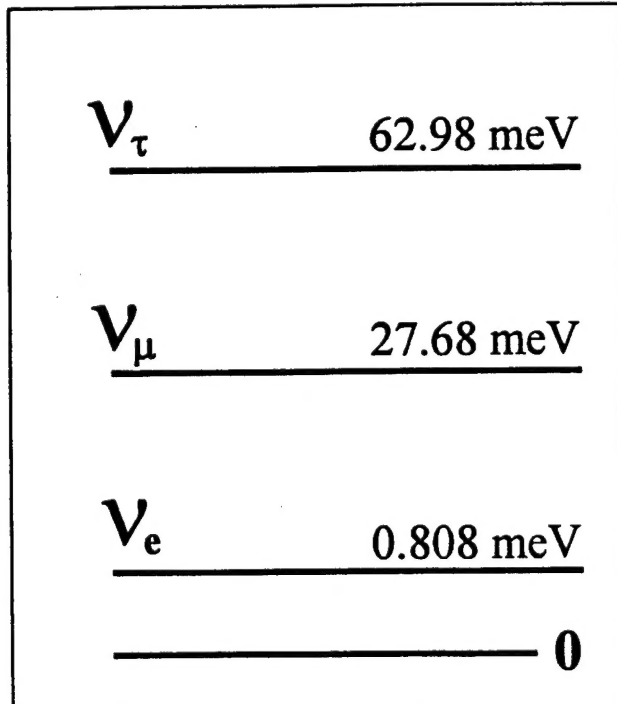
$$\delta m^2 = m_\tau^2 - m_\mu^2$$

$$\delta m^2 = 3.2 \times 10^{-3} \text{ (eV}^2)$$

(MEASUREMENT)

$$m_\mu = 27.68 \times 10^{-3} \text{ eV}$$

$m_\tau = 62.98 \text{ meV}$



C. Biological Processes

A genetic analogy linking the physical mass states of elementary systems with biological process has been developed. Specifically, the subgroup structure of the mass states [5] suggests a direct link with the large-scale organization of metabolic networks [6]. A connection to the dynamics of the p53 tumor-suppressor gene [7] is also seen. A statement [5] concerning the genetic analogy is given below.

Arithmetic conditions between particle masses can be defined on the basis of (1) the supersymmetric conservation of congruence and (2) the observed characteristics of particle reactions and stability. Stated in the form of common divisors, these relations can be interpreted as expressions of genetic elements that represent elementary particle characteristics. In order to illustrate this concept, it is shown that the pion triplet (π^{\pm}, π^0) can be identified by the existence of a common divisor d_{tot} in a way that can also account for the observed π^{\pm}/π^0 mass splitting. The results indicate that a corresponding statement may also hold for all particle multiplets. Classification of the respective physical states is achieved by association of the common divisors with residue class designations in a finite field \mathbb{F}_{p_a} and the existence of the multiplicative group of units $\mathbb{F}_{p_a}^*$ enables the corresponding mass parameters to be associated with a rich subgroup structure. It is further shown that the fundamental source of supersymmetry can be expressed in terms of hierarchical relationships between odd and even order subgroups of $\mathbb{F}_{p_a}^*$, an outcome that reflects itself in the phenomenon of fermion/boson pairing of individual particle systems. Accordingly, supersymmetry is a group rather than a particle property. The status of the Higgs subgroup of order 4 is singular; it is isolated from the hierarchical pattern and communicates globally to the mass scale through the seesaw congruence by specifying the generators of the physical masses.

(6) LIST OF PUBLICATIONS

1. "Bifurcation Mode of Relativistic and Charge-Displacement Self-Channeling," A. B. Borisov, S. Cameron, T. S. Luk, T. R. Nelson, A. Van Tassle, J. Santoro, W. A. Schroeder, Y. Dai, J. W. Longworth, K. Boyer, and C. K. Rhodes, submitted to *J. Phys. B*, May, 2000.
2. "An Efficient, Selective Collisional Ejection Mechanism for Inner-Shell Population Inversion in Laser Driven Plasmas," W. A. Schroeder, T. R. Nelson, A. B. Borisov, J. W. Longworth, K. Boyer, and C. K. Rhodes, *J. Phys. B*, in press.
3. "L-shell Emission from High Z-solid Targets by Selective Inner-shell Collisional Electron Ejection," T. R. Nelson, A. B. Borisov, K. Boyer, S. Cameron, J. W. Longworth, T. S. Luk, A. McPherson, W. A. Schroeder, J. Santoro, A. Van Tassle, and C. K. Rhodes submitted to *J. Phys. B*, December, 2000.
4. "Gamma-Ray Bursts and the Particle Mass Scale," Yang Dai, Alex B. Borisov, James W. Longworth, Keith Boyer, and Charles K. Rhodes. Proceedings of the International Conference on Electromagnetics in Advanced Applications, edited by R. Graglia (Politecnico di Torino, Torino, Italy, 1999) p. 3.
5. "Computation with Inverse States in a Finite Field \mathbb{F}_{p_a} : The Muon Neutrino Mass, the Unified Strong-Electroweak Coupling Constant, and the Higgs Mass," Y. Dai, A. B. Borisov, K. Boyer, and C. K. Rhodes, Sandia National Laboratories, Report SAND2000-2043, August, 2000.

(7) PARTICIPATING SCIENTIFIC PERSONNEL

Charles K. Rhodes

Keith Boyer

Alexey B. Borisov

Yang Dai

Thomas R. Nelson

Yi Wang

Aaron Van Tassle

(8) INVENTIONS

No inventions reported.

(9) BIBLIOGRAPHY

1. A. B. Borisov, J. W. Longworth, K. Boyer, and C. K. Rhodes, "Stable Relativistic/Charge Displacement Channels in Ultrahigh Power Density ($\sim 10^{21}$ W/cm³) Plasmas, *Proc. Natl. Acad. Sci. USA* **95**, 7854 (1998).
2. Y. Dai, A. B. Borisov, J. W. Longworth, K. Boyer, and C. K. Rhodes, "Gamma-Ray Bursts and the Particle Mass Scale," *Proceedings of the International Conference on Electromagnetics in Advanced Applications*, edited by R. Graglia (Politecnico di Torino, 1999), p. 3.
3. Y. Dai, A. B. Borisov, K. Boyer, and C. K. Rhodes, "Computation with Inverse States in a Finite Field \mathbb{F}_{p_a} : The Muon Neutrino Mass, the Unified Strong-Electroweak Coupling Constant, and the Higgs Mass," Sandia National Laboratories, Report SAND2000-2043, August, 2000.
4. S. Pukuda et al., "Tau Neutrinos Favored over Sterile Neutrinos in Atmospheric Muon Neutrino Oscillations," *Phys. Rev. Lett.* **85**, 3999 (2000).
5. Y. Dai, A. B. Borisov, K. Boyer, and C. K. Rhodes, "Determination of Supersymmetric Physical Masses with Genetic Divisors," manuscript in preparation.

(10) APPENDICES (SEE ATTACHED.)

Appendix 1

Bifurcation Mode of Relativistic and Charge-Displacement Self-Channeling

A. B. Borisov¹, S. Cameron², T. S. Luk², T. R. Nelson^{1,2}, A. J. Van Tassle¹, J. Santoro¹, W. A. Schroeder¹, Y. Dai^{1,3}, J. W. Longworth^{1,4}, K. Boyer¹, and C. K. Rhodes¹

¹ Department of Physics (M/C 273),
University of Illinois at Chicago,
Chicago, IL 60607-7059, USA

² Sandia National Laboratories,
Albuquerque, NM 87185, USA

³Department of Mathematical and Computing Sciences,
Tokyo Institute of Technology,
O-Okayama, Meguro-ku, Tokyo 152-8552, JAPAN

⁴Department of Physics,
Illinois Institute of Technology,
Chicago, IL 60616, USA

ABSTRACT

Stable self-channeling of ultra-powerful ($P_0 \sim 1$ TW - 1 PW) laser pulses in dense plasmas is a key process for many applications requiring the controlled compression of power at high levels. Theoretical computations predict that the transition zone between the stable and highly unstable regimes of relativistic/charge-displacement self-channeling is well characterized by a form of weakly unstable behavior that involves bifurcation of the propagating energy into two powerful channels. Recent observations of channel instability with femtosecond 248 nm pulses reveal a mode of bifurcation that corresponds well to these theoretical predictions. It is further experimentally shown that the use of a suitable longitudinal gradient in the plasma density can eliminate this unstable behavior and restore the efficient formation of stable channels.

I. INTRODUCTION

Robust stability is known both theoretically [1-3] and experimentally [1-4] to be a chief characteristic of relativistic/charge-displacement self-channeling [1-12]. Moreover, it is known that the influence of the ponderomotively generated charge-displacement is the major factor [2] governing the stability of the confined modes of propagation and it has been observed that this feature has a counterpart in the ponderomotive stabilization present in related areas of plasma physics and accelerator design [2]. It is also theoretically clear [2,3] that the eigenmodes play a key role in the dynamics of the stability, since they function as attractors and efficiently guide the energy into stable states of high power compression.

A regime of unstable propagation is also theoretically predicted [2] to exist, although a systematic experimental study of its properties is lacking. The unstable behavior can be roughly classified into two subcategories. They are (1) strongly unstable propagation that results in catastrophic filamentation, an outcome associated with an operating point located deep in the unstable region [2], and (2) weak instability associated with the stable/unstable boundary zone in which deviations from stable single channel propagation initially become apparent. The former regime is characterized by the development of a group of peripheral small-scale filaments each containing a power on the order of the critical power for self-channeling. Under these circumstances, an increase in the incident laser power leads primarily to a disorganized multiplication of filaments with the outcome that the trapped power in an individual filament does not increase. In the case of weak instability, however, when typically two channels are formed, the power of the strongest channel can be raised with an increase of the incident laser power. Overall, the principal characteristics of the weakly unstable behavior are (a) bifurcation of the propagating mode and (b) the development of lateral displacements of the confined power.

The present study discusses these irregularities in the propagation by examining both their experimental observation and the corresponding theoretical description. The main findings reported in this work are (i) the first experimental observations of bifurcation of the propagating channel and (ii) experimental confirmation of the previously proposed [1] use of a suitable longitudinal gradient in the plasma density for both the restoration of stable propagation and channel optimization.

II. DISCUSSION OF RESULTS

Experimental evidence for bifurcation is shown in Fig. 1(a), an image that displays a transverse view of the spectrally integrated Xe(M) radiation ($\sim 1\text{keV}$) produced by the propagating ultraviolet (248nm) radiation in a gaseous xenon cluster target [4,5] having a Xe density of $\sim 3 \times 10^{19} \text{ cm}^{-3}$. The

methods of measurement and the experimental conditions generally pertaining to the data in Fig. 1(a) have been previously described [4]. An interpretation of the observed Xe(M) spectrum has also been given [13].

The key feature shown in Fig. 1(a) is the dual structure visible at the longitudinal position $z \approx 1500 \mu\text{m}$. Since x-rays are generated, this indicates the existence of two separate parallel zones in which the power is highly compressed. In contrast, at the position corresponding to $z \approx 600 \mu\text{m}$, only a single feature is evident. In the process of channel formation, the incident propagating energy collapses from this initial region to a thin channel whose volume is sufficiently small that the x-ray emission from it is not visible in the exposure on account of the detection limit imposed by combined influence of (i) the relatively low spatial resolution ($\sim 30 \mu\text{m}$), (ii) the bound on the dynamic range of the detector, and (iii) the quenching of the Xe(M) emission in the high intensity zone of the channel that is caused by stripping of the entire 3d-shell by field ionization. This behavior causes the longitudinal gap ($800 \mu\text{m} \leq z \leq 1400 \mu\text{m}$) in the x-ray emission to occur. The subsequent bifurcation of the thin ($\sim 2-3 \mu\text{m}$ radius) channel [1-3] causes the dual feature at $z \approx 1500 \mu\text{m}$ to appear. We note that other studies [14] have examined the spectral properties of the Xe(L) emission from the intense central region of the filament.

The observed morphology of the x-ray signal can be put in contact with computations of the dynamics for conditions corresponding to those of the experiment. The modeling of the relativistic/charge-displacement self-channeling is based on a relatively simple model [5,6] that involves two dimensionless parameters; one represents the normalized power η , while the other describes the normalized radius ρ_0 of the incident radiation. They are given respectively by

$$\eta = P_0 / P_{\text{cr}} \quad \text{and} \quad \rho_0 = r_0 \omega_{p,0} / c. \quad (1)$$

In Eq. (1) P_0 represents the incident peak power associated with the central zone of the pulse and P_{cr} denotes the critical power for relativistic/charge-displacement self-channeling given by [5-7]

$$P_{\text{cr}} = (m_{e,0}^2 c^5 / e^2) \int_0^{\infty} g_0^2(\rho) \rho d\rho (\omega / \omega_{p,0})^2 = 1.6198 \times 10^{10} (\omega / \omega_{p,0})^2 \text{ W}, \quad (2)$$

in which $m_{e,0}$, c , and e have their standard identifications, $g_0(\rho)$ is the Townes mode [15], and ω , $\omega_{p,0} = (4\pi e^2 N_{e,0} / m_{e,0})^{1/2}$, and r_0 , respectively denote the angular frequency corresponding to the propagating radiation, the angular frequency of the unperturbed plasma, and the radius of the incident transverse intensity profile. A chief feature of the self-channeling process is the stabilization of the transverse beam profile near one of the z -independent modes of propagation designated as the lowest

eigenmodes [5,6] $U_{s,0}(\rho)$ (with index s , $0 < s < 1$) of the governing nonlinear Schrödinger equation. These eigenmodes have the dimensionless radius

$$\rho_{e,0} \equiv [2 \int_0^\infty U_{s,0}^2(\rho) d\rho / U_{s,0}^2(0)]^{1/2}. \quad (3)$$

The self-channeling process can be described as the dynamic adjustment of the radius r_0 of the incident focused beam to the radius r_{ch} of the laser channel, the value of which can be derived from the dimensionless radius $\rho_{e,0}$ of the corresponding lowest eigenmode [3,6] as

$$r_{ch} = \frac{c \rho_{e,0}}{\omega_p}. \quad (4)$$

Previous analysis [6] has shown that in the case of relativistic and charge-displacement self-channeling, the dimensionless radius of the channel $\rho_{e,0}$ varies extremely slowly over a large range of normalized laser power η , $\rho_{e,0} \approx \text{const}$ for $\eta > 1.5$, a property evident in Fig. 2. Therefore, from the expression for the plasma frequency

$$\omega_p = (3\pi e^2 N_e / m_{e,0})^{1/2}, \quad (5)$$

we conclude that the radius of the laser channel formed in a plasma with a local electron density N_e scales in good approximation [3] simply as

$$r_{ch} \sim N_e^{-1/2}. \quad (6)$$

The situation involving $\eta = P_0 / P_{cr} \gg 1$ and $r_0 / r_{ch} \gg 1$ leads to a strong self-focusing response which can be either stable or unstable [1,2]. Unfortunately, even in the stable case, the propagation is generally characterized by a substantial loss of laser power and the efficiency of the process is grossly compromised [3]. However, the efficiency of the power compression can be optimized when $r_0 \sim r_{ch}$ (or, equivalently, $\rho_0 \sim \rho_{e,0}$), a condition that can be dynamically achieved by the adjustment of the local electron density N_e (see Eq. (6)). This can be readily achieved with the use of an appropriate longitudinal gradient in the electron density distribution [3].

Previous work [2] has shown that the conditions governing the stability of relativistic/ponderomotive self-channeling are well described by two-dimensional (η, ρ_0) stability maps of the form illustrated in Fig. (2) and that specific zones corresponding to stable and strongly unstable propagation can be identified. In particular, the stability and efficiency of the relativistic/charge-displacement self-channeling mechanism have been analyzed [1,2] for perturbed Gaussian beams having incident transverse amplitude distributions given by

$$U_0(r, \phi) = I_0^{1/2} \exp(-0.5(r/r_0)^2 \times (1 + (r/r_0)^4 \sum \epsilon_q \cos(q\phi))). \quad (7)$$

In the profile represented by Eq. (7), the weak azimuthal perturbations are characterized by

$$\epsilon_q = 0.03, \quad q = 1 - 4, \quad \delta = \max |I_0(r, \phi_1) - I_0(r, \phi_2)| / I_0 = 0.21. \quad (8)$$

The information presented in the stability (η, ρ_0) map illustrated in Fig. (2) can be used to establish a direct correspondence between the experimental data shown in Fig. 1(a) and the theoretical procedures applicable to the dynamics of pulses with amplitude distributions given generally by the form of Eq. (7). The gaseous xenon cluster target is experimentally [4,14] produced by a pulsed valve having a ~ 1.5 mm orifice that is equipped with a vertical barrier on the side facing the incident 248nm beam. This wall, which contains an aperture having a diameter of ~ 100 μm , blocks the lateral expansion of the gas except in the local zone near the ~ 100 μm opening. Accordingly, a focal position located sufficiently inside the wall corresponds well to a uniform target density. In contrast, location of the focus in the region near or slightly outside of the 100 μm aperture causes the focussed pulse to propagate through a zone in which a substantial longitudinal gradient in target density is present. Therefore, adjustment of the focal position along the direction of propagation in the region defined by the barrier enables the alteration of the density gradient experienced by the focussed radiation. Consequently, there exists a controllable experimental procedure that can provide either a uniform target density or one possessing an appreciable density gradient.

The ability to modify the longitudinal density profile enables the dynamic trajectory of the operating point [1,3] of the system to be grossly altered. The principal consequence of this control, for the data shown in Fig. 1(a), can be understood by reference to Fig. 1(b) and Fig. (2). The initial condition corresponding to the development of the experimentally observed bifurcated channel illustrated in Fig. 1(a) is designated by the datum A_{uniform} in Fig.(2), a point that lies near the zone in which strong filamentation occurs [2]. Although in the stable region, it is significant to note that A_{uniform} is clearly located at a considerable remove from the eigenmode curve of the system $\rho_{e, o}(\eta)$ in this situation.

The computed evolution of an incident pulse corresponding to A_{uniform} is illustrated in Fig.1(b). The salient feature of the theoretical distribution is a strong spatial bifurcation, a characteristic that is in good qualitative correspondence with the experimental observation shown in Fig.1(a). Indeed, bifurcation into two roughly equal channels is shown. Experimentally, the bifurcated propagation becomes visible when the divergence of the two channels is sufficiently great that they can be separately resolved by the x-ray camera [4]. A continuation of the computed evolution of the pulse to longitudinal distances $Z > 400$ μm reveals that the stronger component of the bifurcated distribution shown in Fig.1(b) forms a stable channel that is denoted by point B_{uniform} in Fig.(2). We note that this datum falls

very close to the eigenmode curve [$\rho_{e,0}(\eta)$], a basic property of fully evolved stable channels [1,3] and a sharp contrast to the initial condition given by the location of A_{uniform} .

Previous studies have demonstrated that stable channels aggressively seek the eigenmode distribution [6]. Hence, the existence of a channel with an operating point corresponding to a position far from the eigenmode curve necessitates a major reorganization of its structure. The present results indicate that, for circumstances requiring a sufficiently large adjustment, the process of bifurcation enables the operating point of the system to make a single large and abrupt step toward the eigenmode curve. This mechanism, however, leads to very high losses, as the relative positions of A_{uniform} and B_{uniform} in Fig. (2) illustrate.

The use of a plasma gradient greatly alters the dynamics of propagation [3]. Specifically, it was theoretically predicated [3] that the process of bifurcation could be eliminated by the use of a suitable plasma gradient. This predication has now been experimentally confirmed, as shown by the data presented in Fig. 3(a). The morphology of the channel seen in Fig. 1(a) is transformed into that shown in Fig. 3(a) by a relocation of the incident focal zone to a region possessing an appreciable density gradient. It is apparent that the bifurcated region ($z \approx 1500 \mu\text{m}$) of the former has been replaced by an intense single channel in the latter. This was achieved experimentally solely by a small longitudinal shift in the focal position of the incident pulse to the region near the $100 \mu\text{m}$ aperture where a significant gradient in the target density exists. This adjustment places the operating point of the incident radiation in the proximity of the eigenmode.

A corresponding calculation of the pulse evolution which includes a suitable density gradient, shown in Fig. 3(b), illustrates the smooth development of a single channel. In this case, the initial condition has been remapped to point A_{gradient} in Fig. (2) and the trajectory of the operating point leads to the stable configuration by B_{gradient} . Since the loss caused by the formation of the second subsidiary channel in the bifurcated case has been eliminated, the efficiency of the transport into the channel formed has been significantly increased. The existence of the plasma gradient enables the pulse to reorganize in a less abrupt manner, thereby eliminating the need for the bifurcation.

III. CONCLUSIONS

Experimental observations of channel instability show good correspondence to computations of the channel dynamics. The leading instability is seen to be bifurcation of the propagating mode. The use of an appropriate density gradient can control this instability and lead to the efficient development of stable channels.

ACKNOWLEDGEMENTS

Support for this research was provided under contracts with ARO (DAAH04-94-G-0089), ARO (DAAG55-97-1-0310), the Department of Energy at the Sandia National Laboratories (DEAC04-94AL85000), and the Japanese Ministry of Education, Science, Sport, and Culture.

FIGURE CAPTIONS

Figure 1:

- (a) Experimentally observed morphology of channelled propagation obtained by imaging the Xe(M) radiation ($\sim 1\text{keV}$) transverse to the channel with an x-ray pinhole camera having a spatial resolution of $\sim 30\text{ }\mu\text{m}$. The procedures of the measurement are described in Ref. [4]. The incident 248 nm pulse had an energy of $\sim 350\text{ mJ}$ and a pulse width of $\sim 270\text{fs}$. The initial focusing action begins at $z \approx 0.5\text{ mm}$ and a clearly bifurcated region is visible at $z \approx 1.5\text{ mm}$. See text for discussion.
- (b) Computed pulse evolution corresponding to the experimental circumstances yielding the observed pattern shown in Fig. 1 (a). A strong bifurcation of the propagating node is seen, an outcome matching the experimental result.

Figure 2:

Stability map with coordinates (η, ρ_0) . The eigenmode curve, $\rho_{e,0}(\eta)$ is shown. A full description appears in Ref. [1]. See text for discussion of designated loci.

Figure 3:

- (a) Morphology of channel seen with adjustment of the incident focal volume to a region having an appreciable longitudinal plasma density gradient. The procedures of measurement were identical to those used in Fig. 1(a). A single channel is seen. See text for discussion.
- (b) Computed channel evolution for a pulse corresponding to the experimental conditions yielding the result in Fig. 3(a). A single channel is observed in conformance with observation.

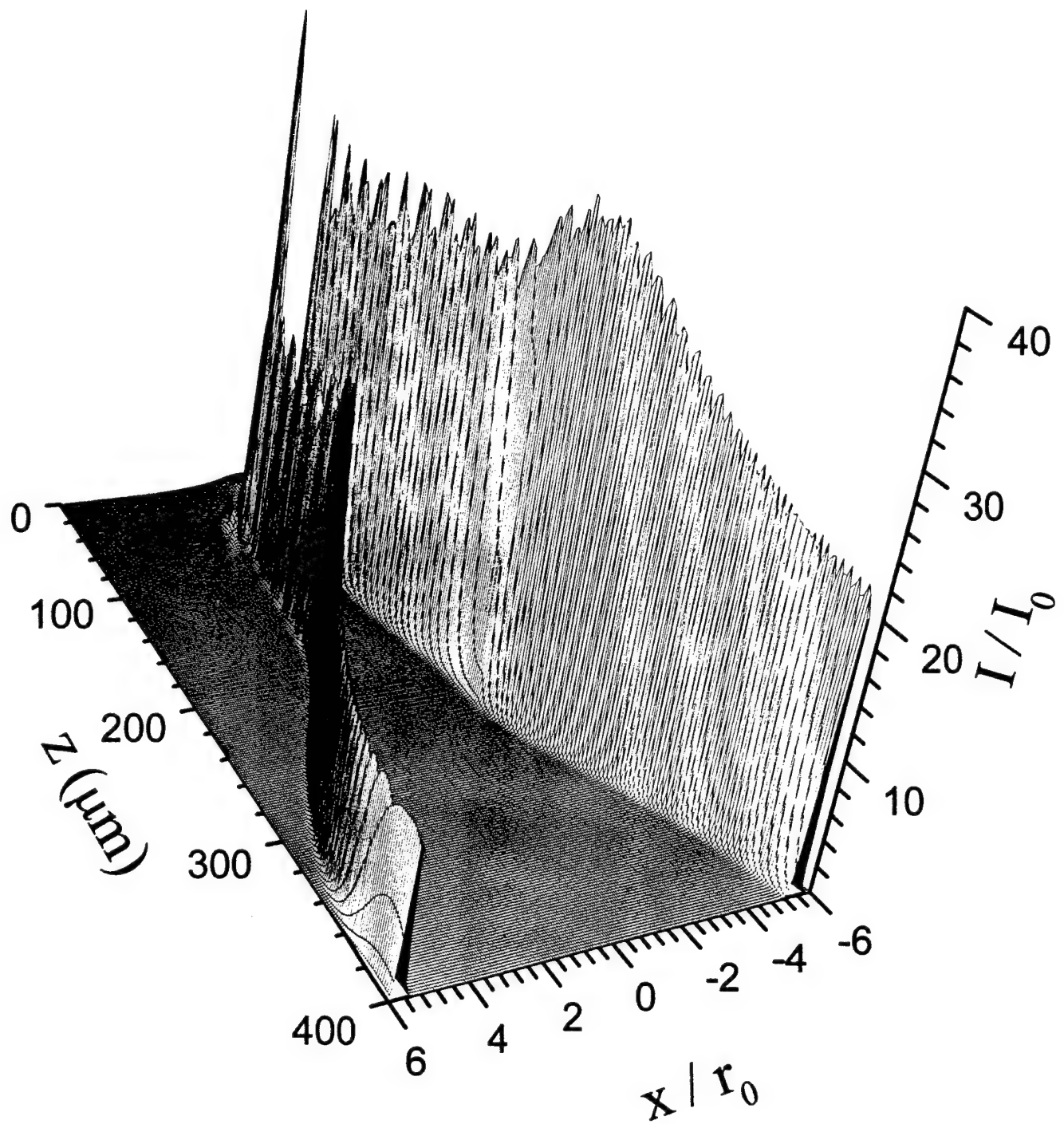


Fig. 1(b)

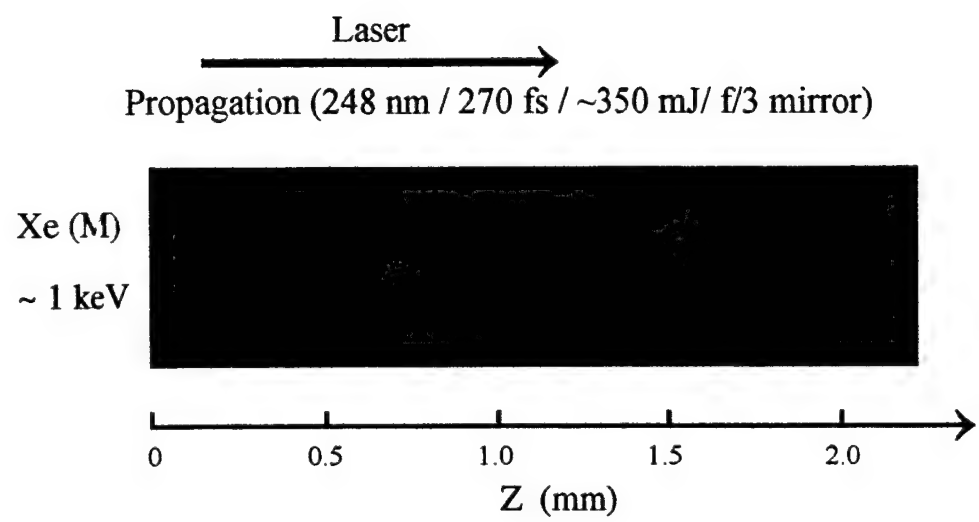


Fig. 1(a)

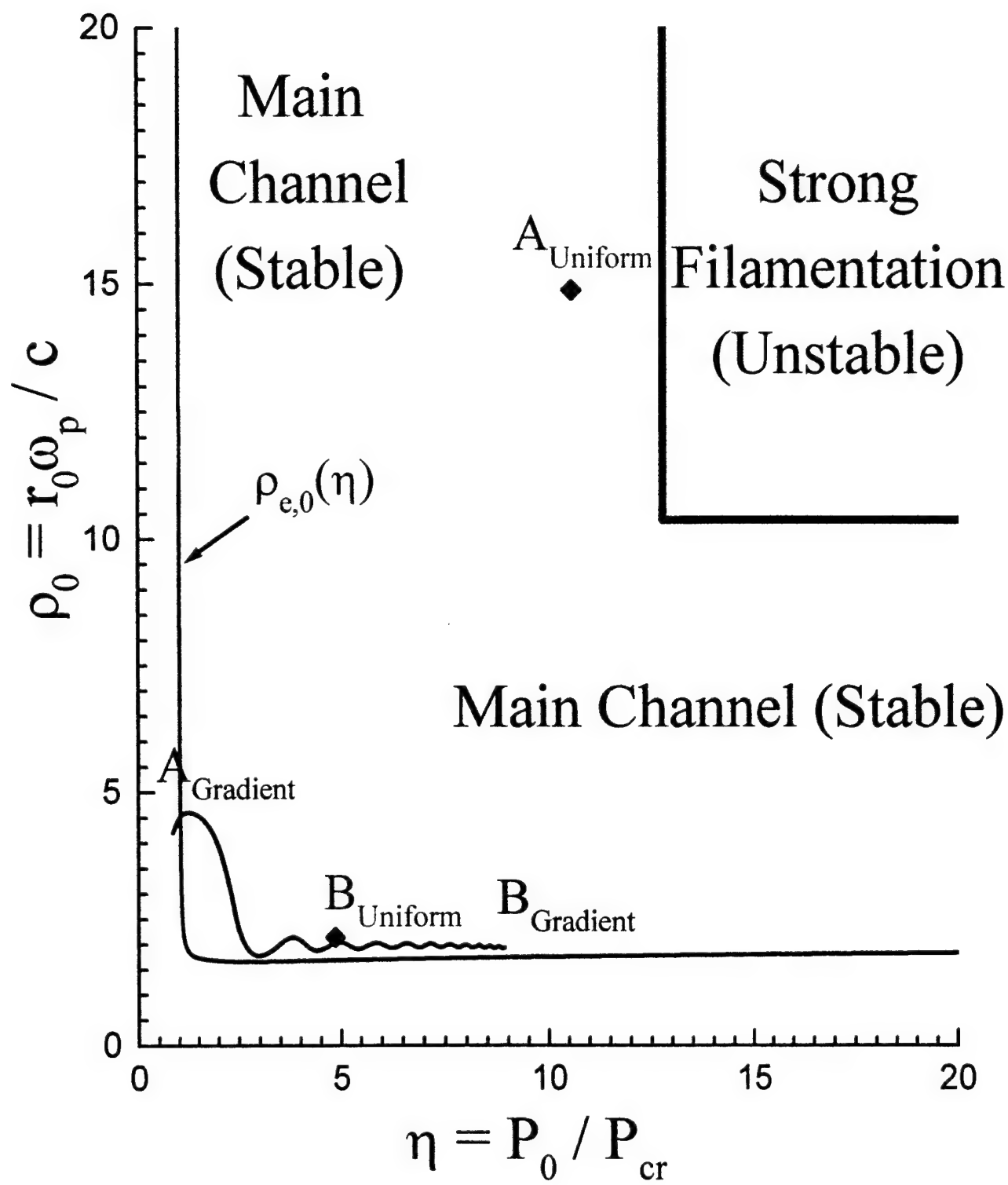


Fig. 2

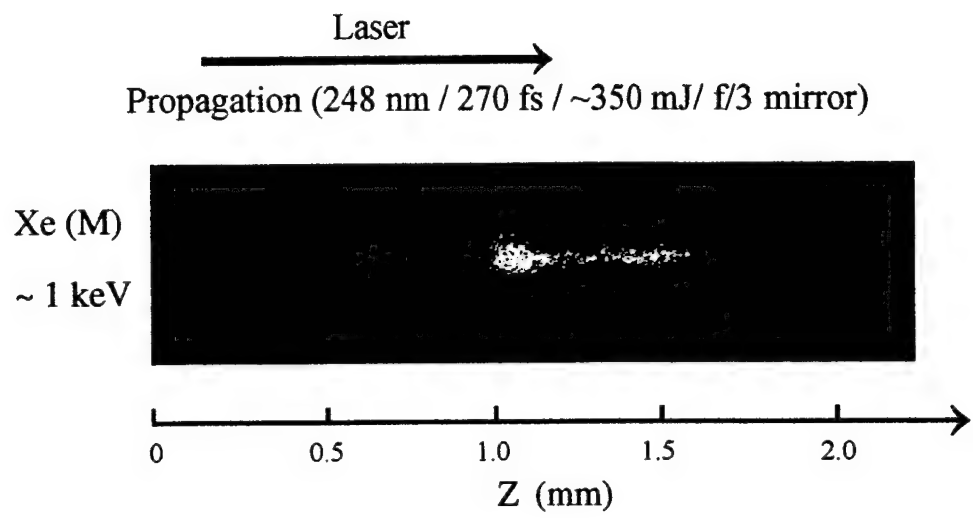


Fig. 3(a)

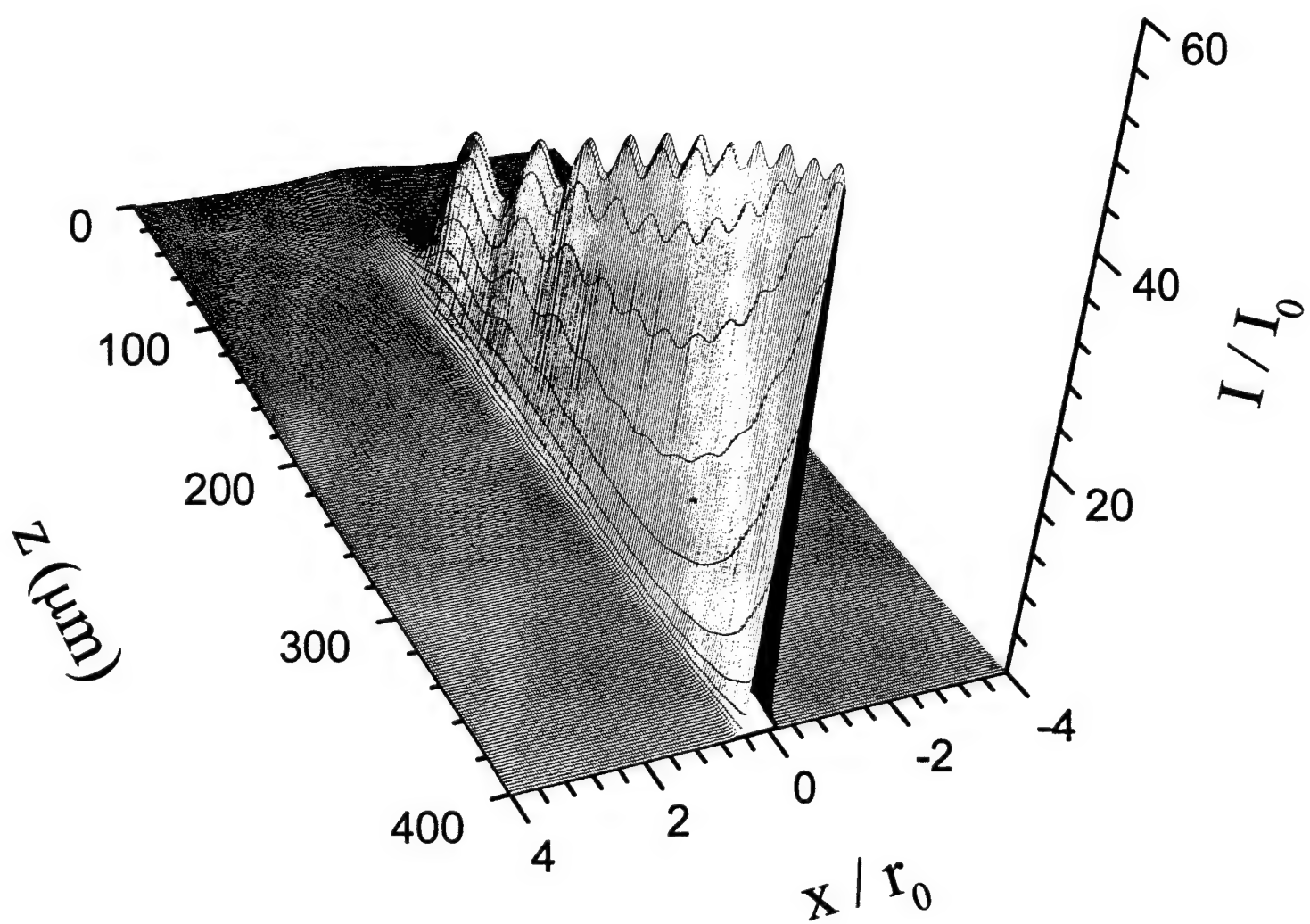


Fig. 3(b)

REFERENCES

1. Borisov, A. B., Longworth, J. W., Boyer, K., and Rhodes, C. K., "Stable Relativistic/Charge-Displacement Channels In Ultrahigh Power Density ($\sim 10^{21} \text{ W/cm}^3$) Plasmas," *Proc. Acad. Sci. USA* **95**, 7854, (1998).
2. Borisov, A. B., Shiryaev, O. B., McPherson, A., Boyer, K., and Rhodes, C. K., "Stability Analysis of Relativistic and Charge-Displacement Self-Channelling of Intense Laser Pulses In Underdense Plasmas," *Plasma Phys. Control. Fusion* **37**, 56 (1995).
3. Borisov, A. B., Cameron, S., Dai, Y., Davis, J., Nelson, T., Schroeder, W. A., Longworth, J. W., Boyer, K., and Rhodes, C. K., "Dynamics of Optimized Stable Channel Formation of Intense Laser Pulses with the Relativistic/Charge-Displacement Mechanism," *J. Phys. B* **32**, 3511 (1999).
4. Borisov, A. B., McPherson, A., Thompson, B. D., Boyer, K., and Rhodes, C. K., "Ultrahigh Power Compression for X-Ray Amplification: Multiphoton Cluster Excitation Combined with Non-Linear Channeled Propagation," *J. Phys. B* **28**, 2143 (1995).
5. Sun, G-Z., Ott, E., Lee, Y. C., and Guzdar, P., "Self-Focusing of Short Intense Pulses in Plasmas," *Phys. Fluids* **20**, 526 (1987).
6. Borisov, A. B., Borovskiy, A. V., Shiryaev, O. B., Korobkin, V. V., Prokhorov, A. M., Solem, J. C., Luk, T. S., Boyer, K., and Rhodes, C. K., "Relativistic and Charge-Displacement Self-Channeling of Intense Ultrashort Laser Pulses in Plasmas," *Phys. Rev. A* **45**, 5830 (1992).
7. Borisov, A. B., Borovskiy, A. V., Korobkin, V. V., Prokhorov, A. M., Shiryaev, O. B., Shi, X. M., Luk, T. S., McPherson, A., Solem, J. C., Boyer, K., and Rhodes, C. K., "Observation of Relativistic and Charge-Displacement Self-Channeling of Intense Subpicosecond Ultraviolet (248 nm) Radiation in Plasmas," *Phys. Rev. Lett.* **68**, 2309 (1992).
8. Borisov, A. B., Shi, X. M., Karpov, V. B., Korobkin, V. V., Shiryaev, O. B., Solem, J. C., McPherson, A., Boyer, K., and Rhodes, C. K., "Stable Self-Channeling of Intense Ultraviolet Pulses in Underdense Plasma, Producing Channels Exceeding 100 Rayleigh Lengths," *J. Opt. Soc. Am. B* **11**, 1941 (1994).
9. Monot, P., Auguste, T., Gibbon, P., Jakober, F., Mainfray, G., Dulieu, A., Louis-Jacquet, M., Malka, G., and Miquel, J. L., "Experimental Demonstration of Relativistic Self-Channeling of a Multiterawatt Laser Pulse in an Underdense Plasma," *Phys. Rev. Lett.* **74**, 2953 (1995).
10. Wagner, R., Chen, S-Y., Maksimchuk, A., and Umstadter, D., "Electron Acceleration by a Laser Wakefield in a Relativistically Self-Guided Channel," *Phys. Rev. Lett.* **78**, 3125, (1997).
11. Feit, M. D., Garrison, J. C., and Rubenchik, A. M., "Channeling of Intense Laser Beams in Underdense Plasmas," *Phys. Rev. E* **56**, 2394, 1997.
12. Chen, S-Y., Sarkisov, G. S., Maksimchuk, A., Wagner, R., and Umstadter, D., "Evolution of a Plasma Waveguide Created during Relativistic-Ponderomotive Self-Channeling of an Intense Laser Pulse," *Phys. Rev. Lett.* **80**, 2610 (1998).
13. Borisov, A. B., Longworth, J. W., McPherson, A., Boyer, K., and Rhodes, C. K., "Dynamical Orbital Collapse Drives Super X-ray Emission," *J. Phys. B* **29**, 247 (1996).

14. Borisov, A. B., McPherson, A., Boyer, K., and Rhodes, C. K., "Z-Imaging of Xe(M) and Xe(L) Emissions from Channelled Propagation of Intense Femtosecond 248 nm Pulses in a Xe Cluster Target," *J. Phys. B: At. Mol. Opt. Phys.* **29**, L113 (1996).
15. Chiao, R. Y., Garmire, E., and Townes, C. H., "Self-Trapping of Optical Beams," *Phys. Rev. Lett.* **13**, 479 (1964).
16. Bespalov, V. I. and Talanov, V. I., "Filamentary Structure of Light Beams in Nonlinear Liquids," *Pis'ma Zh. Eksp. Teor. Fiz.* **3**, 471 (1966), [*JETP Lett.* **3**, 307 (1966)].
17. Campillo, A. J., Shapiro, S. L., and Suydam B. R., "Periodic Breakup of Optical Beams Due to Self-Focusing," *Appl. Phys. Lett.* **23**, 628 (1973).

Appendix 2

Gamma-Ray Bursts and the Particle Mass Scale

*Yang Dai¹, Alexey B. Borisov², James W. Longworth³,
Keith Boyer², and Charles K. Rhodes²*

¹Department of Mathematical and Computing Sciences,
Tokyo Institute of Technology, JAPAN

²Department of Physics, University of Illinois at Chicago,
Chicago, IL 60607-7059, USA

³Department of Physics, Illinois Institute of Technology,
Chicago, IL 60616, USA

ABSTRACT

A mode of detonation for neutron stars is derived based on a physically defined power residue counting system used to construct a particle mass scale that reflects supersymmetric fermion/boson pairing. Neutron stars with specific mass values (M_a) can become unstable toward decay into an ensemble of highly energetic pairs of supersymmetric particles with an energy release whose upper bound can approach the rest mass energy of the original body. The subsequent scattering of these particles provides a way to account for (1) the high radiative yield ($\sim 10^{43}\text{-}10^{47}$ J) of gamma-ray bursts, (2) the large variability of their observed energy, and (3) the expected collateral production of ultrahigh energy cosmic rays. The joint action of (a) supersymmetric classification and (b) a new arithmetic selection rule designated as congruence conservation governs the condition of instability and the dynamic participation of the magnetic monopole obviates baryon number conservation. The decay patterns of certain elementary particles and putative supermassive forms of cosmological dark matter may be subject to similar conditions. Specifically, the analysis predicts the existence of a super-light boson neutrino ν_1 that plays a fundamental role in weak interactions and it is conjectured that the phenomenon of lepton number conservation is isomorphic to the supersymmetric conservation of congruence. The ν_1 boson also provides (i) a potential basis for the CP violation observed in K_L^0 decay and (ii) an alternative description of the attribute of strangeness. These interpretations support the conclusion that the observations of gamma-ray bursts signal the existence of a radically new organizing principle of physical interactions that defines a general condition of stability for massive particles and expresses the unstable case with the copious production of energetic emissions.

I. Introduction

The spectacular energy release ($\sim 10^{43}\text{-}10^{47}$ J), frequency of occurrence, high variability in output ($\sim 10^3\text{-}10^4$), and spectral characteristics ($\sim 10^{-1}\text{-}1$ MeV) of gamma-ray bursts currently lack a unified description [1-3]. Physical evidence is also extant which suggests the correlation of these observations with other energetic cosmic phenomena [4,5]. Various pictures of these enormously powerful radiative events plausibly involve neutron stars in processes that give rise to the production of super-relativistic charged particles whose collisional and magnetic Bremsstrahlung is the observed emission. The present study examines a specific mechanism which enables an individual neutron star (NS)

with mass M_a to undergo spontaneous detonation and produce an array of superenergetic particles with an aggregate yield comparable to the rest mass energy ($M_a c^2$) of the original body.

Basically, it is found that the system can become unstable if appropriate conditions governing its structure are satisfied. These conditions are defined by the existence of a new form of numerical (arithmetic) selection rule that reflects both the specific magnitude of the mass and its supersymmetric (fermi/bose) classification. An isolated elementary event of this nature considerably simplifies the circumstances of a gamma-ray burst in comparison to other

descriptions [1-4], since the participation of another exceptional astrophysical body (e.g. neutron star or black hole) is not necessary. Furthermore, with the customary mass limits [6,7] for neutron stars, it also produces an energy yield which conforms to the observed range. As indicated below, these considerations may also be relevant to the understanding of the phenomenon of lepton number conservation, CP violation in K_L^0 decay [8,9], the attribute of strangeness, and reactions involving putative supermassive forms of cosmological dark matter [10-12].

II. Discussion

A physically anchored scale invariant system of enumeration has been developed [11,12] which is capable of representing the particle mass spectrum in a way that explicitly respects supersymmetric fermion/boson pairing [12]. The manifest scale invariance of the counting procedure [11,12] confers on it the capacity to represent a particle with an arbitrarily large mass, thereby enabling a description of neutron stars or even more massive objects. A specific result of the analysis of the mass scale [12] was the prospective identification of a fundamental supersymmetric pair composed of a light ($m_e \sim 0.808$ meV) fermion, presumably representing the electron neutrino, and its supersymmetric partner, a heavy ($m_\chi \sim 1.22 \times 10^{28}$ eV) sneutrino which serves as a candidate for an immobile form of cosmological dark matter [10-12]. The predicted characteristics [11,12] of the sneutrino (m_χ) are such that it can account for the existence [12] of a cosmological constant with a value of $\Lambda \equiv 0.7$. Since the masses m_e and m_χ of these two particles physically define the mathematical bases of a dual counting operation, they were nominated as the basis of a fundamental organizing principle through their roles as the twin generators of the mass scale. The supersymmetric fermion/boson classification that emerged [12] was also found to be consistent with the values of the masses computed in prior work [11] for both the electron and the proton.

The physically established counting system [12], which represents particle masses with a normalized integer amplitude B , is expressed with power residues and congruences [13] of the form

$$g_\alpha^{t_\alpha} \equiv B \pmod{P_\alpha}, \quad (1)$$

in which P_α is a prime modulus, g_α is a primitive root [14-17] of P_α , and t_α is the integral index parameter (power) whose range is determined by the Euler function $\phi(P_\alpha)$ as $0 < t_\alpha < P_\alpha - 1$. Furthermore, since the specific magnitudes of P_α and g_α are independently and directly founded [12] on an interlocking set of observational data involving the Hubble dimension, the mass of the universe, chief characteristics of the cosmic microwave background, the magnitude of the gravitational constant G , and the value of the fine-structure constant α , the power residue formulation combines a

physically unique definition, based on both cosmic phenomena and microscale couplings, with a strict mathematical imperative, the primitive root relation between P_α and g_α . The integer P_α also physically represents the mass of the magnetic monopole [11], a crucial condition in relation to the stability of a neutron star, since the dynamic presence of that particle [18] enables the occurrence of processes which violate baryon number conservation [19].

Consider an isolated uncharged rotationally static mass M_0 and proportionally corresponding [11,12] normalized mass parameter B_0 . From Eq. (1), we can write the explicit relation

$$B_0 = g_\alpha^{t_\alpha 0} + k_{\alpha 0} P_\alpha \quad (2)$$

for appropriate integer indices ($t_{\alpha 0}$, $k_{\alpha 0}$). Since previous studies [11,12] have identified g_α as an even number and P_α as an odd prime, the correspondence B_0 (odd, even) and $k_{\alpha 0}$ (odd, even) for the modulus index holds. Furthermore, since the supersymmetric classification [12] generally partitions fermions and bosons with the parity of k_α , any mass, including a neutron star, can have either fermi or bose character depending upon the corresponding parity of the mass parameter B_0 . The previous study of the mass scale [12] led to the conclusion that k_α (even/odd) corresponds to (fermi/bose), respectively.

We now derive the conditions necessary for the elementary process of decay of a system with mass M_0 into two energetic particles with masses m_x and m_y and corresponding integer mass parameters B_x and B_y in the reaction

$$M_0 \rightarrow m_x + m_y. \quad (3)$$

Using the normalized momenta (A_x , A_y , A_0), masses (B_x , B_y), and total energies (C_x , C_y , C_0) defined generally in earlier work [11], the corresponding relativistic energy/momentum relations

$$B_0 = C_0, \quad (4)$$

$$A_x^2 + B_x^2 = C_x^2, \quad (5)$$

and

$$A_y^2 + B_y^2 = C_y^2 \quad (6)$$

hold in the rest frame ($A_0=0$) of the particle M_0 . With the conditions for conservation of linear momentum and energy given by

$$A_x + A_y = 0 \quad (7)$$

and

$$C_x + C_y = C_0 = B_0, \quad (8)$$

the solution of Eqs. (5) and (6) yields the individual particle energies

$$C_x = \frac{1}{2} \left[B_0 + \frac{B_x^2 - B_y^2}{B_0} \right] \quad (9)$$

and

$$C_y = \frac{1}{2} \left[B_0 - \frac{B_x^2 - B_y^2}{B_0} \right]. \quad (10)$$

Since C_x and C_y are constrained to have integral values [11], we require that

$$B_0 \pm \frac{(B_x^2 - B_y^2)}{B_0} = 2k_{\pm} \quad (11)$$

for some integers k_+ and k_- , a condition that yields

$$\pm (B_x^2 - B_y^2) = (2k_{\pm} - B_0)B_0. \quad (12)$$

With the further definition of the effective modulus parameters

$$k_{0\pm} = 2k_{\pm} - B_0, \quad (13)$$

Eq. (12) can be expressed as the quadratic congruence

$$B_x^2 \equiv B_y^2 \pmod{B_0}. \quad (14)$$

Equation (14) represents an arithmetic selection rule relating the three mass parameters B_x , B_y , and B_0 for the two-body decay given by Eq.(3). Consequently, the permissible solutions of Eqs.(9) and (10) are subject to constraints that are dependent upon the detailed arithmetic structures of B_x , B_y , and B_0 . From Eq. (13) it is immediately seen that the supersymmetric classification of mass parameters causes two classes of solutions corresponding to bose and fermi species to exist. Specifically, we have the effective modulus parameters k_{\pm} (even/odd) for B_0 (fermi/bose), respectively. Many characteristics of the solutions of Eq.(14) are known [13,14,20,21]. For example, any integer [14,20] represented by the form $B_x^2 - B_y^2$ is either odd or a multiple of 4, and general classes of solutions of the congruence are available in both cases [21].

The restriction of Eq.(14) to decay pathways involving supersymmetric pairs defines an important subclass of solutions. The properties of these solutions can be examined by utilizing the conjecture that the sum Σ , of the masses of all supersymmetric pairs is governed by the statement

$$\Sigma_S \equiv 0 \pmod{P_{\alpha}}, \quad (15)$$

the outcome suggested by the study [12] of the systematics of the power residue mass scale. Therefore, if we assume that B_x and B_y represent a supersymmetric pair, we have

$$B_x + B_y \equiv 0 \pmod{P_{\alpha}}, \quad (16)$$

or equivalently,

$$B_y = k_{xy}P_{\alpha} - B_x \quad (17)$$

for some odd integer k_{xy} , since $B_x + B_y$ must be odd. Explicitly forming the quadratic difference

$$B_x^2 - B_y^2 = 2k_{xy}B_xP_{\alpha} - k_{xy}^2P_{\alpha}, \quad (18)$$

it follows that

$$B_x^2 \equiv B_y^2 \pmod{P_{\alpha}}. \quad (19)$$

Hence, the combination of Eqs. (14) and (19) yields the additional relation [17]

$$B_x^2 \equiv B_y^2 \pmod{N_{\alpha 0}} \quad (20)$$

in which the modulus $N_{\alpha 0}$ is the least common multiple of B_0 and P_{α} . Since P_{α} is a prime, the minimum value of $N_{\alpha 0}$ attainable is P_{α} . Physically, of course, this decay can only occur if $B_0 \geq P_{\alpha}$.

We now summarize the development given above. The conditions stated in Eqs. (13) and (14) define a general arithmetic selection rule corresponding to amplitudes for two-body decay of fermi and bose particles that is consistent with supersymmetric classification. The restriction of this selection rule to pathways involving the production of supersymmetric fermion/boson pairs is represented by Eqs. (14), (19), and (20). We note that fulfillment of these conditions is explicitly consistent with integral solutions for A_x and A_y , and the condition $A_x + A_y = 0$, a statement whose proof is readily demonstrated by direct substitution of Eqs. (9) and (10) into the corresponding Eqs. (5) and (6). Hence, the identical selection rules govern both energy and momentum. We designate this selection rule generally as the conservation of congruence.

A. Conservation of Congruence and Angular Momentum

The consequences of the joint conservation of congruence and angular momentum on the decay pathways of an isolated massive particle are now evaluated. At a further point, the role of baryon number conservation and related implications concerning lepton number conservation [19] will be explored.

1. Fermi Mass Parameter

In this case, since B_o and the corresponding modulus parameters $k_{\alpha\beta}$ are even, $B_x^2 - B_y^2$ is perforce even on the basis of the supersymmetric classification [12]. Indeed, as noted above [14], $B_x^2 - B_y^2$ is generally a multiple of 4. Hence, B_x and B_y are either (a) both even (fermi) or (b) both odd (bose). Since two fermions or two bosons cannot represent the angular momentum state of a single fermion, the two-body decay paths into either fermions or bosons is strictly forbidden by the conservation of angular momentum. The remaining possibility for two-body decay, which leads to a final state composed of a fermion/boson pair, is barred by supersymmetry from Eqs. (13) and (14). Hence, all two-body pathways for the decay of fermi species (B_o) are forbidden.

It is important to recognize that this result is entirely dependent upon the classification of fermions with even mass parameters in the construction of the mass scale [12], an outcome that arose perforce from consideration of supersymmetric fermion/boson pairing with respect to the identification of the mass of the electron neutrino (ν_e). Had that assignment been the reverse, with the specification of odd mass parameters for fermions, the reaction shown by Eq. (3) would be allowed for a fermion/boson pair, since the integer parity condition demanded by Eqs. (11) through (14) and the angular momentum requirement could be simultaneously satisfied. This alternative assignment would have lifted the bar imposed by supersymmetry. Therefore, the conclusion is reached that all two-body amplitudes are forbidden for fermi character B_o by the combined demands of conservation of supersymmetric congruence and angular momentum. Specifically, we arrive at the important outcome that the single fermion/boson pair channel is blocked by supersymmetry.

2. Bose Mass Parameter

Boson decay gives B_o odd and $B_x^2 - B_y^2$ odd with the direct consequence that B_x^2 and B_y^2 are necessarily of opposite parities. It follows that the only supersymmetry allowed two-body final state is a fermion/boson pair. However, since this configuration cannot satisfy the angular momentum requirements for a bose system, the amplitude is forbidden. Again, the joint action of the conservation of supersymmetric congruence and angular momentum rules out an amplitude for two-body decay. It is important to note from Eqs. (14) and (20), however, that for a system of bose

character, the single fermion/boson channel is allowed by supersymmetry in contrast to the fermi case with B_o even.

Table I summarizes the conclusions governing two-body amplitudes for both fermi and bose particles. The astonishing result is that all two-body channels are forbidden by the joint fulfillment of congruence and angular momentum conservation. Obviously, a bold contradiction to the clear experimental observation [22] of two-body decay channels for a wide range of elementary systems (e.g. $\pi^+ \rightarrow \mu^+ + \nu_\mu$) is presented by this highly unexpected outcome. This important conflict is fully-resolved below in Section II.A.3.b through the development of a specific physically motivated modification of Eq.(14).

B_o	Two-Body Amplitude	Selection Rules	
		Angular Momentum	Supersymmetry/ Congruence
Fermi	$f_x + f_y$	Forbidden	Allowed
Fermi	$f_x + b_y$	Allowed	Forbidden
Fermi	$b_x + b_y$	Forbidden	Allowed
Bose	$f_x + f_y$	Allowed	Forbidden
Bose	$f_x + b_y$	Forbidden	Allowed
Bose	$b_x + b_y$	Allowed	Forbidden

Table I: Summary of two-body amplitudes for the decay of a fermi/bose particle with mass parameter B_o . The notation f/b designates fermi or bose particles for the final state $m_x + m_y$, given by Eq. (3). The joint requirements of congruence and angular momentum conservation block all two-body channels.

3. Supersymmetric Pair Pathways and Lepton/Baryon Conservation

a. Three-Body Amplitudes

The addition of a third body (m_z) consistent with the requirements of angular momentum conservation, which converts Eq.(3) to the three-body process

$$M_0 \rightarrow m_x + m_y + m_z, \quad (21)$$

enables all six channels in Table I to become allowed. In interesting contrast to the fundamentally unsolvable nature of the standard 3-body problem [23] and the complexities of radiative corrections to normal channels of β -decay [24], it is easily seen that the energies and momenta characterizing the three-body final state can be exactly determined on the

integral energy/momentum lattice. This fact can be demonstrated from known properties of the solution [11] of the elementary case which involves values of B_x , B_y , and B_z given by odd primes. Subject to the physically necessary condition $B_x + B_y + B_z < B_o$, this case admits the possibility of only a single solution for the three-body final state. It is readily shown that the specific solution for B_x , B_y , and B_z prime corresponds to

$$A_x = \frac{B_x^2 - 1}{2}, \quad C_x = \frac{B_x^2 + 1}{2} \quad (22)$$

$$A_y = \frac{B_y^2 - 1}{2}, \quad C_y = \frac{B_y^2 + 1}{2}; \quad (23)$$

and

$$A_z = \frac{B_z^2 - 1}{2}, \quad C_z = \frac{B_z^2 + 1}{2}, \quad (24)$$

under the condition that the subsidiary statements

$$2B_o = B_x^2 + B_y^2 + B_z^2 + 3 \quad (25)$$

and

$$B_x^2 + B_y^2 \geq B_z^2 + 1 \geq B_x^2 - B_y^2 + 2 \quad (26)$$

are fulfilled. Equation (25) represents energy conservation while the inequalities [25] expressed in Eq.(26) enable satisfaction of the conservation of linear momentum. For explicit confirmation of solvability, the values $(B_x, B_y, B_z) = (29, 23, 31)$ uniquely satisfy the conditions of Eqs. (25) and (26) for $B_o = 1167$. Since all four mass parameters are odd, this numerical example would represent the decay of a boson into three bosons, an outcome that also satisfies the demand for angular momentum conservation. This simple case demonstrates the existence of arithmetic constraints on the set of mass parameters $\{B_x, B_y, B_z, B_o\}$ which determine the condition for solvability.

The generalization to composite mass parameters, which gives the possibility of a multiplicity of solutions, is readily formulated. In order to obtain a high density of solutions per unit normalized energy [11] of the individual particles m_x , m_y , and m_z , the corresponding mass parameters B_x , B_y , and B_z must be composite high k-factorable low z-smooth integers [26] whose arithmetic factor structures are mutually subject to numerical constraints. Basically, these constraints must be such that the number of representations $N(B_o)$ of the integer B_o , which denotes the total energy of the system, through the expression

$$C_x + C_y + C_z = B_o, \quad (27)$$

is high. Formally, we can express Eq.(27) as

$$2B_o = d_x + d_y + d_z + \frac{B_x^2}{d_x} + \frac{B_y^2}{d_y} + \frac{B_z^2}{d_z}, \quad (28)$$

in which d_x , d_y , and d_z respectively represent the appropriate divisors of B_x^2 , B_y^2 , and B_z^2 . Satisfaction of linear momentum conservation requires that the subsidiary conditions

$$\frac{B_x^2}{d_x} + \frac{B_y^2}{d_y} \geq \frac{B_z^2}{d_z} + d_x + d_y - d_z \geq \frac{B_x^2}{d_x} - \frac{B_y^2}{d_y} + d_x + d_y \quad (29)$$

also be fulfilled. We observe that Eqs.(28) and (29) coincide with the corresponding statements in Eqs.(25) and (26) for the case

$$d_x = d_y = d_z = 1. \quad (30)$$

The existence of these arithmetic conditions obviously carries important implications for the systematics of the particle mass scale [12] and the observed channels of decay. For example, if the sets of mass parameters $\{B_o, B_x, B_y, B_z\}$ are such that Eqs. (28) and (29) do not possess a solution for all physically possible choices of B_x , B_y , and B_z , the particle M_o in Eq. (21) would behave as a stable system like the proton. In this way, Eqs. (28) and (29) define the conditions governing particle stability.

Since the squares of suitably smooth integer mass parameters for typical particles like the electron and proton can have more than 10^{12} divisors [11], the requirement for a high representation number $N(B_o)$ involves a complex set of relations concerning the arithmetic structures of the mass parameters whose precise nature remains to be formulated [21]. It may be possible to consider Eq. (28) as a restricted class of partitions [27] of the even integer $2B_o$.

A physical example of the three-body final state for the decay of a fermion is the commonly observed conversion of a free neutron to a proton, an electron, and an electron anti-neutrino by the 3-body amplitude

$$n \rightarrow p + e^- + \bar{\nu}_e. \quad (31)$$

This process explicitly exhibits the conservation of lepton number, an empirically established quantity which is believed to be separately conserved for electron, muon, and tau species. In principle, of course, the third body (m_o) in Eq.(21) could also be a photon, as it is in the Dalitz decay [22] of the neutral pion (π^0). In light of the discussion given above, the comparison between the character of the theoretical results illustrated in Table I and the experimentally observed behavior of particle decay channels (e.g. the neutron) suggests that supersymmetric congruence

conservation may potentially provide a mathematical basis for the phenomenon of lepton number conservation. Separate conservation of lepton number for electron, muon, and tau amplitudes would then be direct consequences of the detailed arithmetic structures of the mass parameters of those particles (e.g. e^- , μ^- , τ^- , \bar{v}_e , \bar{v}_μ , \bar{v}_τ) and the ability of the specific factors of these parameters to satisfy the arithmetic demands expressed by Eqs.(28) and (29) with integers of the correct parity, in addition to the requirement for the conservation of angular momentum. This hypothesis is currently under computational evaluation with respect to the β -decay of the neutron [Eq. (31)], since the neutron/proton mass ratio is experimentally known to high precision [22] and candidate values for the mass parameters of the p, e^- , and \bar{v}_e are available [11,12].

b. Analysis of Two-Body Channels

Two-body decay channels for both fermi and bose systems are well established experimentally for many particles (e.g. $K^+ \rightarrow \mu^+ + v_\mu$, $\pi^+ \rightarrow \mu^+ + v_\mu$, and $\Lambda^0 \rightarrow p + \pi^-$). It is obvious that these observational facts stand in direct contradiction to the conclusions stated in Table I. The manner in which this conflict can be resolved is now described.

The resolution of this issue requires the participation of an additional interacting particle. The influence of a third body in the final state of the system with a mass parameter of unity ($B_z = 1$), as expressed through Eqs.(28) and (29), has a magnitude sufficient to nullify fully the arithmetic restrictions given by Eq.(14). Since this conclusion is valid for B_x , B_y , and B_0 of any numerical size, the minimal value $B_z = 1$ has scale invariant consequences. Hereafter, a bose particle with the mass parameter of unity will be designated with the symbol v_1 .

The physical consequences of this super-light boson can be readily evaluated. Specifically, with $B_z = 1$, Eqs.(28) and (29) are respectively modified to read

$$d_x + d_y + \frac{B_x^2}{d_x} + \frac{B_y^2}{d_y} = 2(B_0 - 1) \quad (32)$$

and

$$d_x - d_y - \frac{B_x^2}{d_x} + \frac{B_y^2}{d_y} = 0, \quad (33)$$

results which lead immediately to the statement

$$B_x^2 - B_y^2 = (d_x - d_y)(B_0 - 1) \quad (34)$$

With the identification of the factor $(d_x - d_y)$ with the modulus index

$$k = d_x - d_y, \quad (35)$$

Eq. (34) can be written as the congruence

$$B_x^2 \equiv B_y^2 \pmod{B_0 - 1}, \quad (36)$$

a form which is identical to Eq.(14) under the transformation of the modulus $B_0 \rightarrow B_0 - 1$. It also follows from Eqs. (32) and (33) that

$$B_0 = d_{x0} + d_{y0} + 1, \quad (37)$$

in which d_{x0} and d_{y0} respectively represent specific members of the sets of divisors of the integers B_x^2 and B_y^2 .

The shift of unity in the value of the modulus completely eliminates the restrictions listed in Table I arising from violation of the supersymmetry/congruence selection rule. Consider the known [22] weak decay process

$$\pi^+ \rightarrow \mu^+ + v_\mu, \quad (38)$$

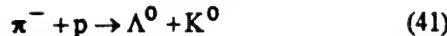
a reaction that is forbidden by supersymmetry in Table I. However, if the reaction given by Eq.(38) is physically reinterpreted to be

$$\pi^+ \rightarrow \mu^+ + v_\mu + v_1, \quad (39)$$

the amplitude becomes fully allowed as a three-body process in accord with Eq.(36). Furthermore, since Eq.(24) states that a particle with a mass parameter of unity ($B_z = 1$) can only have a vanishing momentum ($A_z = 0$), the v_1 particle plays no role in the distribution of momentum. Therefore, the kinematic conservation of momentum is observationally identical in both Eqs.(38) and (39). The particle v_1 acts as an experimentally invisible boson neutrino whose rest mass energy is given by the quantity (E_0), the quantity which defines the minimum energy uncertainty of the system [11,12]. Hence, energy conservation is also observationally unaffected by the coupling to the v_1 particle. Consequently, the three-body reaction for π^+ decay shown in Eq.(39) behaves kinematically as a two-body amplitude that would not be distinguished from Eq. (38) by standard procedures of measurement. In contrast, the decay of the neutron given in Eq.(31) behaves kinetically as a conventional three-body process and yields a continuous spectrum of particle energies. The amplitudes governing the decay patterns of all other known particles [22] appear consistent with this formulation. For example, the principal decay mode of the Λ^0 hyperon ($\Lambda^0 \rightarrow p + \pi^- + v_1$), a fermion, can be likewise considered as the reaction

$$\Lambda^0 \rightarrow p + \pi^- + v_1. \quad (40)$$

This reassignment of the amplitude for Λ^0 decay in Eq. (40) also suggests an alternative interpretation of the attribute of strangeness. Specifically, the low rates generally exhibited by nonleptonic hyperon (e.g. Λ^0 , Σ^* , Ω^-) decay can be regarded to be the result of a suitably weak coupling to the v_1 boson in processes of the form shown in Eq. (40) for the Λ^0 particle. At the same time, it is important to note that the corresponding production of the Λ^0 system by the reaction



can occur unsuppressed directly through the strong interaction. This follows, since the participation of four strongly interacting particles (π^- , p , Λ^0 , K^0) allows the arithmetic conditions specified by Eqs. (28) and (29) to be satisfied. The conundrum of strong production joined with weak decay in the $\pi^- + p$ channel is thereby resolved. Further, the nonoccurrence of the amplitude



can also be understood as a case for which the divisors of the corresponding mass numbers of the particles do not admit a solution of Eqs. (28) and (29). Therefore, the behavior associated with the assignment of strangeness can be alternatively considered to be the natural consequence of (a) weak coupling to the v_1 boson and (b) the arithmetic requirements of Eqs. (28) and (29).

The v_1 particle can be given a supersymmetric classification [12] in relation to the mass scale expressed by Eqs. (1) and (2). Specifically, in accord with the previous development [12] of Eq.(15), the corresponding supersymmetric partner ϕ_1 of the v_1 particle has a mass parameter with the value $P_\alpha - 1$. Therefore, this assignment predicts the existence of a supermassive fermion ϕ_1 with a mass infinitesimally shifted from that of the monopole [11,12]. Overall, the characteristics of the ϕ_1 particle mark it as an attractive candidate for a supermassive component of cosmological dark matter [10-12].

Since the construction of the supersymmetric mass scale led to the definition of a four dimensional index space [12], the corresponding indices of the v_1 particle associated with the power residue formulation (cf. Eqs. (1) and (2)) can be given. They are $t_\alpha = t_\beta = 0$ for the power indices and $k_\alpha = k_\beta = 0$ for the modulus indices. Hence, the v_1 boson physically defines the origin of the index space governing the classification of particle masses. It is also simply shown [12] that the two power indices corresponding to the supersymmetric partner ϕ_1 are degenerate with values of $t_\alpha = t_\beta = (P_\alpha - 1)/2$.

The presence of the v_1 boson enables a three-body amplitude to behave observationally as a two-body process. For example, if a neutral particle were to have two bosonic modes of decay, one involving three bosons (e.g. π^+, π^-, π^0), and another yielding two bosons and an unobserved

v_1 particle (e.g. π^+, π^-, v_1), experimentally distinct 3π and 2π channels with different lifetimes would be identified. In this case, the two decay modes are simply related by a π/v_1 exchange. Interestingly, for K mesons, this experimental characteristic is precisely the signature of direct CP violation in K_L^0 decay [8,9]. Therefore, the existence of a v_1 boson could provide a mathematical basis for CP violation which is founded on the power residue formulation of the particle mass scale [12].

c. Baryon Conservation

Baryon conservation naturally forbids the detonation of a neutron star in a process which calls for a massive decrease in baryon number to occur. However, this customary restriction can be obviated by the dynamic participation of the magnetic monopole [18,19], the key particle promoting baryon nonconservation. Since the theoretical picture underlying the construction of the mass scale [12] suggests that the mass numbers associated with supersymmetric fermion/boson pairs generally satisfy the congruence given by Eq. (16), we can generally write

$$B_f + B_b \equiv 0 \pmod{P_\alpha}, \quad (43)$$

in which the subscripts f and b denote fermi and bose particles, respectively. We recall, since $B_f + B_b$ must be odd, this statement specifies that the masses physically sum to an odd multiple (nP_α , $n=1, 3, 5, \dots$) of the monopole mass [12]. Hence, for the case $n=1$, the sum of the masses of an arbitrary supersymmetric pair would correspond exactly to the monopole mass shell (P_α). In turn, this suggests that the baryon nonconserving decay of a massive object can occur through the production of an ensemble of supersymmetric pairs, or equivalently, by a process that goes directly through the monopole state for every particle/pair. The monopole would then play the role of the fundamental modulus connecting the individual decay channels through a baryon nonconserving amplitude. Therefore, with this interpretation, the ability to involve dynamically the monopole state through the satisfaction of Eq. (43) obviates the restriction of baryon conservation.

We conclude that two conditions must be fulfilled to permit the existence of a baryon nonconserving channel for the decay of an isolated body with mass M . They are (1) the presence of three or more particles in the final state and (2) the availability of an amplitude involving the production of supersymmetric pairs which couple directly through the monopole mass shell P_α .

Allowed decay channels for both bose and fermi character systems can now be classified. Under the combined requirements of Eqs. (13), (14), (19), (20), (28), and (29) it is immediately seen that bose species can undergo baryon nonconserving decay into channels involving supersymmetric pairs ($f_x + b_y$) in reactions of the general form

$$B_0(\text{bose}) \rightarrow (f_x + b_y)_{2m-1} + (f_z)_{2n-1} \quad (44)$$

and

$$B_0(\text{bose}) \rightarrow (f_x + b_y)_{2m} + (b_z)_{n-1}, \quad (45)$$

in which m and n are nonzero integers ($m, n = 1, 2, 3, \dots$), f_x and b_y denote respectively a supersymmetric particle pair with corresponding mass parameters $B_x = B_f$ and $B_y = B_b$, and f_z, b_z designates an appropriate fermion/boson companion with mass parameter B_z . The two decay pathways given by Eqs. (44) and (45) can satisfy (a) the specific requirements for conservation of angular momentum, linear momentum, and energy, (b) the general consequences of the arithmetic constraints, and (c) the need to proceed on the monopole mass shell for the $(f_x + b_y)$ supersymmetric pairs.

The corresponding conditions are now determined for the decay of a system with fermi character. A final state, containing a single pair is forbidden by supersymmetry, as shown in Table I, and the two-pair channel is blocked by the conservation of angular momentum. However, the presence of an additional boson or fermi particle (b_z or f_z , respectively) in the final state, as discussed above in Sections II.A.3.a and II.A.3.b, obviates these restrictions and reactions involving the production of supersymmetric pairs $(f_x + b_y)$ conforming to Eq. (43) of the general form

$$B_0(\text{fermi}) \rightarrow (f_x + b_y)_{2m-1} + (b_z)_n \quad (46)$$

and

$$B_0(\text{fermi}) \rightarrow (f_x + b_y)_{2m} + (f_z)_{2n-1} \quad (47)$$

with m and n integral ($m, n = 1, 2, 3, \dots$) become allowed. In parallel with the boson case described above, these two channels allow the full satisfaction of all the corresponding constraints for fermi species B_0 .

The decay channels given by Eqs. (44), (45), (46), and (47) represent amplitudes for baryon nonconserving reactions which yield supersymmetric $(f_x + b_y)$ pairs for both fermi and boson character systems. Specifically, for the case $m=n=1$, Eqs. (44) and (46) can be put in direct correspondence with the statements expressed in Eqs. (28), (29), and (43). Consequently, in the discussion below, we will assume that the pathways for the decay of a neutron star involve the disintegration into an ensemble of energetic supersymmetric pairs and associated particle companions whose subsequent electromagnetic scattering gives rise to the phenomenon of gamma-ray bursts.

B. Detonation of a Neutron Star

We now direct our attention to the general systematics that apply to the detonation of a neutron star with mass M_n and corresponding mass parameter B_n . Since the congruence expressed in Eq. (1) can represent any normalized physical magnitude [11,12], it can express both the energies $\{C_i\}$ and mass parameters $\{B_i\}$ of the set of

particles $\{X_i\}$ involved in the neutron star decay. The normalized integer energies of these particles $\{C_i\}$, which are obtained by the calculational procedures previously described [11], are assumed to give the sum

$$C_\sigma = \sum C_i \quad (48)$$

under the constraint of momentum conservation, namely,

$$\sum A_i = 0 \quad (49)$$

Therefore, the parameter C_σ represents the total energy of the energetic decay products in the process

$$\text{NS} \rightarrow \{X_i\} \quad (50)$$

and the individual energies C_i can assume even and odd values according to the factor structures of the mass parameters of the particles involved in the decay [11]. Table II summarizes the parities of the energy parameters C_i that can be attained for different individual boson and fermi particles based on the possible arithmetic structures of the corresponding mass parameters.

Particle Mass Parameter B	Energy C: Parity	
	even	odd
Bose (odd) (2^0)	✗	✓
Fermi (even) (2^1)	✓	✗
Fermi (even) ($2^n, n \geq 2$)	✓	✓

✗ Forbidden parity of energy

✓ Allowed parity of energy

Table II: Parities of the energy parameters C for different arithmetic structures of the mass parameter B . Bose species always yield odd values; fermi systems give rise to two classes depending upon whether the necessary factor of 2 occurs either to the first ($n=1$) or to a higher ($n \geq 2$) power in the corresponding mass parameter.

In order to conserve energy for mass parameters B_n of either fermi or boson character, it follows that the energy sum C_σ given by Eq.(48) must be able to assume a corresponding even or odd parity, respectively. Inspection of the entries in Table II demonstrate that this requirement can be satisfied, but that its fulfillment will impose a complex constraint on the number of pairs involved and the detailed factor structure of the mass parameters of the participating particles. We encounter a basic arithmetic question concerning the representation of a given number B_n by a sum of terms whose forms are determined by the relativistic

energy/momentum relation and the specific factor structures of the particles produced in the final state. Since the gross physical properties of the participating particles are probably unknown, since the arithmetic structures of the corresponding mass parameters are certainly unknown, and since consideration of a neutron star requires the evaluation of this issue at an enormous ($\sim 10^{38}$) number scale, no general analytic solution to this problem is presently at hand. This matter clearly defines a central question for future study that is intimately connected with the detailed character of the particle mass scale.

C. Instability of a Neutron Star

Figure (1) schematically illustrates the energetic considerations associated with the decay of a neutron star with bose character B_n into supersymmetric pairs in accord with the final states specified by Eq. (45). This process is the sole possibility for disintegration purely into ensembles of supersymmetric pairs, the condition defined by $(m,n) = (m,1)$. For this channel, the total energies $C_{2m\sigma}$ for ensembles of zero-momentum pairs are illustrated (e.g. $C_{2\sigma}, C_{4\sigma}$). With the assumption of the pairwise conservation of momentum in Eq.(47) that expression is simplified and the corresponding energies can be readily computed [11]. An exact energy resonance $C_{2m\sigma}^*$ modulo (s) the monopole mass (P_α) for the general boson case corresponding to

$$B_n = C_{2m\sigma}^* + sP_\alpha \quad (51)$$

is also shown. Taking into account the rest energy of the 2m-pairs ($2mP_\alpha$) and defining the kinetic energy release as

$$R_{2m\sigma}^* = C_{2m\sigma}^* - 2mP_\alpha, \quad (52)$$

we can write the relation

$$R_{2m\sigma}^* = B_n - (2m+s)P_\alpha. \quad (53)$$

With the parities for the energy parameters illustrated in Table II, the integers s can assume all non-negative values ($s=0, 1, 2, \dots$). It is important to note that the known properties [11] of the solutions of the energy parameters $C_{2m\sigma}$ are clearly such that the corresponding kinetic energies $R_{2m\sigma}$ can be super-relativistic.

Equation (53) represents the condition of instability for a neutron star with bose character for the decay channel $(m,n) = (m,1)$ defined by Eq.(45) in terms of (1) the neutron star mass B_n , (2) the total kinetic energy $R_{2m\sigma}$ of the 2m supersymmetric pairs, the value of which is dependent upon the exact arithmetic structure of the mass parameters of the particles constituting these pairs [11,12], and (3) the monopole mass represented by the prime P_α . This relation can be summarized by the statement

$$R_{2m\sigma}^* \equiv B_n \pmod{P_\alpha} \quad (54)$$

for a suitable modulus parameter

$$k_\sigma = -(2m+s). \quad (55)$$

Three basic characteristics of the bose system for the pure supersymmetric channel $(m,1)$ are immediately apparent. Consider the system for $s=0$. (A) For all mass parameters

$$B_n \leq 2P_\alpha \quad (56)$$

the system is stable. The value $2P_\alpha$ is excluded in Eq. (56), since B_n for bose character is odd and $2P_\alpha$ is even. Hence, $R_{2\sigma}^* > 0$ with a minimum numerical value determined by the factor structures of particles involved, a condition consistent with the data appearing in Table II. (B) Small changes in the value of B_n can lead to relatively large variations in $R_{2m\sigma}^*$, the integer representing the energy yield of the decay. This arises naturally, since the modulus parameter k_σ is typically expected to have a very large magnitude ($k_\sigma \sim 10^{35}$). As shown in Fig. (1), this situation produces a dense set of overlapping sequences of points ($C_{2m\sigma}^*$) arising from all orders up to $2m$, a condition that enables k_σ to experience an extremely wide variation over a small range of B_n . Physically, this feature would be revealed by an exceptionally large variance in the observed yield of gamma ray bursts, a leading characteristic of this phenomena [1-3]. Indeed, a variance on the order of the average yield is consistent with both observation and the conditions given in Eqs. (54) and (55). (C) Finally, sufficiently low magnitudes of k_σ enable the yield to approach the full rest mass energy of the original body provided $B_n \gg P_\alpha$, a condition that is obviously very well satisfied for stellar systems.

We now summarize the conditions of instability determined above. The stability of a neutron star having bose character against disintegration solely into supersymmetric pairs is governed by Eqs. (54) and (55); stability is maintained unless the mass of the system B_n satisfies an exact arithmetic condition. Moreover, the precision involved is exceptionally high, since P_α and B_n respectively represent number scales [11,12] of $\sim 10^{60}$ and $\sim 10^{38}$, and a shift of unity from the condition specified is governing. In addition, since the exact values of $R_{2m\sigma}^*$ and the corresponding density of the solutions are determined by the detailed arithmetic structure of the mass parameters [11], there is a high sensitivity to the physical characteristics of the daughter particles. Finally, the key role of the monopole in relation to both supersymmetric pairing and baryon nonconservation is expressly communicated by the modulus P_α in Eq. (54).

The corresponding conditions of stability for the boson decay channel given by Eq.(44) and the two fermi amplitudes expressed by Eqs.(46) and (47) can be understood mutatis mutandis. By inspection of Eqs.(44) and

(46), systems with either bose or fermi character are stable for

$$B_n \leq P_\alpha + B_z \quad (57)$$

in which B_z denotes the mass parameter of the companion particle. Correspondingly, fermi species B_n is stable against decay though the amplitude defined by Eq.(47) for

$$B_n \leq 2P_\alpha + B_z. \quad (58)$$

From the discussion in Section II.A.3.b above, the minimum value of B_z is unity. It follows that unconditional stability against all channels involving the production of supersymmetric pairs is present for

$$B_n \leq P_\alpha, \quad (59)$$

the monopole mass.

III Conclusions

The phenomenon described above represents the conversion of cold degenerate matter at the physical scale of a neutron star directly to energetic radiation by a fundamental instability of matter that is governed by an exact physically based counting mechanism. Specifically, neutron stars can develop an instability toward spontaneous detonation with the production of super-relativistic supersymmetric pairs and particles at specific mass values. These conditions enable the violation of baryon number conservation and the resulting energy yield can approach the rest mass energy of the original body, an upper limit that incorporates the observed output of cosmic gamma-ray bursts including the very large ($\sim 10^{47} \text{ J}$) event (GRB 990123) recently detected [2,3]. Furthermore, the characteristics of the counting operation, which define the condition of instability, provide a simple explanation for the large variance in the observed energies. Further, a high neutrino yield is not mandatory in this model, a feature that both contrasts significantly with other descriptions of gamma-ray bursts and is consistent with recent experimental [28] findings indicating a low neutrino emission. In addition, the characteristics of the particle energy spectrum [11] given by Eqs.(9) and (10) can readily account for the production of the very high energy quanta [$\sim 18 \text{ GeV}$] reported [28] in connection with GRB 940217. The findings predict the existence of a maximally supersymmetry-breaking particle pair consisting of a super-light boson neutrino ν_1 , which plays a fundamental role in weak interactions, and a supermassive form of fermionic dark matter [10]. The results also support the conjecture that the empirically established phenomenon of lepton number conservation is isomorphic to the joint requirements of angular momentum conservation and the supersymmetric conservation of congruence. It is further hypothesized that

the existence of the ν_1 particle may provide an alternative theoretical basis for (1) CP violation in K_L^0 decay [8,9] and (2) the attribute of strangeness, a characteristic example of which is given by the properties of hyperon decay into nonleptonic channels. Overall, the pattern of findings that has emerged points strongly to the existence of a highly energetic realm of physical interactions that is based on supersymmetry and a new arithmetic organizing principle. Its presence imposes a form of scale invariance that enables small particles and large bodies to have similar characteristics of stability. Hence, both neutrons and neutron stars can exhibit unstable behavior.

Acknowledgments

Support for this research was partially provided under contracts with the Army Research Office (DAAG55-97-1-0310), the Department of Energy at the Sandia National Laboratories (DE-AC04-94AL85000 and BF 3611), and a Grant-in-Aid of the Ministry of Science, Culture, and Education of Japan.

Correspondences should be addressed to C.K.R. (e-mail: rhodes@uic.edu).

References

- [1] Piran, T. 1997 Toward Understanding Gamma-Ray Bursts. In *Unresolved Problems in Astrophysics*, (ed. John N. Bahcall and Jeremiah P. Ostriker), p.343. Princeton: Princeton University Press.
- [2] Kulkarni, S.R., et al. 1999 The Afterglow, Redshift and Extreme Energetics of the γ -Ray Burst of 23 January 1999. *Nature* **398**, 394.
- [3] Galama, T.J., et al. 1999 The Effect of Magnetic Fields on γ -Ray Bursts Inferred from Multi-Wavelength Observations of the Burst of 23 January 1999. *Nature* **398**, 400.
- [4] Totani, T. 1998 TeV Bursts of Gamma-Ray Bursts and Ultra-High-Energy Cosmic Rays. *Astrophys. J. Lett.* **509**, L81.
- [5] Akerlof, C. et al. 1999 Observations of Contemporaneous Optical Radiation from a γ -Ray Burst. *Nature* **398**, 394.
- [6] Irvine, J.M. 1978 *Neutron Stars*. Oxford: Clarendon Press.

- [7] Misner, C. W., Thorne, K. S., and Wheeler, J. A. 1973 *Gravitation*. San Francisco: W.H. Freeman & Co.
- [8] Gibbons, L.K., et al. 1993 Measurement of the CP-Violation Parameter $\text{Re}(\epsilon'/\epsilon)$. *Phys. Rev. Lett.* **70**, 1203.
- [9] Alavi-Harati, A., et al. 1999 Observation of Direct CP Violation in $K_{S,L} \rightarrow \pi\pi$ Decays. *Phys. Rev. Lett.* **83**, 22.
- [10] Chung, D. J. H., Kolb, E. W., and Riotto, A. 1998 Nonthermal Supermassive Dark Matter. *Phys. Rev. Lett.* **81**, 4048.
- [11] Dai, Y., Borisov, A.B., and Rhodes, C.K. 1999 Nature, Number, and Universality. *Foundations of Physics*, submitted April 1999.
- [12] Dai, Y., Borisov, A.B., Longworth, J.W., and Rhodes, C.K. 1999 Supersymmetry and a Universal Power Residue Mass Scale. *Foundations of Physics*, submitted April 1999.
- [13] Chebyshev, P.L. 1975 *Theorie der Congruenzen*. New York: Chelsea Publishing Company.
- [14] Hardy, G. H. and Wright, E. M. 1960 *An Introduction to the Theory of Numbers*, 4th edn. London: Oxford University Press.
- [15] Cohn, H. 1962 *Advanced Number Theory*. New York: Dover.
- [16] Dedekind, R. 1996 *Theory of Algebraic Numbers*. Cambridge: Cambridge University Press.
- [17] Hecke, E. 1981 *Lectures on the Theory of Algebraic Numbers*. Berlin: Springer-Verlag.
- [18] Preskill, J. 1984 Magnetic Monopoles. *Ann. Rev. Nucl. Part. Sci.* **34**, 461.
- [19] Primakoff, H. and Rosen, S. P. 1981 Baryon Number and Lepton Number Conservation Laws. *Ann. Rev. Nucl. Part. Sci.* **31**, 145.
- [20] Grosswald, E. 1985 *Representation of Integers as Sums and Squares*. Berlin: Springer-Verlag.
- [21] Dickson, L. E. 1992 *History of the Theory of Numbers*, Volumes I, II, III. New York: Chelsea Publishing Company.
- [22] Caso, C. et al. 1998 Review of Particle Physics. *European Physical Journal C3*, 1.
- [23] Sternberg, S. 1969 *Celestial Mechanics*, Part I. New York: W.A. Benjamin, Inc.
- [24] Marshak, R.E., Riazuddin, and Ryan, C.P. 1969 *Theory of Weak Interactions in Particle Physics*. New York: Wiley-Interscience.
- [25] Hardy, G. H., Littlewood, J.E., and Polya, G. 1964 *Inequalities*. Cambridge: Cambridge University Press.
- [26] Riesel, H. 1994 *Prime Numbers and Computer Methods for Factorization*, 2nd edn. Boston/Basel/Stuttgart: Birkhäuser.
- [27] Andrews, G.E. 1984 *The Theory of Partitions*. Cambridge: Cambridge University Press.
- [28] Alekseev, E.N., Alexseeva, L.N., Zakidyshev, V.N., and Poddubnyi, V.Ya. 1998 Search for Low-Energy Neutrino Radiation Accompanying Gamma-Ray Bursts on the Baksan Subterranean Scintillation Telescope, *J. Exper. Theor. Phys. (JETP)* **87**, 1041.

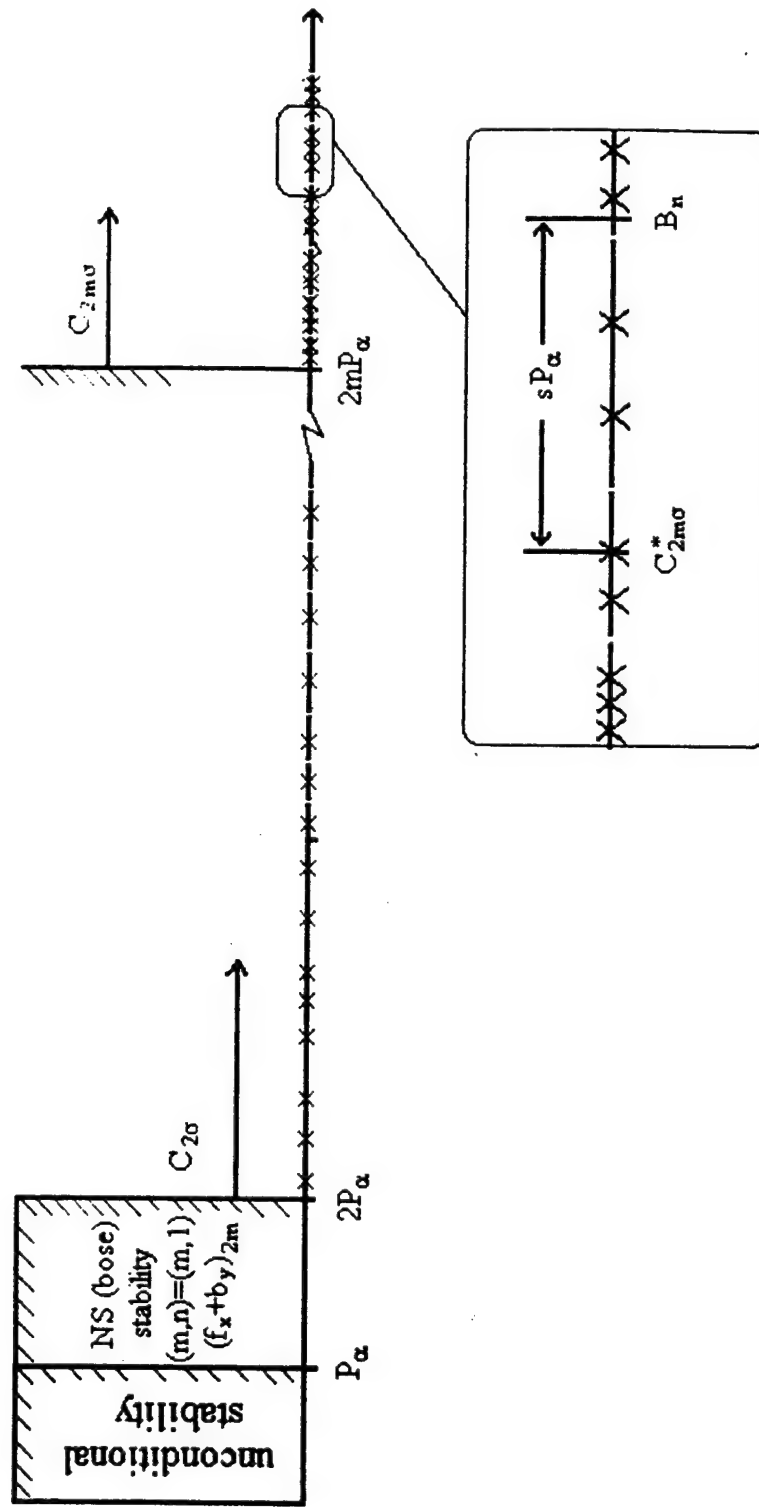


Figure (1): Schematic of the energetics associated with the detonation of a neutron star of bose character into an array of energetic supersymmetric pairs according to the channel defined by Eq. (45). A zone of stability given by Eq. (56) is indicated. Unconditional stability exists against all decay channels involving supersymmetric pairs for both fermi and bose character systems for $B_n \leq P_\alpha$. See text for discussion and definitions of the corresponding parameters.

Appendix 3

Computation with Inverse States in a Finite Field F_{P_a} : The Muon Neutrino Mass, the Unified Strong-Electroweak Coupling Constant, and the Higgs Mass

Yang Dai^{††}, Alexey B. Borisov[†], Keith Boyer[†], and Charles K. Rhodes[†]

[†]Department of Mathematical and Computing Sciences,
Tokyo Institute of Technology, Tokyo, JAPAN

[‡]Department of Physics, University of Illinois at Chicago,
Chicago, IL 60607-7059, USA

ABSTRACT

The construction of inverse states in a finite field F_{P_a} enables the organization of the mass scale with fundamental octets in an eight-dimensional index space that identifies particle states with residue class designations. Conformance with both CPT invariance and the concept of supersymmetry follows as a direct consequence of this formulation. Based on two parameters (P_a and g_a) that are anchored on a concordance of physical data, this treatment leads to (1) a prospective mass for the muon neutrino of ~ 27.68 meV, (2) a value of the unified strong-electroweak coupling constant $\alpha^* = (34.26)^{-1}$ that is physically defined by the ratio of the electron neutrino and muon neutrino masses, and (3) a seesaw congruence connecting the Higgs, the electron neutrino, and the muon neutrino masses. Specific evaluation of the masses of the corresponding supersymmetric Higgs pair reveals that both particles are superheavy ($>10^{18}$ GeV). No renormalization of the Higgs masses is introduced, since the calculational procedure yielding their magnitudes is intrinsically divergence-free. Further, the Higgs fulfills its conjectured role through the seesaw relation as the particle defining the origin of all particle masses, since the electron and muon neutrino systems, together with their supersymmetric partners, are the generators of the mass scale and establish the corresponding index space. Finally, since the computation of the Higgs masses is entirely determined by the modulus of the field P_a , which is fully defined by the large-scale parameters of the universe through the value of the universal gravitational constant G and the requirement for perfect flatness ($\Omega = 1.0$), the seesaw congruence fuses the concepts of mass and space and creates a new unified archetype.

I. Introduction

The concept of mass [1] has been an everlasting challenge to physical theory [2]. In general, an organization of the particle mass scale is sought that exhibits certain salient features. Four prominent desired characteristics are (A) the equivalence of particle P and antiparticle \bar{P} masses ($m_P = m_{\bar{P}}$), a demand of CPT invariance [3,4], (B) an expression of supersymmetry [5], a principle invoking fermion (f) /boson (b) pairing that presently exists as a very attractive theoretical hypothesis, (C) the existence of the Higgs particle [6], the entity which introduces mass into the Standard Model [7], and (D) a basis for the value of the unified strong-electroweak coupling constant α^* , the physical parameter regulating non-gravitational interactions [8].

Taken together, the two features (A) and (B) of the mass spectrum noted above incorporate three forms of two-particle associations. The requirement of CPT separately pairs both fermi (e.g. e^+/e^-) and bose (e.g. π^+/π^- and π^0/π^0) species. Supersymmetry connects the fermi and bose particle genres through the formation of corresponding supersymmetric pairs (P/P_{ss}). Therefore, these two classes of relationships produce three pairings (f/f, b/b, and b/f) yielding a system in which each particle P has both an antiparticle \bar{P} and a supersymmetric partner P_{ss} . The overall result is the construction of the particle mass scale [9] with fundamental quartets ($P, \bar{P}, P_{ss}, \bar{P}_{ss}$). Two previous studies [9,10] explicitly illustrate the manner in which this mass scale can be organized. A leading prediction of these analyses is a prospective value of 0.808 meV for the mass m_{ν_e} of the electron neutrino ν_e , a magnitude that is consistent with currently available data [11].

The present work demonstrates that the three classes of pairings associated with CPT and supersymmetry given above follow as immediate consequences of the definition of a new class of particle states designated as inverse states. This description additionally associates each particle state P with a corresponding inverse state P_{in} through a specific relationship of the particle masses. The outcome is an affiliation of four particles ($P, P_{ss}, P_{in}, (P_{in})_{ss}$), normally, but not necessarily, with nondegenerate mass values, which are further related to a corresponding quartet of antiparticles. The final result is (1) the formation of an octet of states that generally represents four distinct mass values and (2) the construction of a corresponding eight-dimensional index space that provides a system of particle classification.

This theoretical picture can be implemented by incorporating the previous analyses [9,10] into the mathematical structure of a finite field [12]. Since an algebraic field possesses the operation of division, this extension permits the definition of inverses and the corresponding construction of a set of units $\{U\}$. An important consequence is the fact that these units comprise a group structure [12]. As shown in the development below, we will be primarily concerned with the subset of fields F_p in which $P \equiv 1 \pmod{4}$, the physically motivated case [9,10,13].

The ability to define inverse states leads to several new statements concerning the organization of the mass scale and satisfaction of the four desired characteristics (A-D) listed above. Chief among the specific findings are (1) the muon neutrino mass with a predicted value of

$$m_{\nu_\mu} = 27.68 \text{ meV}, \quad (1)$$

(2) the conclusion that the unified strong-electroweak coupling constant α^* is physically defined through the electron/muon neutrino mass ratio by

$$a^* = \frac{m_{\nu_e}}{m_{\nu_\mu}} = (34.26)^{-1}, \quad (2)$$

(3) the identification of uniquely specified candidate values for the masses of a supersymmetric doublet that corresponds to the Higgs particle, and (4) a seesaw congruence that connects the electron neutrino mass, the muon neutrino mass, and the masses of the supersymmetric Higgs pair [6–8,14]. Explicit evaluation of the pair of Higgs masses indicates that both particles are in the superheavy regime ($>10^{18}$ GeV). Since the computation of the Higgs masses is intrinsically divergence-free, no renormalization [6] is necessary. The stated values of this set of fundamental parameters are consistent with the ranges of their potentially expected magnitudes [6–8,11,14–17] and all currently available experimental data. The overarching conclusion that follows from the form of the seesaw relation derived in this analysis is that the concepts of space [18,19] and mass [1,2] are fundamentally inseparable. The results state directly that these two physical archetypes constitute an identity.

II. Theoretical Development

A. Elementary Properties of Finite Fields \mathbb{F}_p

A commutative division ring is designated as a field [12]. For any prime integer P , the field \mathbb{F}_p consists of the set of residue classes

$$\{[0]_p, [1]_p, [2]_p, \dots, [P-1]_p\}. \quad (3)$$

Computations performed with elements $[x]_p$ of \mathbb{F}_p are conducted with the customary rules of arithmetic and reduction modulo the prime P . Since all primes possess primitive roots [20], power residue systems of enumeration in \mathbb{F}_p can be established and the properties of congruences [21] are central. Physically anchored procedures of counting based on these concepts were used in earlier studies to describe the organization of the particle mass scale [9,10] and the phenomenon of γ -ray bursts [22].

The existence of the operation of division enables the definition of an inverse $[x]_p^{-1}$ for every element $[x]_p$ of \mathbb{F}_p except $[0]_p$. Hence, a set of units $\{U\}$, defined by the statement

$$[x]_p [x]_p^{-1} = [1]_p, \quad (4)$$

exists and it is known that these units $\{U\}$ form a multiplicative group [12]. Furthermore, a simple general procedure exists for the calculation of the inverses $[x]_p^{-1}$ based on Fermat's Little Theorem [23]. Specifically, Fermat's result states that

$$\forall x, \gcd(x, P) = 1, [x]_p^{p-1} = [1]_p, \quad (5)$$

from which it follows directly that

$$[x]_p^{-1} = [x]_p^{p-2}. \quad (6)$$

Eq.(6) explicitly shows that an inverse $[x]_p^{-1}$ generally depends on both the value of x and the modulus P .

B. Specific Mathematical Properties of Inverses

All inverses can be computed directly through Eq.(6). However, a restricted subset of inverses has a special elementary formulation. Anticipating the need for this result below, we state the lemma specifying this set of residues and give the corresponding proof.

Lemma (1): Let P_α be prime, B_x be a divisor of $P_\alpha - 1$, and $(B_x)_{ss} = P_\alpha - B_x$.

$$\text{Then, } [(B_x)_{ss}]_{P_\alpha}^{-1} = [(P_\alpha - 1)/B_x]_{P_\alpha}.$$

Proof: By definition, $[(B_x)_{ss}]_{P_\alpha}^{-1} = [(B_x)_{ss}]_{P_\alpha}^{P_\alpha - 2}$.

$$\begin{aligned} \text{Since } (B_x)_{ss}^{P_\alpha - 2} &= (P_\alpha - B_x)^{P_\alpha - 2} = \sum_{i=0}^{P_\alpha - 2} (-1)^i \binom{P_\alpha - 2}{i} P_\alpha^{P_\alpha - 2 - i} B_x^i \\ &= -B_x^{P_\alpha - 2} + k \cdot P_\alpha \text{ for some integer } k, \end{aligned}$$

$$\text{we have } (B_x)_{ss}^{P_\alpha - 2} \equiv -B_x^{P_\alpha - 2} \pmod{P_\alpha}. \quad (7)$$

$$\text{Suppose } B_x^{P_\alpha - 2} \equiv A \pmod{P_\alpha}, \quad (8)$$

$$\text{then } -B_x^{P_\alpha - 2} \equiv P_\alpha - A \pmod{P_\alpha}. \quad (9)$$

In order to evaluate the constant A from Eq.(8), we write

$$1 \equiv B_x^{P_\alpha - 1} \equiv B_x^{P_\alpha - 2} \cdot B_x \equiv AB_x \pmod{P_\alpha}, \text{ if } \gcd(B_x, P_\alpha) = 1.$$

Therefore, $AB_x = 1 + k_x \cdot P_\alpha = (k_x + 1) + k_x(P_\alpha - 1)$ for some integer k_x .

Then $A = \frac{k_x + 1}{B_x} + k_x \frac{P_\alpha - 1}{B_x}$. Since $\frac{P_\alpha - 1}{B_x}$ is an integer by assumption, $\frac{k_x + 1}{B_x}$ must also be an integer.

Let $\frac{k_x + 1}{B_x} = N$, where N is an integer.

$$\begin{aligned} \text{Then we have } A &= N + (NB_x - 1) \frac{P_\alpha - 1}{B_x} \\ &= N + N(P_\alpha - 1) - \frac{P_\alpha - 1}{B_x} \\ &= NP_\alpha - \frac{P_\alpha - 1}{B_x}. \end{aligned}$$

From Eq.(9),

$$-B_x^{P_\alpha-2} \equiv P_\alpha - NP_\alpha + \frac{P_\alpha - 1}{B_x} \equiv \frac{P_\alpha - 1}{B_x} \pmod{P_\alpha},$$

and from Eq.(7)

$$[(B_x)_{ss}]_{P_\alpha}^{-1} = [-B_x]_{P_\alpha}^{P_\alpha-2} = [(P_\alpha - 1)/B_x]_{P_\alpha}. \quad (10)$$

Q.E.D.

Hence, B_x must be a divisor of $P_\alpha - 1$.

Lemma (1) specifies a subset of residue classes $\{B_x\}$ whose corresponding supersymmetric [9,10] partners $(B_x)_{ss}$ possess inverse states of the special form given by Eq.(10). The number of elements of the set $\{B_x\}$ is given by the arithmetic function $d(P_\alpha - 1)$, the function [24] which represents the number of divisors of the integer $(P_\alpha - 1)$. On the basis of an earlier study [13], $d(P_\alpha - 1) \approx 2.32 \times 10^{11}$. By inspection of Eq.(10), all members of $\{B_x\}$ obey the congruence

$$[B_x]_{P_\alpha} [(B_x)_{ss}]_{P_\alpha}^{-1} \equiv -1 \pmod{P_\alpha}. \quad (11)$$

The subset $\{g\}$ of elements of \mathbb{F}_{P_α} whose members are primitive roots of the modulus P_α also enjoy a select status [9,10,21,22], since these integers serve a generating function. Of particular significance will be the restricted subset $\{g_x\}$ of primitive roots such that

$$\{g_x\} = \{g\} \cap \{B_x\}. \quad (12)$$

Specifically, it will be shown below that the subset $\{g_x\}$ relates directly to both the magnitude of the unified strong-electroweak coupling constant α^* and the values for the masses of the electron and muon neutrinos. We note further that since $\{g_x\}$ can be empty, as the prime 41 demonstrates [21], the demand for the existence of a nonempty set $\{g_x\}$ constitutes an additional mathematical requirement for acceptable physical values [13] of the prime P_α .

In order to explore the needed characteristics of primitive root inverse mappings, we will initially limit our treatment to moduli of the form $P \equiv 1 \pmod{4}$ and pairs of primitive roots (g_α, g_β) that sum to the modulus P_α , the condition that expresses supersymmetry [9,10]. Further, since the Euler function $\phi(P - 1)$ is always even [24-26] for any prime $P > 3$, and a result of Gauss [27] certifies that all primitive roots of primes of the genre $P_\alpha \equiv 1 \pmod{4}$ can be arranged in supersymmetric pairs [9,10] such that

$$g_\alpha + g_\beta = P_\alpha, \quad (13)$$

it follows from Lemma (2) below that the inverse state operation given by Eq.(6) always maps a primitive root pair (g_α, g_β) according to the pattern

$$(g_\alpha, g_\beta) \rightarrow (g'_\alpha, g'_\beta) \quad (14)$$

with

$$g_\alpha \neq g'_\alpha \quad (15)$$

and

$$g_\alpha + g_\beta = g'_\alpha + g'_\beta = P_\alpha \quad (16)$$

Therefore, primitive root pairs perform transform to different primitive root pairs with both pairs in conformance with Eq.(13), the postulated mass relationship expressing supersymmetry [9,10,22]. This is an extension of the Q-pairing pattern described in an earlier study [9] of the mass scale. We now prove this important statement.

Lemma (2): Assume $g_\alpha + g_\beta = P_\alpha$, g_α, g_β are primitive roots of P_α , and P_α prime.

Let the inverses of g_α and g_β respectively be B_α and B_β .

Then, (1) $B_\alpha + B_\beta = P_\alpha$,

(2) B_α and B_β are primitive roots of P_α .

Proof: (1) can be proved by using Lemma (1) of an earlier study [9] whose proof was therein given.

Let $x = P_\alpha - 2$, an odd number.

By the previously demonstrated lemma [9], we have

$$g_\alpha^{P_\alpha-2} + g_\beta^{P_\alpha-2} \equiv 0 \pmod{P_\alpha}$$

and

$$B_\alpha + B_\beta = P_\alpha.$$

To show that both B_α and B_β are primitive roots of P_α , we use the relation

$$g_\alpha \cdot B_\alpha \equiv 1 \pmod{P_\alpha},$$

the defining statement of the inverse mapping.

For any $y \leq P_\alpha - 1$,

$$\begin{aligned} g_\alpha^y \cdot B_\alpha^y &\equiv 1 \pmod{P_\alpha} \\ g_\alpha^{P_\alpha-y-1} \cdot g_\alpha^y \cdot B_\alpha^y &\equiv g_\alpha^{P_\alpha-y-1} \pmod{P_\alpha} \\ \Leftrightarrow g_\alpha^{P_\alpha-1} \cdot B_\alpha^y &\equiv g_\alpha^{P_\alpha-y-1} \pmod{P_\alpha} \\ \Leftrightarrow B_\alpha^y &\equiv g_\alpha^{P_\alpha-y-1} \pmod{P_\alpha}, \text{ since } g_\alpha^{P_\alpha-1} \equiv 1 \pmod{P_\alpha}. \end{aligned}$$

The residue of B_α is in one-to-one relation with the residue of $g_\alpha^{P_\alpha-y-1}$. Hence, B_α is a primitive root. The corresponding result for B_β follows *mutatis mutandis*.

Q.E.D.

It follows from Lemmas (1) and (2), if either g_α or g_β is a member of $\{g_x\}$, the $(g_\alpha, g_\beta) \rightarrow (g'_\alpha, g'_\beta)$ inverse transformation is immediately calculable on the basis of the divisor structure of $P_\alpha - 1$ through Eq.(10).

C. Mass Parameter Inverse Mapping Characteristics

Scale invariance of the representation of the mass parameters is a fundamental characteristic of the power residue formulation [9,10]. Therefore, the basic features of the inverse state mapping described above can be fully illustrated with an example utilizing a prime modulus of small magnitude. Table I displays the inverse state primitive root pairings for the prime modulus $P_\alpha = 37$. We observe that one primitive root ($g_\alpha = 2$) is a divisor of $P_\alpha - 1 = 36$, so that $[g_\beta]_{37}^{-1} = 18$, the result given directly by Eq.(10). In order to show the gross characteristics of the scaling of the pairing pattern on the magnitude of the modulus, a second example of the primitive root inverse mapping is given in Table II for $P_\alpha = 73$ and it is seen that the qualitative features of the transformation are unaltered.

Two new conserved quantities are revealed by the primitive root inverse mappings illustrated in Tables I and II. The statements of the conserved magnitudes are presented in Table III. It is conjectured that these relationships correspond to the conservation of internal attributes of the particle under the inverse state operation. Further work [28] is underway to elucidate the potential physical interpretations of these conserved quantities in terms of the subgroup structure of the units of F_{P_α} .

An explicit picture of the quartet of residues representing the octet of physical particle masses $\{P, \bar{P}, P_{ss}, \bar{P}_{ss}, P_{in}, \bar{P}_{in}, (P_{in})_{ss}, (\bar{P}_{in})_{ss}\}$ can be made by further examination of the example for $P_\alpha = 37$. For this illustration, we will take $(g_\alpha, g_\beta) = (2, 35)$, one of the primitive root pairs identified in Table I. Fig. (1) shows the spectrum of these primitive roots in conjunction with the corresponding inverse state pairs $(g'_\alpha, g'_\beta) = (19, 18)$. These four generators can now be used jointly to organize both (a) the particle mass parameters and (b) the corresponding index space for state classification.

Inspection of Fig. (1) shows that the operators corresponding to the supersymmetry O_{ss} and inverse state O_{in} transformations commute, so that

$$O_{in}O_{ss} = O_{ss}O_{in}. \quad (17)$$

We also have

$$O_{in}^2 = O_{ss}^2 = 1, \quad (18)$$

the unity operator, and the inverses

$$[O_{in}]^{-1} = O_{in}, \quad [O_{ss}]^{-1} = O_{ss}, \quad (19)$$

so that $\{O_{in}, O_{ss}\}$ constitutes an abelian group.

Table IV comprehensively illustrates the mappings of the residues that arise from the four primitive roots shown in Fig. (1). The particle states, supersymmetric partners, and corresponding inverse states that occur through organization by the quartet of primitive roots are shown. In general, each residue possesses four power indices $\{t_i; i = 1, 2, 3, 4\}$ and four corresponding modulus indices $\{k_i; i = 1, 2, 3, 4\}$,

parameters which define the coordinates of the 8-dimensional space in terms of residue classes $[x]_{p_\alpha}$ designations.

Examination of Table IV demonstrates that the Q- and D-pairing motifs developed in an earlier study [9] remain. The extension of the pattern with inverse states simply adds new relationships that the four-dimensional structure could not reveal. Specifically, for power index t odd, a supersymmetric pair is coupled to a corresponding inverse supersymmetric pair (e.g. $t = 7$, $(20, 17) \leftrightarrow (13, 24)$) that preserves the Q-pairing structure. All supersymmetric primitive root pairings fall in this class, as described in Section II.B. Likewise, for power index t even, the degenerate pattern exhibited by D-pairing [9] is transferred to the corresponding inverse state pair which also exhibits D-pairing. The appropriate conjugate panels [9] are always related by a shift in the power index t by the transformation $t \rightarrow t + (P_\alpha - 1)/2$, the relation established in the earlier work [9].

INVERSE STATE PROPERTIES

Power Residue Systematics ($P_\alpha = 37$)

t	1	2	3	4	5	6	7	8	9	10
	2 35	4	8	16	32 5	27	17 20	34	31 6	25
1	13 24	26	15 22	30	23	9	18 19	36	35 2	33
2	29 8	21 24	5 32	10	20 17	3	6	12	24 13	11
3	22 15	7	14 23	28	19 18	1				

Table I: The systematics of the power residue counting system represented by $(g_\alpha, g_\beta, P_\alpha) = (2, 35, 37)$. The parameter t represents the respective integral power indices t_α and t_β . In green are the residues (B_α) for $g_\alpha = 2$ and correspondingly (B_β) in red for $g_\beta = 35$. Two patterns are apparent; the one for t odd always yields $B_\alpha + B_\beta = P_\alpha = 37$, the value coincident with $(g_\alpha + g_\beta = P_\alpha = 37)$, the condition governing supersymmetry. The remaining entries for t even always represent the degenerate condition $B_\alpha = B_\beta$. Conjugate panels are shifted $t \rightarrow t + (P_\alpha - 1)/2$ uniformly in both cases such that the respective sums give P_α . Hence, both patterns provide pairing which represents the prime modulus $P_\alpha = 37$. Every residue has an associated inverse in a field. Shown below is the subclass corresponding to the primitive root pairings for prime $P_\alpha = 37$ established by constructing units in the finite field \mathbb{F}_{37} . The primitive roots are $\{2, 5, 13, 15, 17, 18, 19, 20, 22, 24, 32, 35\}$.

<u>STATES</u> (g_α, g_β)	<u>INVERSE STATES</u> (g'_α, g'_β)
$(2, 35)$	$\xrightarrow{\hspace{1.5cm}}$
$(5, 32)$	$\xrightarrow{\hspace{1.5cm}}$
$(13, 24)$	$\xrightarrow{\hspace{1.5cm}}$
	$(19, 18)$
	$(15, 22)$
	$(20, 17)$

The inverse operation in \mathbb{F}_{37} relates conjugate panels for two distinct sets of primitive roots, thereby conferring a unique status on these four residues. For example, the inverse mapping (1) satisfies supersymmetry ($g_\alpha + g_\beta = g'_\alpha + g'_\beta = P_\alpha = 37$) and (2) the pair $(g_\alpha, g_\beta) = (2, 35)$ is transformed to $(g'_\alpha + g'_\beta) = (19, 18)$, another primitive root pair. Therefore, two distinct quartet manifolds are related by the inverse mapping for primitive root states. Hence, four $(2, 18, 19, 35)$ distinct masses are related together with a corresponding quartet of antiparticle states. Therefore, the existence of inverse states give the mass scale an extended foundation through the construction of octets and a corresponding eight-dimensional index space which classifies the particle states with residue class designations. These octets involve (A) particle/antiparticle (CPT), (B) particle/supersymmetric particle (Supersymmetry), and (C) particle/inverse particle (Unitary symmetry) relations. Generally, $[g_\alpha][g_\beta]^{-1} \equiv -1 \pmod{P_\alpha}$ and only t odd states are involved in the primitive root mappings.

Residue Mappings for Supersymmetric Primitive Root Pairs ($P_\alpha = 37$)

$$[g_\alpha]_{37} = 2, [g_\beta]_{37} = 35, [g_\alpha]_{37}^{-1} = 19, [g_\beta]_{37}^{-1} = 18$$

$t \setminus g$	35	2	18	19
1	35	2	18	19
2	4	4	28	28
3	29	8	23	14
4	16	16	7	7
5	5	32	15	22
6	27	27	11	11
7	20	17	13	24
8	34	34	12	12
9	6	31	31	6
10	25	25	3	3
11	24	13	17	20
12	26	26	10	10
13	22	15	32	5
14	30	30	21	21
15	14	23	8	29
16	9	9	33	33
17	19	18	2	35
18	36	36	36	36
19	2	35	19	18
20	33	33	9	9
21	8	29	14	23
22	21	21	30	30
23	32	5	22	15
24	10	10	26	26
25	17	20	24	13
26	3	3	25	25
27	31	6	6	31
28	12	12	34	34
29	13	24	20	17
30	11	11	27	27
31	15	22	5	32
32	7	7	16	16
33	23	14	29	8
34	28	28	4	4
35	18	19	35	2
36	1	1	1	1

Table IV: Pattern of residue classes generated by the quartet of inverse state-related primitive roots $(g_\alpha, g_\beta) = (2, 35) \xleftrightarrow{\text{inverse}} (g'_\alpha, g'_\beta) = (19, 18)$ involving the residues B, their supersymmetric partners B_{ss} , and the corresponding inverse state pairs B_{in} and $(B_{in})_{ss}$. See Fig. (1) for reference.

Power Residue Systematics ($P_\alpha=73$)

$$g_\alpha = 34, \quad g_\beta = 39, \quad g_\alpha + g_\beta = P_\alpha$$

t	1	2	3	4	5	6	7	8	9	10
0	34 39	61	30	71	5 68	24	13 60	4	63 10	25
1	47 26	65	20 53	23	52 21	16	33 40	27 27	42 31	41
2	7 66	19	62 11	64 64	59 14	35	22 51	18 18	28 45	3
3	29 44	37	17	67	15 58	72	39 34	12 12	43 30	2
4	68 5	49	60 13	69 69	10 63	48	26 47	8 8	53 20	50
5	21 52	57	40 33	46	31 42	32	66 7	54 54	11 62	9
6	14 59	38	51	55	45 28	70	44 29	36 36	56 17	6
7	58 15	1								

Primitive root pair \rightarrow its inverse

power index \rightarrow power index mapping sum

$\{5, 68\} \rightarrow \{44, 29\}$	$5 \rightarrow 67$	72
$\{11, 62\} \rightarrow \{20, 53\}$	$59 \rightarrow 13$	72
$\{13, 60\} \rightarrow \{45, 28\}$	$7 \rightarrow 65$	72
$\{14, 59\} \rightarrow \{47, 26\}$	$61 \rightarrow 11$	72
$\{15, 58\} \rightarrow \{39, 34\}$	$35 \rightarrow 37$	72
$\{31, 42\} \rightarrow \{33, 40\}$	$55 \rightarrow 17$	72

Table II: Systematics of the inverse states for the prime $P_\alpha = 73$ represented for the primitive roots

$$g_\alpha = 34 \text{ and } g_\beta = 39.$$

NEW STATES and NEW CONSERVATION LAWS

- Inverse States Define a New Symmetry Based on Supersymmetry Preserving Primitive Root Mapping
 - $(g_\alpha, g_\beta) \longrightarrow (g'_\alpha, g'_\beta)$
 $g_\alpha + g_\beta = P_\alpha, \quad g'_\alpha + g'_\beta = P_\alpha, \quad g_\alpha \neq g'_\alpha$
- Inverse State Transformations Define New Conservation Laws
 - Power Index t
 - $(g_\alpha, g_\beta) \longrightarrow (g'_\alpha, g'_\beta)$
 $t \longrightarrow t'$
$$t + t' = P_\alpha - 1$$
 - Modulus Index k
 - $$k_\alpha g'_\alpha + k'_\alpha g_\alpha \equiv 0 \pmod{P_\alpha}$$
$$k_\beta g'_\beta + k'_\beta g_\beta \equiv 0 \pmod{P_\alpha}$$
- One New Fundamental State Classification (Symmetry)
and
Two New Conserved Quantities

Table III: Inverse states define a new symmetry based on a supersymmetry preserving mapping that can be achieved with $P_\alpha \equiv 1 \pmod{4}$.

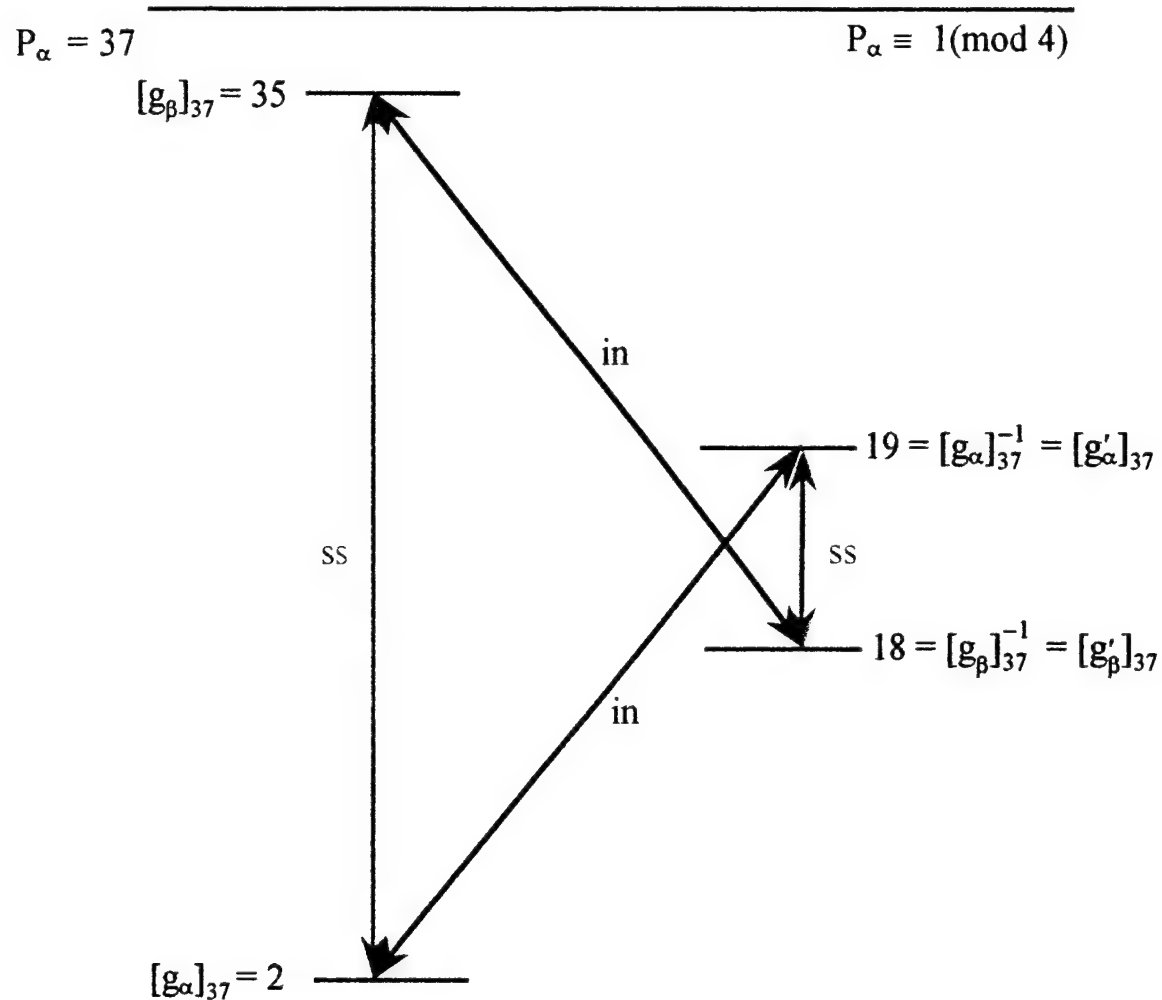


Fig. (1): Example of the spectrum of primitive roots governing the octet state manifolds for $P_\alpha = 37$. The primitive roots are $(g_\alpha, g_\beta) = (2, 35)$; the corresponding supersymmetric inverses of (g_α, g_β) are $(g'_\alpha, g'_\beta) = (19, 18)$.

III. Computational Findings

A. Muon Neutrino Mass

The results derived in Section II above can be applied to several specific computations. The use of Eq.(10) permits the determination of a mass parameter which we prospectively identify as the muon neutrino ν_μ mass m_{ν_μ} . An earlier study [9] gave an electron neutrino mass m_{ν_e} of ~ 0.808 meV, a value corresponding to the mass parameter [9,10]

$$g_\alpha = 2q = 2 \cdot 3^2 \cdot 7 \cdot 13 \cdot 31 \cdot 37 \cdot 47 \cdot 53 \cdot 59 \cdot 71 \cdot 73 \cdot 83 \cdot 107 \cdot 109 \cdot 113 \cdot 137 \cdot 139 \cdot 149. \quad (20)$$

Direct evaluation [9,10,13] showed that g_α is a primitive root of the modulus P_α , the vital property that lets it serve as a generator. Furthermore, since g_α is manifestly [13] a member of the divisor set $\{B_x\}$ of the integer

$$P_\alpha - 1 = 2^2 \cdot 3^2 \cdot 5^2 \cdot 7 \cdot 11 \cdot 13 \cdot 17 \cdot 19 \cdot 23 \cdot 29 \cdot 31 \cdot 37 \cdot 41 \cdot 43 \cdot 47 \cdot 53 \cdot 59 \cdot 61 \cdot 67 \cdot 71 \cdot 73 \cdot 79 \cdot 83 \cdot 89 \cdot 97 \cdot 101 \cdot 103 \cdot 107 \cdot 109 \cdot 113 \cdot 127 \cdot 131 \cdot 137 \cdot 139 \cdot 149 \cdot 151, \quad (21)$$

Eq.(10) of Lemma (1) can be used to compute directly the inverse of

$$g_\beta = P_\alpha - g_\alpha. \quad (22)$$

This gives

$$[g_\beta]_{P_\alpha}^{-1} = \frac{r}{2} = 2 \cdot 5^2 \cdot 11 \cdot 17 \cdot 19 \cdot 23 \cdot 29 \cdot 41 \cdot 43 \cdot 61 \cdot 67 \cdot 79 \cdot 89 \cdot 97 \cdot 101 \cdot 103 \cdot 127 \cdot 131 \cdot 151 \quad (23)$$

in which the integer r is defined in an earlier study [13]. Accordingly, on the basis of the previous work [9,10,13], we immediately recognize the specific magnitude of $[g_\beta]_{P_\alpha}^{-1}$ as a factor in the known result [13]

$$qr = (2q)(r/2) = P_\alpha - 1. \quad (24)$$

These earlier analyses [9,10,13] also demonstrated the important finding that the fine-structure constant α could be uniquely represented as

$$\alpha = \frac{q}{r} = (137.03599926808)^{-1} \quad (25)$$

and that this value is in full agreement with the measured magnitude [29,30].

In summary, Eqs. (22) and (24) can be respectively restated as

$$[g_\alpha]_{P_\alpha} + [g_\beta]_{P_\alpha} = 0 \pmod{P_\alpha}, \quad (26)$$

the additive relation representing supersymmetry [9,10] in the field F_{P_α} , and

$$[g_\alpha]_{P_\alpha} [g_\beta]_{P_\alpha}^{-1} \equiv -1 \pmod{P_\alpha}, \quad (27)$$

a corresponding multiplicative condition. However, the unusual factor structure exhibited by $[g_\beta]_{P_\alpha}^{-1}$ in Eq.(23), specifically, that $[g_\beta]_{P_\alpha}^{-1} \in \{B_x\}$, requires the special condition that $[g_\alpha]_{P_\alpha} \in \{B_x\}$ hold, an outcome legislated by Eq.(10). Only a very rare fraction of the primitive roots of P_α will satisfy this exceptional requirement and, without conformance to this condition, the crucial statements given in Eqs.(24) and (25) would not follow. For the physically relevant values [9,10,13] of P_α , this fraction is less than one in $\sim 10^{47}$.

The magnitude, smoothness, and factor structure of $[g_\beta]_{P_\alpha}^{-1}$ correspond to a light propagating particle [13] whose properties would resemble those of the electron neutrino which has been prospectively identified [9,10] with a mass parameter of g_α and a physical mass of ~ 0.808 meV. From the symmetry expressed by Eq.(27), we will provisionally assign $[g_\beta]_{P_\alpha}^{-1}$ as the mass number of the muon neutrino ν_μ .

This gives the physical mass corresponding to the muon neutrino ν_μ as

$$m_{\nu_\mu} \equiv 27.68 \text{ meV}, \quad (28)$$

a value that is consistent with both the available data and the range expected for this particle [11].

B. Unified Strong-Electroweak Coupling Constant α^*

The results presented in Section III.A above lead directly to an expression for the magnitude of the unified strong-electroweak coupling constant α^* . A previous study [9] derived the relationship

$$(\alpha^*)^{-1} = \frac{P_\alpha - 1}{g_\alpha^2} \equiv 34.26 \quad (29)$$

on the basis of characteristics of the mass scale. However, the introduction of the concept of inverse states, the results given in Eqs.(20), (22), (23), and (26), and the identification of m_{ν_μ} with the quantity $[g_\beta]_{P_\alpha}^{-1}$, enable Eq.(29) to be immediately recast in the form of the fundamental mass ratio

$$\alpha^* = \frac{m_{\nu_e}}{m_{\nu_\mu}} = \frac{[g_\alpha]_{P_\alpha}}{[g_\beta]_{P_\alpha}^{-1}} \equiv (34.26)^{-1}. \quad (30)$$

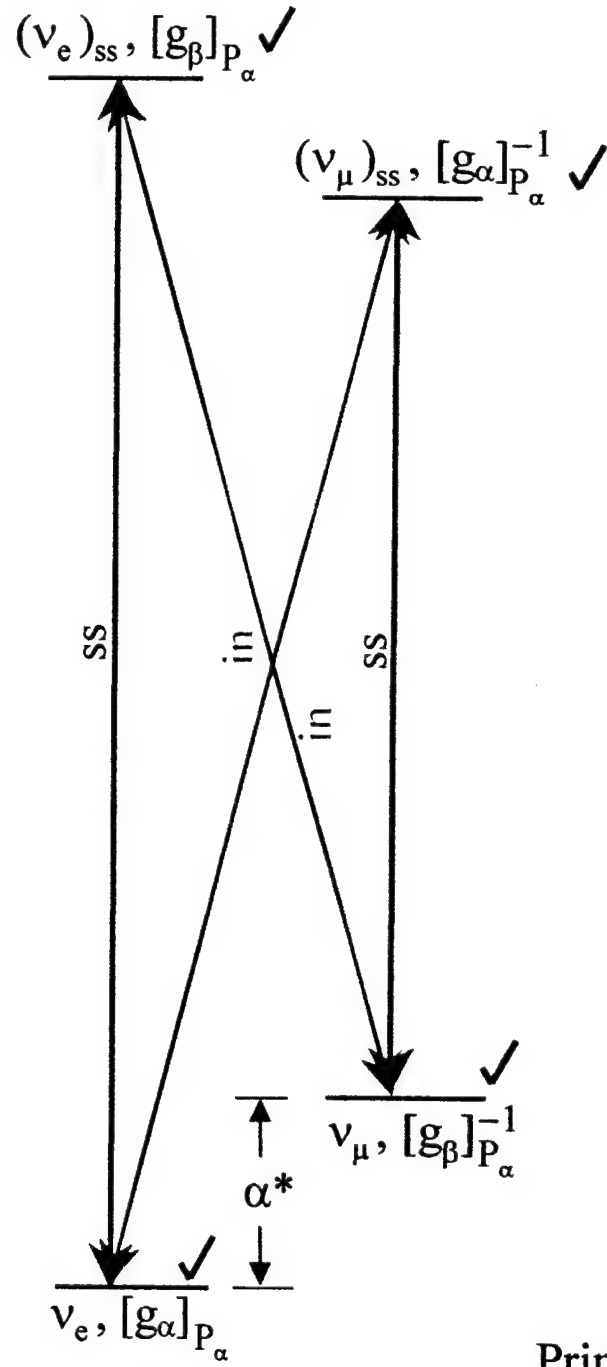
The expression given in Eq.(30) has several attractive properties. First, it gives a magnitude that stands in good correspondence with the anticipated range [7,8,16,17] of α^* . Further, it simultaneously relates the utterly basic quantity α^* mathematically to the ratio of two primitive roots that are members

of a restricted set $\{g_x\}$ of special elements in the field \mathbb{F}_{p_a} and physically to the mass ratio of two fundamental particles. Moreover, the integers $[g_\alpha]_{p_a}$ and $[g_\beta]_{p_a}^{-1}$, along with their corresponding respective supersymmetric partners $[g_\beta]_{p_a}$ and $[g_\alpha]_{p_a}^{-1}$, are all primitive roots by Lemma 2. This enables them to serve collectively as the generators of the mass scale and the organizers of the eight-dimensional index space that classifies all particle states. Fig. (2), in parallel with the model shown in Fig. (1), illustrates the relationships connecting these four primitive roots. Basic physical entities and correspondingly fundamental mathematical quantities unite to (a) construct the particle mass scale and (b) specify the magnitude of the cardinal physical parameter governing their interactions.

MASS SCALE OCTET GENERATORS

P_α, m_{mo}

$P_\alpha \equiv 1 \pmod{4}$



E_o, v_1

Primitive Root \checkmark

$$[g_\alpha]_{P_\alpha} [g_\beta]_{P_\alpha}^{-1} \equiv -1 \pmod{P_\alpha}$$

Fig. (2): Illustration of the primitive root states that organize the mass scale, construct the eight-dimensional index space, and specify the unified strong-electroweak coupling constant α^* . The magnitude of P_α represents the monopole mass m_{mo} , E_o denotes the energy unit, and v_1 a boson neutrino with a mass equal to E_o . See references [9,10,13,22] for further discussion.

C. Definition and Computation of the Higgs Mass

The analysis presented above demonstrates how the definition of inverse states extends the previously developed four-dimensional index space [9] to eight dimensions, thereby enriching its classificational capacity. Inspection of the pattern represented by the inverse states immediately identifies a fundamental degeneracy. For a particle P , it is the condition of the equality of the mass parameters for the supersymmetric P_{ss} and inverse P_{in} states; hence,

$$B_{ss} = B_{in}, \quad (31)$$

a statement signaling a point of symmetry. Furthermore, this degeneracy only occurs for two critical values of the power index

$$t_{\pm} = \frac{P_{\alpha} - 1}{2} \pm \frac{P_{\alpha} - 1}{4}. \quad (32)$$

From Eq.(32) it is apparent that the existence of the degeneracy given by Eq.(31) requires $P_{\alpha} \equiv 1 \pmod{4}$, a condition made necessary earlier by several other considerations [9,10,13]. Accordingly, this degeneracy appears in Table IV for $t = 9$ and $t = 27$. In these two cases, the residues represent the equivalent supersymmetric pairs (6, 31) and (31, 6). It can be further shown that the magnitudes of these residues are unique, since they are invariant over the full set of primitive roots of the prime P_{α} . It follows that these two residues (e.g. 6 and 31) depend solely on the value of the prime modulus P_{α} , the large scale parameter in the counting system, and obey the quadratic congruence

$$x^2 \equiv -1 \pmod{P_{\alpha}}. \quad (33)$$

Indeed, it can be shown [23] that Eq.(33) has a solution if and only if $P_{\alpha} \equiv 1 \pmod{4}$, the condition stipulated by Eq.(32). Finally, these two residues always have order 4, hence, the quartic congruence

$$x^4 \equiv 1 \pmod{P_{\alpha}} \quad (34)$$

simultaneously holds.

The unique status of these residues that is established by Eqs.(31), (32), and (33), in alliance with the fact that they depend only on the modulus P_{α} , whose value is fully determined by the large scale parameters of the universe [13], nominates these supersymmetric states as candidates for the Higgs particle. With this assignment, we can write from Eq.(33) the mass parameter of the Higgs system as

$$B_{Higgs}^2 \equiv -1 \pmod{P_{\alpha}}. \quad (35)$$

We now explore the consequences of this prospective identification.

Consider the definition of the Higgs mass presented in Fig. (3). The defining statement given by Eq.(31) is expressed by the simultaneous fulfillment of two conditions, one additive and the other

multiplicative. These conditions respectively relate (1) the supersymmetric (X,Y) pair mass distribution and (2) the inverse state definition. They are

$$[X]_{P_\alpha} + [Y]_{P_\alpha} \equiv 0 \pmod{P_\alpha} \quad (36)$$

and

$$[X]_{P_\alpha} [Y]_{P_\alpha}^{-1} \equiv -1 \pmod{P_\alpha}. \quad (37)$$

Satisfaction of Eqs.(36) and (37) leads to the statement given in Eq.(31), the degeneracy of the P_{ss} and P_{in} states and the specification of the supersymmetric residue pair uniquely dependent upon the modulus P_α .

D. Seesaw Mass Congruence

The results expressed in Eqs.(27) and (35) immediately lead to the relation

$$[g_\alpha]_{P_\alpha} [g_\beta]_{P_\alpha}^{-1} - [B_{Higgs}]_{P_\alpha}^2 \equiv 0 \pmod{P_\alpha} \quad (38)$$

and the seesaw statement

$$[g_\alpha]_{P_\alpha} [g_\beta]_{P_\alpha}^{-1} \equiv [B_{Higgs}]_{P_\alpha}^2, \quad (39)$$

HIGGS MASS DEFINITION

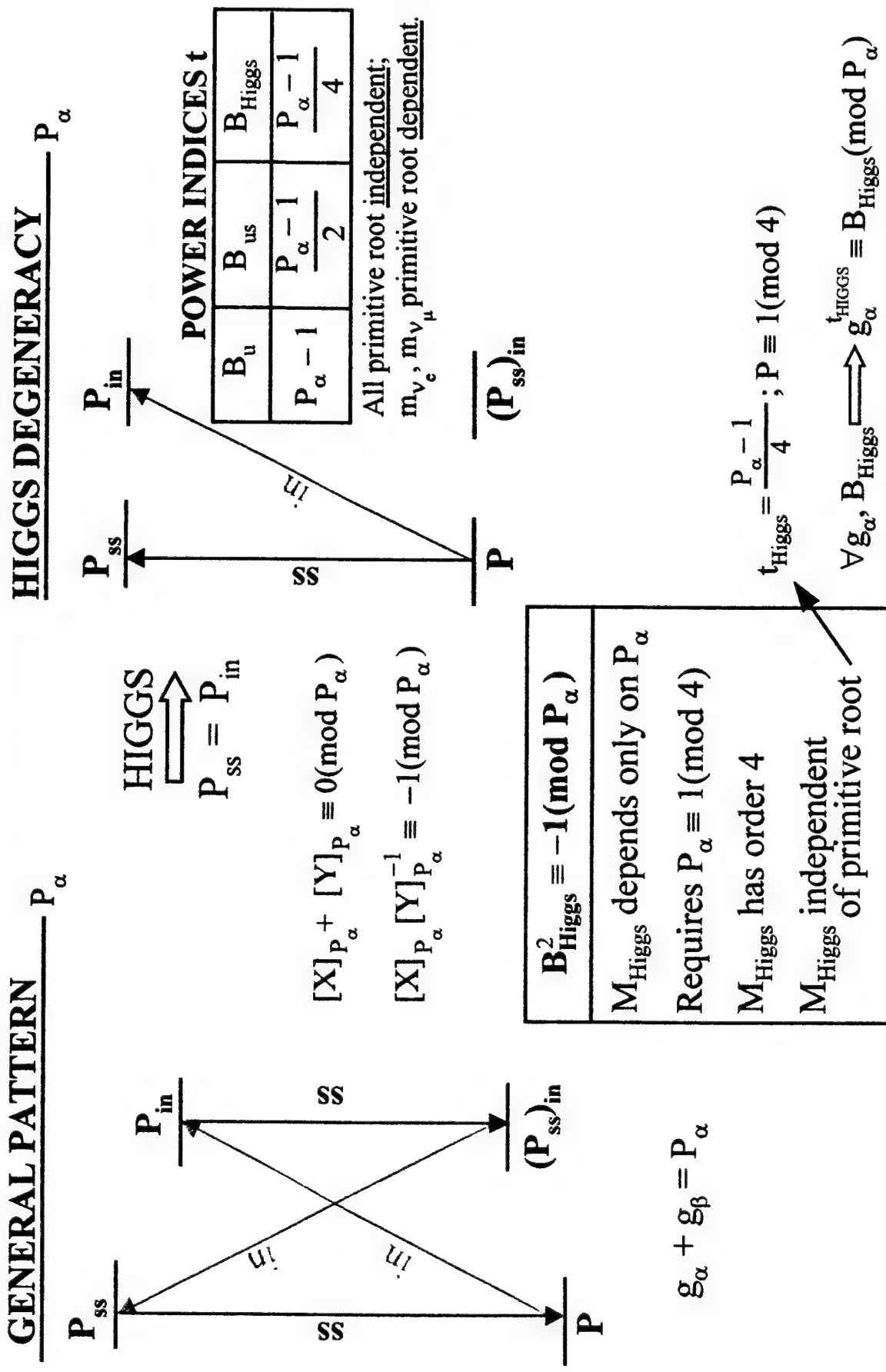


Fig. (3): Defining condition for the supersymmetric Higgs particle.

a fundamental expression that connects the electron neutrino mass, the muon neutrino mass, and the masses of the supersymmetric Higgs pair. Importantly, since Eq.(39) is written as a congruence, it holds simultaneously for the masses of both particles comprising the supersymmetric Higgs system.

An explicit evaluation of the Higgs masses can be made, since g_α and P_α are known [9,10,13] from Eqs.(20) and (21), and the critical power indices t_\pm are given by Eq.(32). In order to simplify the calculation, we can use the smallest primitive root of P_α , which has the value $g_{\min} = 14$, since the residues corresponding to the supersymmetric Higgs pair are independent of the primitive root and depend only on the modulus P_α . Hence, we evaluate the congruence

$$\frac{P_\alpha - 1}{g_{\min}^4} \equiv B_{\text{Higgs}} \pmod{P_\alpha} \quad (40)$$

and obtain the mass parameter of the Higgs boson as

$$B_{\text{Higgs}}^b = 5295067887317048385691240239639344309098972470130691907921115, \quad (41)$$

an integer composed of the factors

$$5, 13, 31, 109, 677, 25717, 165235181, 3158418359, \\ 5645180551, 470014220572174240309. \quad (42)$$

The mass parameter presented in Eq.(41) gives a physical mass of $\sim 9.56 \times 10^{18}$ GeV. The corresponding supersymmetric Higgs fermion is then found directly by the condition for supersymmetry through

$$B_{\text{Higgs}}^f = P_\alpha - B_{\text{Higgs}}^b \\ = 1464518162437886934175466847230415731421582430740004414836186, \quad (43)$$

a mass parameter having the factor structure

$$2, 3, 29, 37, 344353, 204901219, 14323448690905379, \\ 225085635424845454780404199 \quad (44)$$

and representing a physical mass of $\sim 2.64 \times 10^{18}$ GeV. Consequently, both members of the supersymmetric Higgs doublet possess masses $> 10^{18}$ GeV. These results given by Eqs. (41) and (43) were confirmed by a calculation using the primitive root g_α . Therefore, since the two neutrino species have a lower bound on their masses (< 30 meV) and the Higgs particles are both superheavy ($> 10^{18}$ GeV), we find that Eq.(39) contains no representative of an intermediate scale (~ 100 GeV) mass. This outcome contrasts sharply with customary seesaw relationships [31] developed originally from Lagrangian field theory [11,32,33]. The modular seesaw given by Eq.(39) expresses a fundamentally different physical conclusion. Further, since the mathematical procedures used to compute the Higgs

mass with Eq.(40) are entirely divergence-free, no renormalization is necessary, a second result that highlights the contrast with findings derived by customary quantum field theoretical methods [6–8,34,35].

The seesaw congruence given by Eq.(39) expresses a deep connection between the concepts of space and mass. In particular, Eq.(39) states that the Higgs system specifies the set of generators $\{g_\alpha, g_\beta, g_\alpha^{-1}, g_\beta^{-1}\}$ of the mass scale illustrated in Fig. (2). The mass parameters corresponding to the supersymmetric Higgs doublet cannot be generators themselves, since they satisfy the quadratic congruence given by Eq.(35) and are thereby barred from status as primitive roots of P_α . Further, since the magnitudes of the Higgs residues are determined in Eq.(40) solely by the value of the modulus P_α , the seesaw congruence finds the generators of the particle masses directly on the large scale characteristics of space. Hence, the cosmic seesaw creates a new archetype by expressing the fusion of the concepts of space and mass.

E. Higgs Mass and the Many-Body Problem

Quantum field theoretical procedures have been applied to the computation of the Higgs mass [6–8,34,35]. Electroweak theory requires quantum loop corrections that are intrinsically divergent and lead to an estimate of the Higgs mass that is in the superheavy regime ($> 10^{16}$ GeV). Basically, the underlying theory has a many-body character and these corrections are a manifestation of that feature. Hence, the calculation of the Higgs mass in quantum field theory is a basic many-body problem, an outcome that reflects the fundamental nature of the Higgs mechanism and our concept of the vacuum [19].

The result expressed by Eq.(40) for the mass parameters of the supersymmetric Higgs doublet is an exact value obtained by mathematical procedures that do not admit a perturbative approach [13]. With the assumption that the problem is properly formulated, the only result obtainable is the unique correct solution. In the approach using finite fields that leads to Eq.(40), this occurs because of the large number of hidden constraints that are present. Basically, the solution is gridlocked by the combined influence of the magnitude and the factor structure of the integer. This exceptional intolerance to computational approximation follows as a consequence of the profound influence of unity, at any number scale, on the factor structure of integers. Therefore, since there exists no neighborhood about the exact result in which an approximation is meaningful, the procedures of perturbation theory are invalid.

We conclude with a statement of the obvious conjecture, namely, that the counting procedure intrinsic to the theoretical framework provided by a finite field automatically and perforce yields the exact solution to a properly posed many-body problem. Further, if this conjecture holds for the Higgs particle, we may expect that is valid for any system, potentially even proteins. In the case of proteins, the verification of this conjecture would allow a fundamental reformulation of the protein folding problem, a central question of immense importance in biology and medicine.

III. Conclusions

The construction of inverse states in a finite field \mathbb{F}_p enables the organization of the mass scale with fundamental octets in an eight-dimensional index space that classifies particle states with residue class designations. Conformance with both CPT invariance and the concept of supersymmetry follows as a direct consequence of this formulation. Based on two parameters (P_α and g_α) that are anchored on a concordance of physical data embracing both large scale cosmic parameters and small scale couplings [9,10,13], this analysis leads to (1) a prospective mass for the muon neutrino of ~ 27.68 meV, (2) a value

of the unified strong-electroweak coupling constant $\alpha^* = (34.26)^{-1}$ that is physically defined by the electron and muon neutrino mass ratio, and (3) a seesaw congruence connecting the Higgs, the electron neutrino, and the muon neutrino masses. Specific evaluation of the masses of the corresponding supersymmetric Higgs pair reveals that both particles are superheavy ($>10^{18}$ GeV). No renormalization of the Higgs masses is necessary, since this theoretical approach intrinsically excludes the possibility of divergences. Further, the Higgs fulfills its conjectured role through the seesaw relation as the particle defining the origin of all particle masses, since the mass parameters of the electron and muon neutrino systems, together with their supersymmetric partners, are the generators of the mass scale and the corresponding index space. Finally, since the computation of the Higgs masses is entirely determined by the modulus P_α , which is fully defined by the large-scale parameters of the universe through the value [36] of the universal constant G and the requirement [9,10,13,37] for perfect flatness ($\Omega = 1.0$), the cosmic seesaw congruence provides an explicit unifying statement for the concepts of mass [1,2] and space [18,19]. As inseparable entities in this picture, these two physical archetypes constitute an identity. This outcome mirrors the fundamental connection between space and geometry in general relativity.

Acknowledgements

The authors respectfully acknowledge many insightful conversations with James W. Longworth. Support of this research was partially provided under contracts with the Army Research Office (DAAG55-97-0310), the Department of Energy at the Sandia National Laboratories (DE-AC04-94AL85000 and BF3611), and a Grant-in-Aid of Ministry of Education, Science, Sport, and Culture of Japan.

Correspondences should be addressed to CKR (e-mail: rhodes@uic.edu).

REFERENCES

1. Max Jammer, *Concepts of Mass* (Harvard University Press, Cambridge, 1961).
2. Max Jammer, *Concepts of Mass in Contemporary Physics and Philosophy* (Princeton University Press, Princeton, 2000).
3. J. J. Sakurai, *Invariance Principles and Elementary Particles* (Princeton University Press, Princeton, 1964).
4. C. Caso et al., "Review of Particle Physics," *European Physical Journal C3*, 1 (1998).
5. J. Wess and J. Bagger, *Supersymmetry and Supergravity* (Princeton University Press, Princeton, 1983).
6. John F. Gunion, Howard E. Haber, Gordon Kane, and Sally Dawson, *The Higgs Hunter's Guide* (Addison-Wesley Publishing Co., Redwood City, Ca, 1990).
7. M. K. Gaillard, P. D. Grannis, F. J. Sciulli, "The Standard Model of Particle Physics," *Rev. Mod. Phys.* 71, S96 (1999).
8. Frank Wilczek, "Quantum Field Theory," *Rev. Mod. Phys.* 71, 585 (1999).
9. Y. Dai, A. B. Borisov, J. W. Longworth, K. Boyer, and C. K. Rhodes, "Systematics of a Supersymmetric Power Residue Particle Mass Scale," manuscript in preparation.
10. Y. Dai, A. B. Borisov, J. W. Longworth, and C. K. Rhodes, "Supersymmetry and a Universal Power Residue Mass Scale," manuscript in preparation.
11. *New Era in Neutrino Physics*, edited by H. Minokata and O. Yasuda (Universal Academy Press, Inc., Tokyo, 1999).
12. Rudolfo Lidl and Harold Niederreiter, *Finite Fields*, Vol. 20 of the *Encyclopedia of Mathematics and Its Applications*, edited by G. -C. Rota (Cambridge University Press, Cambridge, 1997).
13. Y. Dai, A. B. Borisov, and C. K. Rhodes, "Nature, Number and Universality," manuscript in preparation.
14. Marcela Carena, John Conway, Howard Haber, and John Hobbs, Report of the Higgs Working Group, Version 4, 8 March 2000; <http://fnth37.fnal.gov/susy.html>
15. Jonathan L. Feng, Konstantin T. Matchev, and Takeo Moroi, "Multi-TeV Scalars Are Natural in Minimal Supergravity," *Phys. Rev. Lett.* 84, 2322 (2000).
16. J. L. Lopez, D. V. Nanopoulos, and A. Zichichi, "Status of the Superworld from Theory to Experiment," CERN-PPE/94-01, (6 January 1994).
17. J. Ellis, "Unification and Supersymmetry," *Phil. Tran. Roy. Soc. A* 310, 279 (1983).
18. Max Jammer, *Concepts of Space* (Harvard University Press, Cambridge, 1961).
19. *The Philosophy of the Vacuum*, edited by S. Saunders and H. P. Brown (Clarendon Press, Oxford, 1991).
20. Harvey Cohn, *Advanced Number Theory* (Dover Publications, Inc., New York, 1962).
21. P. L. Tschebyscheff, *Theorie der Congruenzen* (Chelsea Publishing Co., New York, 1972), p.3.
22. Y. Dai, A. B. Borisov, J. W. Longworth, K. Boyer, and C. K. Rhodes, "Gamma-Ray Bursts and the Particle Mass Scale," Proceedings of the International Conference on Electromagnetics in Advanced Applications, edited by R. Graglia (Politecnico di Torino, Torino, 1999).
23. Kenneth Ireland and Michael Rosen, *A Classical Introduction to Modern Number Theory*, Second Edition (Springer-Verlag, Berlin/Heidelberg/New York, 1998).

24. G. H. Hardy and E. M. Wright, *An Introduction to the Theory of Numbers*, Fourth Edition (Oxford University Press, London, 1900).
25. Lindsay N. Childs, *A Concrete Introduction to Higher Algebra*, Second Edition (Springer-Verlag, New York/Berlin/Heidelberg, 1995).
26. H. Riesel, *Prime Numbers and Computer Methods for Factorization*, Second Edition (Birkhäuser, Boston/Basel/Stuttgart, 1994).
27. L. E. Dickson, *History and the Theory of Numbers, Volumes I, II, and III* (Chelsea Publishing Co., New York, 1992).
28. Yang Dai, Alexey B. Borisov, Keith Boyer, and Charles K. Rhodes, "Determination of Supersymmetric Physical Masses with Genetic Divisors," manuscript in preparation.
29. T. Kinoshita, "New Value of the α^3 Electron Anomalous Magnetic Moment," *Phys. Rev. Lett.* 75, 4728 (1995).
30. Peter J. Mohr and Barry N. Taylor, "CODATA Recommended Values of the Fundamental Physical Constants: 1998," *J. Phys. Chem. Ref. Data* 28, 1713 (1999).
31. M. Gell-Mann, P. Raymond, and R. Slansky, in *Supergravity*, edited by D. Freedman and P. van Nieuwenhuizen (North Holland, Amstredam, 1979), p. 315; T. Yanagida in Proceedings of the Workshop on Unified Theory and Baryon Number in the Universe, edited by O. Sawada and A. Sugamoto (KEK, Tsukuba, Japan, 1979); R. Mohapatra and G. Senjanovic, *Phys. Rev. Lett.* 44, (1980), p. 912 and *Phys. Rev. D23*, (1981) p. 165.
32. F. Boehm and P. Vogel, *Physics of Massive Neutrinos* (Cambridge University Press, Cambridge, 1987).
33. Boris Kayser with Françoise Gibrat-Debu and Frederic Perrier, *The Physics of Massive Neutrinos* (World Scientific, Singapore, 1989).
34. Manuel Drees, "An Introduction to Supersymmetry," APCTP-5, KEK-TH-501, November 1996; hep-ph/9611409 25 Nov 1996.
35. Hitoshi Marayama, "Supersymmetry Phenomenology," arXiv:hep-ph/0002232 v2 4 Mar 2000.
36. J. Shaw, F. Noltig, & W. Kündig, "Gravitational Constant Measured by Means of a Beam Balance," *Phys. Rev. Lett.* 80, 1142, 1998.
37. P. de Bernardis et al., "Boomerang Collaboration" and A. Lange et al., <http://xxx.lanl.gov/astro-ph/0005004>.

Appendix 4

An efficient, selective collisional ejection mechanism for inner-shell population inversion in laser-driven plasmas

W. Andreas Schroeder, T.R. Nelson[†], A.B. Borisov, J.W. Longworth, K. Boyer,
and C.K. Rhodes

*Department of Physics (M/C 273), University of Illinois at Chicago,
845 W. Taylor Street, Chicago, IL 60607-7059, USA*

Abstract

A theoretical analysis of laser-driven collisional ejection of inner-shell electrons is presented to explain the previously observed anomalous kilovolt L-shell x-ray emission spectra from atomic Xe cluster targets excited by intense sub-picosecond 248nm ultraviolet radiation [A. McPherson *et al.*, *Nature* **370**, pp. 631-634 (1994)]. For incident ponderomotively-driven electrons photoionized by *strong* above threshold ionization, the collisional ejection mechanism is shown to be highly *l*-state and significantly *n*-state (i.e. radially) selective for time periods shorter than the collisional dephasing time of the photoionized electronic wavefunction. The resulting preference for the collisional ejection of *2p* electrons by an ionized *4p* state produces the measured anomalous Xe(L) emission which contains *direct* evidence for (*i*) the generation of Xe²⁷⁺(*2p*⁵*3d*¹⁰) and Xe²⁸⁺(*2p*⁵*3d*⁹) ions exhibiting inner-shell *population inversion* and (*ii*) a *coherent* correlated electron state collision responsible for the production of double *2p* vacancies. For longer time periods, the selectivity of this coherent impact ionization mechanism is rapidly reduced by the combined effects of intrinsic quantum mechanical spreading and dephasing – in agreement with the experimentally observed and extremely strong $\sim\lambda^{-6}$ pump-laser wavelength dependence of the efficiency of inner-shell (*2p*) vacancy production in Xe clusters excited in underdense plasmas [K. Kondo *et al.*, *J. Phys. B* **30**, pp. 2707-2716 (1997)].

[†] Present address: Sandia National Laboratories, MS-1188, P.O. Box 5800,
Albuquerque, NM 87185-1188

Tel: (312) 996-2974

FAX: (312) 996-9016

E-mail: andreas@uic.edu

I. Introduction

Several methods have been previously evaluated in attempts to generate *coherent* radiation in the extreme ultraviolet (XUV) and x-ray spectral regions. Most notable amongst these are: high-order harmonic generation [1-3]; discharge-pumped soft x-ray lasers [4]; laser-pumped recombination [5,6], electron-impact ionization [7,8], and hybrid collision-recombination [9] sources; x-ray [10] and ponderomotively-generated Larmor radiation [11] excited emitters; and Thomson scattering sources [12]. However, none of these methods have been successful at generating coherent radiation with a brightness in excess of $10^{30} \text{ fs}^{-1}(\text{mrad})^2(\text{mm})^2(0.1\% \text{ BW})^{-1}$ at a wavelength $\lambda < 10\text{\AA}$; that is, a *kilovolt* x-ray brightness level sufficient for interferometric biological imaging capable of providing an atomic-level resolution visualization of the molecular anatomy of cells, tissues and organisms in the natural state [13]. Indeed, to date, kilovolt x-ray imaging applications have been limited to static [14] and dynamic [15] differential absorption measurements and time-resolved diffraction experiments [16] using *incoherent* radiation from laser-driven plasmas. Moreover, practical limitations in the generation of high-power sub-5-fs laser pulses and the spectral merging of harmonic orders above ~ 200 may preclude the development of a high brightness source of $>1\text{keV}$ photons by high harmonic generation techniques, while a recent analysis of linear and nonlinear (i.e. multiple) electron-photon interactions [17] suggests that Thomson scattering sources may never reach a brightness level sufficient for a ground-breaking interrogation of living organisms.

A potentially very effective method of producing an extremely bright source of kilovolt x-ray radiation would be to generate a *controlled* population inversion in the inner shells of high-Z atoms, i.e. produce *specific* species of “hollow atoms” [18]. In this paper, we outline a mechanism for achieving precisely this type of population inversion in laser-driven plasmas. The mechanism is based on the *selective* collisional ionization of inner-shell electrons by ponderomotively-driven electrons initially photoionized by *strong* above threshold ionization (ATI) [19]. The selectivity relies on the fact that the wavefunction of a photoionized electron distribution maintains its phase and geometric symmetry for a time shorter than the characteristic collisional dephasing time which, by comparison with electron-electron scattering rates in semiconductors [20,21], is of the order of one femtosecond (10^{-15}s). Consequently, if the photoionized wavefunction collides with an ion or atom within this time period, the matrix element associated with the collision will be dominated by the intrinsic dynamics of the quantum mechanical spreading of the photoionized atomic orbital. In stark contrast to a “plane-wave” collision, this results in a strong angular momentum (l - and m -state) and a significant radial (n -state) dependence in the selectivity of the interaction. Laser-driven classically free electrons in the

plasma [9] cannot exhibit this selectivity, since their wavefunctions contain no information about the atomic orbitals from which they were ionized.

The essential features of the selective collisional ionization mechanism will be discussed in Section III using the interaction of ponderomotively-driven $4p$ electrons photoionized from Xe with the bound state electrons of Xe ions as an example. The results of this theoretical analysis are shown to be in good agreement with the observed *anomalous* Xe(L) spectra described in Section II, which were obtained under intense ultraviolet (UV) 248nm laser irradiation of 5-20 atom Xe cluster targets [22,23]. Specifically, it explains the strongly preferred generation of $2p$ vacancies in Xe cluster targets; a process leading naturally to the observed evidence for (i) a laser-driven generation of Xe ions exhibiting population inversion between the $2p$ and $3d$ shells and (ii) the production of multiple $2p$ vacancies [18]. Furthermore, for gaseous targets such as Xe clusters, the mechanism displays a substantial pump-laser wavelength scaling favoring the use of shorter wavelength driving sources - in agreement with the experimental determination of at least a λ^{-6} scaling in the efficiency of Xe L-shell (2.5-3.1Å) emission between 248nm and 800nm laser excitation [24,25]. The possible extension of this technique to the selective generation of $1s$ vacancies in Kr for strong $\sim 1\text{\AA}$ K-shell emission is explored in Section IV.

II. Xe L-Shell Emission

Arguably the strongest experimental evidence supporting the existence of an anomalous selective laser-driven collisional ionization mechanism comes from the L-shell ($3d \rightarrow 2p$) *hollow-atom* emission observed from atomic Xe clusters [18] under intense irradiation (10^{18} - 10^{19}W/cm^2) by sub-picosecond ultraviolet (UV) terawatt ($1\text{TW} = 10^{12}\text{W}$) laser pulses at 248nm generated by a hybrid Ti:Sapphire/KrF* laser system [26]. As described elsewhere [18,23,25,27-29], these TW UV laser pulses are focused by an $f/3$ optic into a target of Xe clusters (typically of 5-20 atoms) generated by a cooled pulsed valve. A mica-crystal von H  mos spectograph equipped with Kodak RAR 2492 x-ray film and appropriate filters was used to collect the spectrum of the x-ray radiation emitted by the irradiated target. As shown in Figure 1, the kilovolt Xe L-shell spectra detected under these experimental conditions displays the characteristic double peaked hollow-atom structure of the $3d \rightarrow 2p$ transition [30]. It is important to note that this Xe(L) emission must be generated by a collisional mechanism in which photoionized electrons are accelerated by the laser field to a sufficient energy to eject an inner-shell $2p$ electron via Coulombic interaction. This is because the Xe $2p$ state, which has an ionization potential of $\sim 8\text{keV}$, cannot be directly photoionized by above threshold ionization (ATT) [19] at irradiances below 10^{22}W/cm^2 .

However, a fully relativistic classical model of the photoionized electron trajectories for 248nm irradiation at 10^{18} - 10^{19} W/cm 2 [25] has shown that the ponderomotively-driven electrons ionized from more weakly bound orbitals can return to their cluster of origin with an energy of 10-20keV; a value sufficient to eject 2p electrons collisionally and thus produce the observed L-shell emission.

A striking feature of the spectra shown in Fig. 1 is the strong L-shell emission due to single 2p-shell vacancies from Xe^{+q} ions for charge states of $q = 27$ to 37 corresponding to $2p \leftarrow 3d$ transitions ranging from a *filled* 3d-shell ($2p^63d^9 \leftarrow 2p^53d^{10}$) to one containing only one electron ($2p^6 \leftarrow 2p^53d$) respectively. This observation is very unusual in light of the magnitudes of the cross-sections evaluated from a single-electron *plane-wave* analysis for the collisional ejection of inner-shell electrons with an ionization potential $I_p > 250\text{eV}$ [31,32]. As shown in Figure 2, a *plane-wave* collisional analysis indicates that an electron incident on a Xe ion with a collisional energy E_{coll} of 10-20keV is ~ 10 times more likely to eject a 3d, 3p, or 3s electron with ionization potentials of ~ 2 - 3keV than a 2p electron with $I_p \approx 8\text{keV}$. This analysis is clearly in *stark* contradiction to the experimental observations of Fig. 1 on two grounds. First, it would predict that Xe(L) emission from Xe^{+q} ions should be approximately an order of magnitude less than that from $\text{Xe}^{+(q+1)}$ ions, ultimately suggesting that on average all 3d electrons should suffer collisional ejection before a *single* 2p electron is ejected. Consequently, the experimental observation of significant L-shell emission from Xe^{27+} with a *filled* 3d shell (i.e. a $2p^63d^9 \leftarrow 2p^53d^{10}$ transition) indicates that the collisional cross-section for ejection of a 2p electron could be at least an order of magnitude *larger* than that for the ejection of a 3d electron under 248nm UV irradiation at 10^{18} - 10^{19} W/cm 2 ; that is, precisely the inverse of the scaling associated with the plane-wave collisional analysis. And second, it suggests that a significant number of 3p and 3s vacancies should also be generated by the collisional mechanism ejecting the 2p electrons. Yet, strong emission from ionic species possessing such vacancies has not been observed.

More anomalous, given the plane-wave collisional analysis, is the observation of spectral features associated with *double* 2p vacancies in the range 2.60-2.65Å (Fig. 1) [18,22,23]. This result is even more astonishing when one considers the fact that the lifetime of a single 2p vacancy is only $\sim 1.8\text{fs}$ [32,30]. This means that the generation of 2p vacancies in the collisional ejection mechanism must be occurring at a rate in excess of $\sim 10^{15}\text{s}^{-1}$; that is, effectively producing multiple 2p vacancies *within* one optical cycle of the 248nm pump-laser radiation used in the experiment. Previous analyses [28,33,34] have suggested that this could be accomplished by *ordered* or *cooperative* ponderomotive electronic motions in which Z photoionized electrons behave as a single quasi-particle of charge Ze with an effective collective energy Z times their individual mean

energy. For example, the cooperative action of 3-4 electrons under 248nm UV irradiation at 10^{18} - 10^{19} W/cm² would certainly enhance the probability of collisional $2p$ vacancy generation by ensuring that the quasi-particle has an effective collisional energy of \sim 40keV, i.e. near the peak of the $2p$ cross-section (Fig. 2). However, such a mechanism fails to explain the apparent selective generation of $2p$ vacancies with a rate exceeding the production of other multiple inner-shell vacancies (e.g. $2s$, $3s$, and $3p$ vacancies) in the Xe ions.

It is also interesting to note that a comparison experiment conducted with a TW femtosecond Ti:sapphire laser system operating in the infrared (IR) at 800nm did *not* reveal the generation of multiple $2p$ vacancies in the observed Xe L-shell emission [24,25]. Moreover, the overall strength of the L-shell emission was observed to be three orders of magnitude (\sim 3000x) weaker under IR irradiation. Consequently, any plausible collisional ionization mechanism must (*i*) be selective in nature in order to explain the anomalous features of the Xe(L) emission outlined above under UV irradiation and (*ii*) be consistent with the experimental data obtained at both pump-laser wavelengths. Evidently, the latter effect could arise directly from a strong scaling with the laser excitation wavelength, specifically the pump-laser radiation period.

III. Selective Collisional Ionization

III.A. Interaction Geometry and Matrix Element

The cross-section for any collisional interaction is proportional to the modulus square of the matrix element M_{fi} associated with the interaction mechanism [35] which, for an initial state $|i\rangle$ coupled to a final state $|f\rangle$ through the interaction potential V , is written as

$$M_{fi} = \langle f | V | i \rangle \quad (1)$$

In our case, we are interested in the collisional ejection of bound inner-shell electrons by a ponderomotively-driven photoionized electron through the action of the Coulomb potential. The general interaction geometry for this collision is shown in Figure 3. The bound states $|\phi_i\rangle$ are defined by the radial coordinate r_i centered on the nucleus of the target atom or ion. The displacement vector \mathbf{R} describes the trajectory of the center (centriod) of the photoionized electron distribution (or state) during the motion determined by the laser's oscillating ponderomotive potential and the Coulomb potential of the ionized atomic cluster [25,36]. The

internal radial coordinate of the photoionized electron wavefunction $|\psi\rangle$ is given by \mathbf{r}_2 so that $\mathbf{R} + \mathbf{r}_2$ defines the position of the ionized electron with respect to the target ion. Within this framework, the initial state $|i\rangle$ can be written as

$$\langle \mathbf{r} | i \rangle = \phi_i(\mathbf{r}_1) \psi(\mathbf{r}_2, t) \exp[i\mathbf{k}_0 \cdot (\mathbf{R} + \mathbf{r}_2)] ; \quad (2)$$

that is, as the product of the incident ponderomotively-driven time-dependent photoionized wavefunction $\langle \mathbf{R} + \mathbf{r}_2; t | \psi \rangle$, for which \mathbf{k}_0 is the wavevector associated with its motion, and the stationary inner-shell electronic states of target atom or ion $|\phi_j\rangle$. In the limit of a sufficiently long time after the interaction, the final state $|f\rangle$ for the scattered and ejected inner-shell electrons may be well represented as the product of two spherical waves emanating from the origin of the coordinate system centered on the target atom (Fig. 3):

$$\langle \mathbf{r} | f \rangle = \frac{\exp[i\mathbf{k}_1 \cdot \mathbf{r}_1]}{r_1} \frac{\exp[i\mathbf{k}_2 \cdot \mathbf{r}_2]}{r_2} . \quad (3)$$

Here, \mathbf{k}_1 and \mathbf{k}_2 are the wavevectors of the ejected and scattered incident electrons *after* the collision respectively. Thus, since the collisional ejection mechanism is subject the momentum conservation condition $\mathbf{k}_0 = \mathbf{k}_1 + \mathbf{k}_2$ and the vector $\mathbf{r}_1 - (\mathbf{R} + \mathbf{r}_2)$ describes the displacement between the two electrons involved in the Coulomb interaction, the matrix element associated with the interaction is of the form

$$M_{if} = \iiint d^3\mathbf{r}_1 d^3\mathbf{r}_2 d\mathbf{R} \frac{\phi_i(\mathbf{r}_1) \psi(\mathbf{r}_2, t)}{r_1 r_2 |\mathbf{r}_1 - (\mathbf{R} + \mathbf{r}_2)|} \exp[i\mathbf{k}_0 \cdot \mathbf{R} - i\mathbf{k}_1 \cdot (\mathbf{r}_1 - \mathbf{r}_2)] . \quad (4)$$

In general, the full exact calculation of this matrix element is highly complex [37,38]. Accordingly, for the scope of this paper, we will develop a suitable approximate analysis based upon the fact that the $1/r$ dependence of the Coulomb potential will strongly select collisional interactions between $|\psi\rangle$ and $|\phi_j\rangle$ for which $\mathbf{R} \approx 0$, i.e. interactions for which the center of the photoionized state $|\psi\rangle$ passes close to the nucleus of the target ion. Consequently, the essential physics behind the cross-section for inner-shell collisional ejection is expected to be obtained from an evaluation of $|M_{if}(\mathbf{R} = 0)|^2$. In particular and notwithstanding this approximation, it is immediately evident from equation (4) that the strength of the matrix element will be strongly dependent upon the overlap between $|\psi\rangle$ and $|\phi_j\rangle$; that is, the form of $|\psi\rangle$ since the bound states $|\phi_j\rangle$ are known. Specifically, the *spherical* symmetry of the incident photoionized wavefunction

$|\psi\rangle$ with respect to the target wavefunctions $|\phi_j\rangle$ should play a major role in determining the collisional cross-sections for *particular* inner-shell ejection mechanisms. Hence, as in atom-atom and ion-atom collisions [39], the interaction is expected to have strong geometrical features associated with the electronic charge distributions of $|\psi\rangle$ and $|\phi_j\rangle$.

III.B. Temporo-Spatial Dynamics of Photoionized Electron Wavefunctions

Before the collision of the electron with the target atom or ion, it must first be photoionized and then accelerated by the pump laser field. For laser irradiances above $\sim 10^{17} \text{ W/cm}^2$, such as those of $10^{18}\text{-}10^{19} \text{ W/cm}^2$ required to generate the observed Xe(L) emission (Fig. 1), above threshold ionization (ATI) is the dominant ionization process [19]. Moreover, under our experimental conditions, the incident UV pump-laser radiation is observed to undergo relativistic self-focusing, resulting in channelled beam propagation over more than 100 Rayleigh ranges [40]. Numerical simulations of the self-focusing mechanism have indicated that significant self-steepening of the leading edge of the laser pulse occurs over irradiances of $\sim 10^{17}\text{-}10^{22} \text{ W/cm}^2$ as it propagates down the channel [41]. As a result, the conditions of photoionization experienced by the irradiated atoms or ions are expected to be highly dynamic. In particular, it is very probable that the photoionization mechanism closely follows the "ionization ignition" model of Rose-Petrucci et al. [42] where *entire* orbital shells may be ionized by ATI at the peak laser field in each half cycle of the radiation. Thus, for our experimental irradiances of $10^{18}\text{-}10^{19} \text{ W/cm}^2$, we may make the ansatz that the free electronic state is initially a *replica of the photoionized bound state* $|\phi_j\rangle$, i.e. the bound state is simply "tipped" out of the atomic or ionic potential by the perturbing ponderomotive potential of the strong laser field in $\sim 0.1 \text{ fs}$. Consequently, immediately after photoionization at $t = 0$, we may write within this "sudden approximation" that

$$\langle \mathbf{r}_2; t = 0 | \psi \rangle \approx \langle \mathbf{r}_1 | \phi_j \rangle. \quad (5)$$

It follows that the initial photoionized electronic state $\langle \mathbf{r}_2; t = 0 | \psi \rangle$ possesses the angular and radial characteristics of $|\phi_j\rangle$, namely $R(r)Y_{lm}(\theta, \phi)$ where $R(r)$ and $Y_{lm}(\theta, \phi)$ are the usual radial eigenfunctions and spherical harmonics for a central Coulomb potential respectively. As a direct consequence, one would expect $\langle \mathbf{r}_2; t = 0 | \psi \rangle$ to exhibit substantial *p*-wave symmetry within the irradiance range of $10^{18}\text{-}10^{19} \text{ W/cm}^2$ under which the Xe(L) emission of Fig. 1 was observed, since the six-electron Xe $4p$ state with an ATI threshold of $\sim 2 \times 10^{18} \text{ W/cm}^2$ is one of the last states to be photoionized at these levels of irradiance.

The initially ionized state $\langle \mathbf{r}_2; t = 0 | \psi \rangle$ is subsequently accelerated in the ponderomotive potential of the oscillating laser field **Ecosor** [25,43]. This process is usually described by the expansion of $|\psi\rangle$ in terms of Volkov states $|\phi_\mu\rangle$ [44], the eigenstates of the ponderomotive potential;

$$|\psi\rangle = \sum_\mu |\phi_\mu\rangle \langle \phi_\mu | \psi \rangle . \quad (6)$$

However, the expansion coefficients $\langle \phi_\mu | \psi \rangle$ are generally not explicitly evaluated since, as we will demonstrate, the ionized electronic wavefunction evolves into phase-unrelated Volkov states $|\phi_\mu\rangle$ in a timescale significantly less than the 3-4fs radiation period of the most commonly used high-power IR laser systems [45]. The resulting loss of information on both the initial phase and symmetry of $|\psi\rangle$ does not allow any possible selectivity in collision process due to the details of the spatial overlap of the returning electron wavefunction $\langle \mathbf{r}_2; t | \psi \rangle$ with the bound states $|\phi_j\rangle$ of the target atom or ion to be treated. Furthermore, to the authors' knowledge, the explicit time evolution of the photoionized state $|\psi\rangle$ due to intrinsic quantum mechanical spreading and collisional dephasing (due to internal scattering amongst the electrons in the ionized state $|\psi\rangle$) has not been previously considered. The evaluation of these effects and their affect on collisional ionization interactions is a crucial feature of the analysis presented in this paper.

The intrinsic quantum mechanical spreading of the initial wavefunction $\langle \mathbf{r}_2; t = t_0 | \psi \rangle$ during the acceleration by the laser field can be readily treated within its internal coordinate system \mathbf{r}_2 in the *single* non-interacting electron limit. This is because we expect the spreading of $|\psi\rangle$ to be essentially radial since $\langle \mathbf{r}_2; t = 0 | \psi \rangle$ originated from a bound state $|\phi_j\rangle$ in a *central* potential. In other words, the symmetry dictated by the spherical harmonic $Y_{lm}(\theta, \phi)$ of the ionized state $|\phi_j\rangle$ is predominantly preserved in $\langle \mathbf{r}_2; t | \psi \rangle$ since no torque is applied. Thus, to a first-order approximation, the time evolution of $|\psi\rangle$ may be written as [35]

$$\langle \mathbf{r}_2; t | \psi \rangle = \langle \mathbf{r}_2(t), \theta, \phi | \psi \rangle ; \mathbf{r}_2(t) \approx \mathbf{r}_{20} \left(1 + \frac{t^2}{\tau^2} \right)^{-\frac{1}{2}} , \quad (7)$$

where r_{20} is the original radial coordinate and $\tau = ma^2/\hbar$ is the characteristic time for the radial-width a of the wavefunction's initial probability distribution to increase to $\sqrt{2}$ of its initial value. For example, the wavefunction for an electron photoionized from the Xe 4p state, which has a

bound radius of $\sim 0.7\text{\AA}$, will double its width in $\sim 0.07\text{fs}$, i.e. in a *fraction* of a femtosecond! More significantly, when the photoionized Xe $4p$ electron returns to collide with its cluster of origin after one 0.8fs period of the 248nm radiation, $|\psi\rangle$ has expanded to a radius of $\sim 14\text{\AA}$. This is to be compared to the typical $\sim 10\text{\AA}$ diameter 10-20 atom Xe cluster size used as the target material in the experiments generating the observed Xe(L) emission shown in Fig. 1. Thus, since the photoionized electron trajectory at irradiances of $10^{18}\text{-}10^{19}\text{W/cm}^2$ is known to come back through the cluster near its center [25], the expanded wavefunction is *optimally sized* to interact with *all* the atoms in the Xe cluster. This optimal geometrical coupling condition for collisional ionization of inner-shell electrons from the Xe atoms in the cluster will be degraded at longer laser excitation wavelengths. For example, upon return to the target atoms in the cluster under 800nm IR laser excitation (optical period of 2.7fs), $|\psi\rangle$ would be ~ 3 times broader so that its central probability amplitude $\langle r_2 \approx 0 | \psi \rangle$ is reduced by a factor of 5-6. In turn, this should result in more than an order of magnitude reduction in the cross-section for the collisional ejection of *any* bound state $|\phi_j\rangle$ from the a Xe target atom/ion.

In addition to the intrinsic quantum mechanical spreading, the photoionized wavefunction $|\psi\rangle$ will also be dephased (i.e. loose its initial coherence) by collisional scattering. For sufficiently strong ATI, where all electrons in an entire orbital are simultaneously ionized [42], the dominant scattering mechanism will be *internal* electron-electron collisions within the photoionized state $\langle r_2, t | \psi \rangle$. Classically, this process results in a “Coulomb explosion” of the photoionized electron distribution [25] which converts of the shape of the initial *coherent* wavefunction $\langle r_2, t = 0 | \psi \rangle$ into *incoherent* spherical waves originating, on average, from the center of the ionized electron distribution. In other words, this process is primarily responsible for the transition into the regime where a plane-wave analysis of the collisional ejection of inner-shell electrons becomes valid.

We may estimate the electron-electron scattering rate γ_{ee} for this dephasing mechanism by comparison with the large body of experimental work on carrier-carrier collisions in semiconductors. In particular, the observations of Portella *et al.* [20] and Becker *et al.* [21] indicate that the electron-electron scattering rate in bulk GaAs increases with the cube root of the carrier density, i.e. $\gamma_{ee} \approx A_{\text{GaAs}} n^{0.33}$ where $A_{\text{GaAs}} \approx 3.7 \times 10^5 \text{m/s}$. Adjusting for the effective electron mass of GaAs ($m^* = 0.067 m_0$ [46], where m_0 is the free electron rest mass), we obtain a value of $\sim 1 \text{\AA/fs}$ for A_0 in a vacuum. Thus, for the maximal simultaneous photoionization by ATI of *all* six electrons of the Xe $4p$ state in an initial volume with a radius of $\sim 0.7\text{\AA}$, we would expect an initial scattering rate of around $1\text{-}2 \times 10^{15} \text{s}^{-1}$, corresponding to a characteristic electron-electron

scattering time of 0.5-1fs. This initial scattering time is roughly a factor of 5 longer than the characteristic time associated with the intrinsic quantum mechanical spreading of the photoionized wavefunction. Consequently, the $4p$ wavefunction photoionized from a solitary Xe ion spreads faster than it dephases. This means that it is possible for a significant fraction of the photoionized $4p$ state to remain coherent during the ponderomotive acceleration over one radiation period before returning to interact with its parent Xe cluster.

The fraction f of the photoionized state $\langle r_2; t | \psi \rangle$ that remains coherent as a function of time may be estimated by incorporating the reduction in the rate of internal electron-electron collisional dephasing caused by the spreading of the $|\psi\rangle$ into a rate equation of the form

$$\frac{\partial f}{\partial t} = -A_0 n_0^{0.33} f \left(1 + \frac{t^2}{\tau^2} \right)^{-\frac{1}{2}}, \quad (8)$$

where n_0 is the initial electron density of the photoionized wavefunction. The solution to this equation, subject to the initial generation by ATI of a totally coherent state (i.e. $f = 1$ at $t = 0$), is

$$\ln f = -A_0 n_0^{0.33} \tau \ln \left[\frac{t}{\tau} + \sqrt{1 + \frac{t^2}{\tau^2}} \right]. \quad (9)$$

For the photoionized Xe $4p$ orbital with six electrons initially in a radius of $\sim 0.7\text{\AA}$, this analysis indicates that the ionized state $\langle r_2; t | \psi \rangle$ will be 30-40% coherent when it returns to interact with its cluster of origin after the 0.8fs radiation period of 248nm laser excitation [25]. As a result, an accurate description of the collisional ejection mechanism generating the spectrally observed $2p$ vacancies (Fig. 1) must incorporate a *non-plane-wave* component. Such considerations may even be necessary for 800nm IR irradiation since equation (9) suggests that the $4p$ orbital is still 20-30% coherent after the longer 2.7fs radiation period, even though $\langle r_2; t | \psi \rangle$ is now substantially more spread out. However, this intra-orbital analysis does not consider dephasing due to inter-orbital electron-electron scattering which will begin to contribute to the decoherencing of $\langle r_2; t | \psi \rangle$ once the expanding photoionized states from different atoms in the cluster begin to overlap. The scattering rate due to this inter-orbital interaction is estimated to be $0.5-1\text{fs}^{-1}$, which suggests that the electron wavefunction may be almost completely dephased upon returning to interact with its cluster of origin when the driving radiation period exceeds $\sim 2\text{fs}$, i.e. for pump-laser wavelengths greater than $\sim 600\text{nm}$.

III.C. Angular Momentum Selectivity in Collisional Ejection Mechanism

The above analysis of the temporo-spatial dynamics of the photoionized wavefunction clearly indicates that inner-shell impact ionization due to incident Xe 4p electrons under 248nm laser excitation could be primarily affected by the residual coherence of the spreading $\langle \mathbf{r}_2; t | \psi \rangle$ rather than plane-wave collisions resulting from a dephased $\langle \mathbf{r}_2; t | \psi \rangle$. Accordingly, in the rest of this paper we will examine the physics behind such a *coherent* “orbital”-orbital collisional ionization process [38,39].

With a knowledge of the form of the expanding and ponderomotively-driven photoionized wavefunction $\langle \mathbf{r}_2; t | \psi \rangle$ given in equation (7), the essential physics behind the matrix element M_{fi} associated with the collisional ejection of an electron in the bound state $\langle \mathbf{r}_1 | \phi_j \rangle$ by the photoionized electron state may be readily determined for the case when $\mathbf{R} = 0$. In this limit, equation (4) reduces to

$$M_{fi}(\mathbf{R} = 0) = \iint d^3 \mathbf{r}_1 d^3 \mathbf{r}_2 \frac{\phi_j(\mathbf{r}_1) \psi(\mathbf{r}_2, t)}{r_1 r_2 |\mathbf{r}_1 - \mathbf{r}_2|} \exp[-i\mathbf{k}_1 \cdot (\mathbf{r}_1 - \mathbf{r}_2)], \quad (10)$$

which may be solved analytically using the expansion [47]

$$\frac{e^{i\kappa|\mathbf{r}_1 - \mathbf{r}_2|}}{4\pi|\mathbf{r}_1 - \mathbf{r}_2|} = i\kappa \sum_{L=0}^{\infty} j_L(\kappa r_<) h_L^{(1)}(\kappa r_>) \sum_{M=-L}^L Y_{LM}^*(\theta_2, \phi_2) Y_{LM}(\theta_1, \phi_1), \quad (11)$$

where $j_L(\kappa r)$ are spherical Bessel functions of order L , $h_L^{(1)}(\kappa r)$ are Hankel functions of the first kind of order L , and $\kappa = -k_1 \cos\beta$ with β equal to the angle between \mathbf{k}_1 and the vector $\mathbf{r}_1 - \mathbf{r}_2$. As with other collisional interactions [35,37], the matrix element M_{fi} is a function of the details of the collision dynamics, that is \mathbf{k}_1 through κ .

We will begin by considering the collision physics associated with the angular contribution to $M_{fi}(\mathbf{R} = 0)$ in the integrand of equation (10). Here, it is important to note that, unlike the direction of $\mathbf{r}_1 - \mathbf{r}_2$, the direction of the ejected electron's momentum $\hbar\mathbf{k}_1$ cannot be explicitly related to the integration variables $\theta_1, \phi_1, \theta_2$, and ϕ_2 . Instead, the allowed directions of \mathbf{k}_1 are determined solely by the momentum and energy conservation in the collision. As a result,

the angle β between \mathbf{k}_1 the vector $\mathbf{r}_1 - \mathbf{r}_2$ must be considered as a random variable in the evaluation of $M_{fi}(\mathbf{R} = 0)$ so that, for example, the energy conservation condition for the ejection of an inner-shell electron with an ionization potential I_p may be written as

$$k_0^2 - \frac{2mI_p}{\hbar^2} = k_2^2 + 2\kappa^2 , \quad (12)$$

since, on average, $\cos^2 \beta = \frac{1}{2}$. It is then manifest that the form of the angular integrations involved in M_{fi} imply a strong *angular momentum selectivity* to the collisional ejection of inner-shell electrons. Specifically, if one is interested in the collisional ejection of an electron from a bound state $|\phi_j\rangle$ with an orbital angular momentum quantum number l , then the insertion of equation (11) into equation (10) ensures that only the $L = l$ term of the Coulomb expansion contributes to M_{fi} (the θ_1 integration), and thence, that the collisional cross-section is non-zero *only* if the incident photoionized electronic state $\langle \mathbf{r}_2; t | \psi \rangle$ has an angular momentum component of $l\hbar$ in the collision (the θ_2 integration). Alternatively, if the ponderomotively-driven incident wavefunction $\langle \mathbf{r}_2; t | \psi \rangle$ is predominantly a state with a particular orbital angular momentum quantum number, then *strong l-state selectivity* will result in the collisional ejection mechanism.

This type of l -state selectivity in the collisional ionization process is clearly in agreement with the observation of strong Xe L-shell emission from Xe^{30+} ions under intense 10^{18} - 10^{19} W/cm² UV laser excitation (Fig. 1). In particular, unlike the plane-wave collisional analysis, it explains the generation of $2p$ vacancies in Xe ions which have all their $3s$ and a substantial fraction of their $3d$ electrons remaining. This is because, for laser irradiances $\geq 2.5 \times 10^{18}$ W/cm², sufficiently strong ATI can simultaneously photoionize the entire Xe $4p$ shell to generate an initial 6-electron state of the form

$$\langle \mathbf{r}_2; t = 0 | \psi \rangle = r_2 R_{41}(r_2) \sum_{m=-1}^1 Y_{lm}(\theta_2, \phi_2) . \quad (13)$$

After approximately one period of the driving laser radiation, the time-evolving state $\langle \mathbf{r}_2; t | \psi \rangle$ returns to interact with the Xe atoms in its cluster of origin [25]. Under 248nm UV laser excitation with a 0.8fs radiation period, the 30-40% of the returning wavefunction $\langle \mathbf{r}_2; t | \psi \rangle$ which is still coherent with its initial photoionized $4p$ state $\langle \mathbf{r}_2; t = 0 | \psi \rangle$ will predominantly collisionally eject a bound electron from a state with the same spherical harmonic $Y_{lm}(\theta, \phi)$, i.e. a p -state electron with $l = 1$. The matrix elements with all other bound states $|\phi_j\rangle$ with $l \neq 1$ will be

severely suppressed since the spreading of $\langle \mathbf{r}_2; t | \psi \rangle$ has mostly preserved its *p*-wave character. For longer radiation periods, such as the ≈ 3 fs period of near IR laser radiation, this *l*-state selectivity in the collisional ejection process is expected to be sharply reduced by intra- and inter-orbital electron-electron scattering which destroy the symmetry of the initial photoionized state $\langle \mathbf{r}_2; t = 0 | \psi \rangle$, thus rapidly and progressively returning the inner-shell ejection process to the customary plane-wave regime. However, the coherent nature of the collisional interaction may not be completely destroyed, as evidenced by the observation of weak, yet identifiable, L-shell emission from Xe ions with charge states between 27+ and 29+ (Fig. 1); i.e. Xe ions with filled 3s and mostly filled 3d orbitals.

III.D. Multiple Inner-Shell Vacancy Production

It is interesting to note that, in addition to the *l*-state selectivity, *m*-state selectivity is also expected in the *coherent* inner-shell collisional ejection mechanism. This arises because the strong electric field from the exciting laser radiation imposes a preferred axis to the interaction through the Stark effect. As a result, the angular integrations over ϕ_1 and ϕ_2 ensure that a *non-zero* matrix element $M_{fi}(\mathbf{R} = 0)$ for the collisional ejection of an electron from a particular bound state $|\phi_j\rangle$ exists only when the incident photoionized state $\langle \mathbf{r}_2; t | \psi \rangle$ has a component of the same azimuthal angular momentum as $|\phi_j\rangle$. Since the Coulomb interaction is spin invariant, this has an important consequence for the shell-selective collisional ejection process: namely, that it is possible for the two electrons in the same *l*- and *m*-state of $\langle \mathbf{r}_2; t | \psi \rangle$ to act *collectively* (or coherently) [28,33,34] to collisionally eject two inner-shell electrons with the *identical* orbital angular momentum and magnetic quantum numbers. Such a collision between two correlated anti-symmetric spin states of the form $\frac{1}{\sqrt{2}}(|\frac{1}{2}, -\frac{1}{2}\rangle - |-\frac{1}{2}, \frac{1}{2}\rangle)$ in the target and photoionized wavefunctions has the *same* value of the matrix element M_{fi} as the single electron-electron collisional ejection mechanism in the absence of dephasing effects. Thus, the generation of *double m*-state vacancies by this selective coherent process is *only* 4 times less likely than the production of single vacancies – there being 4 possible single electron-electron collisions for each *l*- and *m*-state selective interaction. This ratio of single to double vacancy production is to be contrasted to a ratio of 10^3 - 10^4 for the collision of high *Z* atoms (*Z* > 20) with high energy quanta [48]. This difference is expected since the coherent ejection mechanism is more reminiscent of the orbital-orbital interactions of ion-atom collisions [38,39].

At first glance, one would expect the collision producing a double vacancy to be more affected by dephasing effects than the single-vacancy-generating interaction since, for the former, *both*

electrons in the particular m -state of $\langle \mathbf{r}_2; t | \psi \rangle$ must remain coherent. However, to a good first approximation, this is not the case within a single photoionized orbital, because the most likely electron-electron collision will occur between electrons in the closest spatial proximity; that is, between the spin pair in the same m -state wavefunction. Clearly, this dominant collisional dephasing process will have an *equal* effect on the rates of both single and double vacancy production, resulting in an approximately fixed ratio of single to double vacancy production of 4. For atomic cluster or solid targets, the overlap between expanding photoionized wavefunctions from neighboring atoms or ions, and consequent inter-orbital dephasing collisions, will cause this ratio to increase. However, the experimental evidence of Fig. 1 indicates that the ratio of the peak emission strengths from Xe ions with single and double 2p vacancies is only ~ 5 , suggesting that the inter-orbital scattering rate may be less than 0.5fs^{-1} and thus not a strong effect for short-period UV laser excitation. The observation of strong double 2p vacancy production in Xe clusters excited by 248nm radiation, therefore, provides direct evidence for a *coherent* (or *correlated*) collisional ejection mechanism. Moreover, the lack of the same spectral signature under 800nm IR laser excitation, where the longer radiation period only serves to further “mix” and dephase the expanding ionized states $\langle \mathbf{r}_2; t | \psi \rangle$, is clearly consistent with such a mechanism.

III.E. Radial Selectivity in the Matrix Element

To fully account for the experimentally observed anomalous Xe L-shell emission spectra (Fig. 1), the proposed coherent inner-shell ionization mechanism must also display significant n -state (or radial) selectivity in addition to the strong angular momentum selectivity discussed above. Specifically, it must explain the observed lack of strong 3p ejection when the incident ponderomotively-driven state $\langle \mathbf{r}_2; t | \psi \rangle$ originated from a photoionized 4p orbital at UV irradiances of 10^{18} - 10^{19}W/cm^2 . This follows because the experimental designation and calculational verifications of the charge states in the observed Xe(L) emission from 2p vacancies support the conclusion that the 3p shell is intact. In other words, the collisional cross-section for the ejection of a 2p electron by the proposed mechanism should be greater than that for the ejection of a 3p electron, a result that stands in contradiction to the conventional plane-wave collisional analysis (Fig. 2). Since this type of selectivity cannot be l or m dependent, it must be due to radial dependence of the matrix element $M_{fi}(\mathbf{R} = 0)$.

Evaluation of the radial contribution to the matrix element M_{fi} for $\mathbf{R} = 0$ requires knowledge of the radial forms of both the initially ionized wavefunction $\langle \mathbf{r}_2; t = 0 | \psi \rangle$ and the bound states $|\phi_j\rangle$ of the target ion. In order to simplify this calculation, we will approximate these states by suitably

scaled (to account for screening) hydrogenic wavefunctions [35]. Figure 4 compares the computed normalized hydrogenic wavefunctions $rR(r)$ (dashed curves) with those obtained from an exact calculation (solid curves) [49] for the $2p$, $3p$, and $4p$ radial orbitals of atomic Xe. The relatively good agreement in all three cases allows the matrix element $M_f(R = 0)$ to be evaluated analytically to a high precision. The slight disagreement on the form of the outer lobe of the $4p$ orbital accounts for less than a 2% error in the calculation, since (i) the $1/r$ dependence of V_c suppresses its contribution relative to the first two lobes and (ii) the overlap of the outer lobe of the $4p$ state with the $3p$ and $2p$ orbitals is minimal. Moreover, the rapid radial expansion of the $4p$ orbital after ATI ensures that effectively only the inner two of its well-represented radial lobes contribute to the matrix element after a time $t > 2\tau \approx 0.14\text{fs}$. In fact, for small laser-excited Xe clusters, where the photoionized electrons return to interact with their cluster of origin after one radiation period (i.e. after a time $t/\tau > 10$) [25], essentially only the first radial lobe of the expanding $4p$ orbital overlaps with both the bound $2p$ and $3p$ states for $R = 0$. In addition, it should be noted that the use of the radial forms of the $2p$, $3p$, and $4p$ states for a Xe atom rather than an Xe^{+q} ion of the appropriate charge should not affect the evaluation of the matrix element significantly. This is because the basic shape of both the tightly-bound inner-shell $2p$ and $3p$ states and the innermost first two lobes of the $4p$ state, which dominate the collisional ejection mechanism, should not be significantly perturbed for typical charge states of $q \approx +30$ generated at the experimental excitation irradiances of $10^{18}\text{-}10^{19}\text{W/cm}^2$.

The result of evaluating the radial integration of the matrix element for the collisional interaction in equation (8) using the hydrogenic $2p$, $3p$, and incident expanding $4p$ wavefunctions is shown in Figure 5. The value of $|M_f(R = 0)|^2$, which is directly proportional to the collisional cross-section for the selective ejection mechanism, is plotted as a function of the normalized time t/τ given by equation(7) and $\kappa = k_1 \cos\beta$ for the collisional ejection of the bound $2p$ and $3p$ states in Figs. 5(a) and (b) respectively. Three features are readily apparent. First, in contrast to the plane-wave collisional analysis (Fig. 2) [32], the cross-section for $3p$ ejection is less than that for the impact ionization of a $2p$ electron at equivalent values of t/τ and κ . Second, as expected, the cross-section for the impact ionization of inner-shell electrons decreases in time due to the reduction in the collisional overlap integral caused by the temporal spreading of the photoionized state $\langle r_2; t | \psi \rangle$. Third, the cross-section is also a strong function of κ with slower, less energetic collisions being favored for $t/\tau \geq 10$. Physically, the latter trend may be understood in terms of the collision time – a less energetic collision allowing for a longer time period for the wavefunctions representing the electron states to interact. Mathematically, it is a direct consequence of the form of the Bessel function product $j_1(\kappa r)h_1^{(1)}(\kappa r)$ in equation (11) which,

for sufficiently large values of κ , has a more rapid oscillation with r than the $2p$ and $3p$ bound state wavefunctions (Fig. 4), thus reducing the value of $|\mathcal{M}_{fi}(\mathbf{R} = 0)|^2$.

To quantify the first two observations, we will examine in more detail the interaction conditions leading to the L-shell spectra of Fig. 1 emitted by Xe clusters under 248nm UV and 800nm IR laser excitation. From the relativistic analysis of Ref. 25, a photoionized electron state $\langle \mathbf{r}_2, t | \psi \rangle$ will return to its cluster of origin with a collision energy of $\sim 15\text{keV}$ after approximately one radiation period for both pump-laser wavelengths at the experimental irradiances of 10^{18} - 10^{19}W/cm^2 . With this information, the most probable average value of κ for an inner-shell ejection process may be calculated using equation (12) and assuming the equipartition of the energy available after the collision between the scattered and ejected electrons. For the ejection of a $2p$ electron with an ionization potential $I_p \sim 8\text{keV}$, this calculation gives $\kappa \approx 21\text{\AA}^{-1}$, whereas for $3p$ vacancy production we have $\kappa \approx 28\text{\AA}^{-1}$ since $I_p \sim 2.8\text{keV}$ in this case. For these values of κ , Figure 6(a) displays the temporal dependence of $|\mathcal{M}_{fi}(\mathbf{R} = 0)|^2$ for the ejection of both $2p$ (solid line) and $3p$ (dotted line) electrons by an interaction with the incident expanded and coherent $4p$ state.

Most notably, Fig. 6(a) clearly indicates that the cross-section for the collisional ejection of a $2p$ electron by the ponderomotively-driven and expanding $4p$ orbital is always at least two orders of magnitude *greater* than for the ejection of a $3p$ electron. This additional radial or n -state selectivity is a direct consequence of the shape of the $3p$ radial wavefunction relative to that of the $2p$ state; namely, the bipolar nature of the $3p$ orbital suppresses the matrix element associated with the collisional interaction. In other words, the ejection of electrons from states with the fundamental single-peaked radial wavefunction is strongly preferred in this selective coherent interaction. As shown by the plot in Fig. 6(b), this is in fact true for all values of κ and, hence, incident collision energies for the $4p$ state. Moreover, the ratio of $2p$ to $3p$ collisional cross-sections for this coherent interaction is also relatively insensitive to the excitation wavelength for $\kappa > 5\text{\AA}^{-1}$. This result is clearly consistent with the observed Xe(L) emission under intense laser excitation, because virtually no $3p$ vacancy generation would be expected even for *multiple* $2p$ vacancy production; an outcome in agreement with the charge labeling in Fig. 1 for *both* the IR and UV excitation wavelengths. Furthermore, the calculated ratio between the $2p$ and $3p$ collision cross-section represents at least a three orders of magnitude *reversal* over the cross-section ratio evaluated from a plane-wave analysis (Fig. 2) [32].

Figure 6(a) also reveals a *strong* pump-laser wavelength dependence to the selective collisional ionization process; namely, that the coherent orbital-orbital collision is much more probable for

shorter pump-laser wavelengths (i.e. short radiation periods). Specifically, since $\tau \approx 0.04\text{fs}$ for the $4p$ Xe state with an initial bound-state radius a of $\sim 0.7\text{\AA}$, the value of $|M_{fi}(\mathbf{R} = 0)|^2$ for the ejection of a $2p$ electron is ~ 350 times *greater* under 248nm UV laser excitation (collision at $t/\tau = 19$) than for the 800nm pump-laser wavelength (collision at $t/\tau = 63$). The intrinsic quantum mechanical spreading of the photoionized $4p$ state causes a similar reduction in the cross-section for $3p$ impact ionization as the excitation wavelength increases. The inclusion of collisional dephasing within the incident photoionized state $\langle \mathbf{r}_2; t | \psi \rangle$, which destroys the selectivity of the inner-shell ejection process, further magnifies this adverse dependence on the radiation period. For an estimated average electron-electron scattering rate of the order of 1fs^{-1} (Section III.B), we expect a ratio in the selective collisional cross-sections of $\sim 10^3$ favoring the use of 248nm UV over 800nm IR laser excitation. This cross-section ratio is in good agreement with the experimental observation of a strong pump-laser wavelength dependence in the Xe L-shell emission [24,25] which indicates that the shorter-period UV radiation is ~ 3000 times more effective at generating $2p$ vacancies in 5-20 atom Xe cluster targets than equivalent terawatt IR (800nm) radiation. An exact calculation of all collisional dephasing rates in expanding photoionized states $\langle \mathbf{r}_2; t | \psi \rangle$ and a full evaluation of the matrix element M_{fi} integrated over all values of \mathbf{R} in a more rigorous analysis, both of which are beyond the scope of this paper, may yield a closer agreement with the experimental results. Nevertheless, the approximate treatment unambiguously shows that the wavelength dependence is strong and that the use of sufficiently long pump-laser wavelengths will eliminate the selectivity of the interaction.

It is interesting to note that since the $3p$ cross-section is at least one order of magnitude less than the $2p$ cross-section for timescales $t/\tau < 5$, it may be possible to circumvent the strong pump-laser wavelength dependence of L-shell emission by ensuring that the time between the photoionization by ATI and the collisional ejection is much less than the period of the driving radiation. This immediately implies that the ionized state $\langle \mathbf{r}_2; t | \psi \rangle$ must interact within the first quarter of the laser radiation period with an atom/ion that is remote from its atom of origin as could be the case in a solid target material or in large (> 100) atom clusters. However, for the selective mechanism to be effective, the laser-driven state $\langle \mathbf{r}_2; t | \psi \rangle$ cannot be significantly dephased by collisions with other atoms/ions in the target material prior to reaching the incident kinetic energy necessary for the collisional ejection of a particular inner-shell electron. Such a condition is expected to be difficult to achieve unless the ponderomotive potential is sufficiently strong to allow acceleration to the required kinetic energy over inter-atomic distances. Nonetheless, precisely this type of interaction has already been observed in the generation of $2\sigma_g$ vacancies in N_2 [50] and in the more recent detection of strong Ba(L) emission from solid BaF_2 targets [51] under excitation with intense sub-picosecond 248nm radiation.

IV. Inner-Shell Population Inversion

The selective collisional ionization mechanism described above is clearly well suited to the efficient generation of inner-shell vacancies and, hence, the population inversion required for the development of coherent kilovolt x-ray radiation sources. In fact, given the quantum state degeneracies of the $2p$ and $3d$ levels, the experimental observation (Fig. 1) of anomalously strong Xe(L) emission due to $2p$ vacancies from both $\text{Xe}^{27+}(2p^53d^{10})$ and $\text{Xe}^{28+}(2p^53d^9)$ is already *direct* evidence for the efficient generation of inner-shell-inverted ionic species in laser-driven plasmas. Whether or not population inversion can be produced is dependent upon the relative rates of generation of the upper and lower states of the considered transition; for example, the electron configurations $2p^53d^{10}$ and $2p^63d^9$ respectively for L-shell emission from Xe^{27+} . Nonetheless, the above analysis of the experimental results (Fig. 1) indicates that a UV laser-pumped Xe L-shell system has great potential as a *coherent* 3\AA ($\approx 4\text{keV}$) x-ray radiation source. Furthermore, the strong relativistic self-focusing effects observed in Xe cluster targets under 248nm pump-laser irradiation [52] may produce an optimal guided-channel geometry [29,40] extending over several Rayleigh ranges for both the optical pumping and the x-ray emission.

The extension of this collisional process to the generation of more energetic x-ray radiation would require the use of either higher Z elements for the equivalent L-shell emission or K-shell emission through the $1s^22p^5 \leftarrow 1s2p^6$ transition in elements with $Z > 30$. While the former is complicated by the engineering of suitable metal cluster or other composite and compound (e.g. UF_6) targets, the latter possibility appears to offer more practical flexibility. A similar selective collisional ionization process for K-shell emission would require the photoionization by ATI and subsequent ponderomotive acceleration of the $3s$ state to collisionally eject an electron from the $1s$ state within one radiative period. Unfortunately, for Xe(K) emission, a very high laser irradiance of $\sim 3 \times 10^{20} \text{W/cm}^2$ to ionize the $3s$ state would be required. A attractive alternative target atomic species, which could produce very useful $\sim 1\text{\AA}$ K-shell radiation [13], is Kr for which ATI of the $3s$ state requires a laser irradiance of $\sim 2 \times 10^{19} \text{W/cm}^2$ - a value associated with the channeling of 248nm radiation in underdense plasmas [29].

Figures 7(a) and (b) show, respectively, the results of evaluating the modulus-square of the explicit l -state selective matrix element, i.e. $|M_{fl}(\mathbf{R} = 0)|^2$, for the collisional ejection of bound $1s$ and $2s$ electrons in Kr by ponderomotively-driven $3s$ electrons as a function of κ and the normalized time t/τ for the expanding photoionized orbital. Again, the collision cross-section

decreases in time, due to the spreading ionized $3s$ wavefunction, and with increasing collision energy, i.e. κ . However, in this case, it is not immediately apparent whether it is more probable to collisionally eject a $1s$ or a $2s$ electron in the coherent interaction. The answer to this question lies in the details of the collision dynamics.

At a laser irradianc of $\sim 2 \times 10^{19} \text{ W/cm}^2$, the relativistic kinetic analysis of Ref. 25 indicates that an electron photoionized by ATI will return to a small (~ 10 atom) Kr cluster with an energy of $\sim 20 \text{ keV}$ after approximately one radiation period. Since the ionization potentials of the $1s$ and $2s$ states are $\sim 17 \text{ keV}$ and $\sim 3.2 \text{ keV}$, the most probable average values for κ are 14 and 33 for the ejected $1s$ and $2s$ electrons respectively. For these values of κ , the temporal dependence of $|M_{\mu}(\mathbf{R} = 0)|^2$ for the ejection of both $1s$ (solid line) and $2s$ (dotted line) electrons by an interaction with the ponderomotively-driven coherent $3s$ state is shown in Figure 8. It is immediately apparent that again the impact ionization of the inner single-lobed bound $1s$ state is favored over the ejection of an electron from the $2s$ state, but only by roughly one order of magnitude. The fact that the magnitudes of the two matrix elements are much closer for this s -state interaction than equivalent elements in the previous p -state collisions is due to the form of the Laguerre polynomials for $l = 0$; namely, that the relative width of the first radial lobe of the s -states is less than that of the p -states. Consequently, the overlap of the expanding photoionized $3s$ wavefunction with the relatively large second lobe of the $2s$ state dominates the matrix element despite the $1/r$ variation of the Coulomb potential. Nevertheless, the analysis suggests that it may be possible to generate efficiently through laser excitation Kr ions exhibiting inversion between the $2p$ and $1s$ states without significant influence from a parasitic $2s \leftarrow 2p$ transition.

The efficiency with which such an inner-shell-inverted ionic species are produced is, however, again a strong function of the pump-laser wavelength due to the spreading of the ponderomotively-driven $3s$ state over one radiation period. In this case, the smaller initial $\sim 0.5 \text{ \AA}$ radius of the Kr $3s$ orbital [49] ensures that the photoionized wavefunction spreads at almost twice the rate of a Xe $4p$ orbital ionized by ATI. As a result, for Kr K-shell emission, the ratio of the $1s$ collisional cross-sections at pump-laser wavelengths of 248 nm ($t/\tau \approx 40$) and 800 nm ($t/\tau \approx 130$) only favors the UV laser radiation by a factor of ~ 30 - an order of magnitude less than for the $2p$ cross-section in the equivalent Xe L-shell process (Fig. 6(a)). However, the initial internal dephasing rate due to electron-electron scattering in the photoionized 2-electron Kr $3s$ orbital is very close to that of the 6-electron Xe $4p$ orbital ionized by ATI, since the initial electron densities are nearly identical. Consequently, after inclusion of collisional dephasing, the ratio between the

two cross-sections is again expected to favor the shorter 248nm pump-laser wavelength by a factor of at least 100.

A comparison of the magnitudes of $|M_{fi}(\mathbf{R} = 0)|^2$ evaluated for the generation of Xe(L) and Kr(K) emission by inner-shell vacancy production (e.g. Figs. 6(a) and 8) also suggests that the cross-section for $1s$ ejection may be substantially larger than that for the impact ionization of a $2p$ electron for this coherent interaction. This is predominantly due to the r^l radial dependence of the bound atomic wavefunctions which suppresses the dominant contribution to the matrix element of the Coulomb interaction near the origin of the coordinate system (Fig. 3) when $l \neq 0$. However, this trend may be reversed in a full evaluation of the matrix element M_{fi} , because the larger $2p$ bound-state target wavefunction will contribute more to the interaction for $\mathbf{R} \neq 0$ than the smaller $1s$ atomic orbital. Moreover, the $2p$ ejection cross-section will be enhanced by an order of magnitude over the $1s$ ejection cross-section since there are three more m -states (and electrons) in a full p -orbital than in a s -state. In addition, it should be noted that the relativistic kinematic analysis of Ref. 25 indicates that the Lorentz force in the ponderomotive potential will force the driven photoionized wavefunction $\langle \mathbf{r}_2; t | \psi \rangle$ to avoid a collision with the target atom(s) in gas or atomic cluster materials at sufficiently high laser irradiances. Thus, since this effect is much less severe for shorter radiation periods (due to the reduced impulse), the future development of a *coherent* $\sim 1\text{\AA}$ x-ray radiation source based on a gaseous target material strongly favors the use of high-power short wavelength (UV) rather than long wavelength (IR) pump lasers. In fact, the combined deleterious effects of the Lorentz force and the dephasing of $\langle \mathbf{r}_2; t | \psi \rangle$ by electron-electron scattering may be the major limiting factors for the efficient generation of the inner-shell population inversion required for an atom-based coherent hard x-ray radiation source.

V. Conclusions

The selective laser-driven collisional ionization mechanism outlined in this paper provides an explanation for the observation of spectrally anomalous and unexpectedly strong L-shell emission from atomic Xe clusters under intense irradiation (10^{18} - 10^{19}W/cm^2) by sub-picosecond UV TW laser pulses at 248nm (Fig. 1). In particular, it elucidates the physics behind the preferential generation of Xe $2p$ vacancies in collisions with ponderomotively-driven $4p$ electrons that are photoionized by the strong ATI expected in the observed stable channeled propagation of the UV laser radiation under relativistic self-focusing conditions [29,40,52]. Such a specific coupling of the incident laser energy into target atoms, at a rate that may exceed 1W/atom [22,23,53], could lead to the inner-shell population inversion required for the development of future coherent hard

x-ray sources. Indeed, the experimental observation of $\sim 5\text{keV}$ L-shell emission from both $\text{Xe}^{27+}(2p^53d^{10})$ and $\text{Xe}^{28+}(2p^53d^9)$ already provides direct evidence that laser-driven inner-shell inverted ions can be efficiently generated. We note that the extension of this mechanism to uranium would generate L-shell emission in the $15\text{-}17\text{keV}$ range. Analysis of a similar selective collisional ejection process to produce $1s$ vacancies in Kr suggests that the development of an efficient K-shell radiation source may also be possible.

The analysis of this novel laser-driven collisional ionization mechanism also indicates an extraordinarily strong laser wavelength dependence for gas-phase-like targets (e.g. small atomic clusters and dilute gases) where the photoionized electrons may return to interact with the atom/cluster of origin after approximately one radiative period [25]. Both the intrinsic quantum mechanical spreading of the photoionized wavefunction and its dephasing by electron-electron scattering ensure that the efficiency of the selective collisional ejection process is reduced by a factor of $\sim 10^3$ as the pump-laser wavelength is increased by only a factor of ~ 3 from the UV (248nm) to the IR (800nm). In fact, for sufficiently long laser radiative periods, the dephasing causes the progression to the plane-wave scattering regime for which the relative cross-sections indicate that the generation of inner-shell population inversion for kilovolt x-ray emission in high Z atoms is ruled out. The analysis also shows that this impossibility is robust and cannot be overcome by the use of higher laser powers, such as petawatt Ti:sapphire- or Nd-based IR laser systems whose long radiation wavelength would essentially avoid the special features arising from the coherent phase dependence of the interaction. Form this point of view, the recent demonstration of an efficient third harmonic generation scheme for high power IR lasers appears very attractive [54]. The strong pump-laser wavelength dependence could be circumvented, while retaining the l -state and significant radial (n -state) selectivity of the collisional ionization mechanism, by using condensed-phase targets (e.g. solid targets and large atomic clusters) provided that the ionization collisions occurred within a quarter of radiation period, i.e. the photoionized electron interacted with an atom other than its atom of origin. However, the selectivity of ionization process is likely to be rapidly impaired by scattering with ions and other electrons in the laser-generated plasma as the photoionized wavefunction is accelerated to the incident collisional energy necessary for inner-shell impact ionization.

A more elaborate and sophisticated calculation of the matrix element M_{fi} for the kinematics of the selective collisional ionization mechanism should provide further insight into the conditions required for the optimally efficient generation of inner-shell vacancies. In particular, explicit evaluation of M_{fi} for $\mathbf{R} \neq 0$ should allow the limits of the strength of the l -state selectivity of the mechanism to be determined. A comparison of the cross-section of this selective mechanism with

respect to the plane-wave case is also required to quantify experimentally observed enhancement of the former. In addition, a more detailed evaluation of the effect of quantum mechanical spreading on the collisional dephasing dynamics internal to the photoionized wavefunction is necessary. Nevertheless, it is clear that the selective collisional ionization mechanism provides a new mode of energy coupling to atoms which could result in the efficient and controlled generation of inner-shell population inversion required of potential *coherent* kilovolt x-ray sources. Furthermore, the evident consistency between the theoretical analysis and the experimental data strongly suggests that the pump-laser wavelength is a substantially more important parameter than the laser power or intensity.

VI. Acknowledgments

The authors would like to thank Drs. T. Imbo and W. Pötz for useful discussions. The authors respectfully acknowledge the expert technical assistance of J. Wright and P. Noel during the experimental investigations and M. Mehendale in the preparation of the manuscript. Support for this research was provided under grants and contracts with the National Science Foundation (BIR 9513266), SDI/NRL (N00014-93-K-2004), Army Research Office (DAAG55-97-1-0310), the Department of Energy at the Sandia National Laboratories and the United States Department of Energy (DE-AC04-94AL85000 and BB9131), the Japanese Ministry of Education, Science, Sport, and culture (#08405009 and #08750046) and the Murata Science Foundation. Sandia is a multi-program laboratory operated by Sandia Corporation, a Lockheed Martin company, for the the United States Department of Energy under contract DE-AC04-94AL85000.

FIGURE CAPTIONS

Figure 1

The kilovolt Xe L-shell ($2p \leftarrow 3d$) x-ray spectrum emitted by 5-20 atom Xe clusters pumped by TW ultraviolet (248nm) and infrared (800nm) sub-picosecond laser pulses. The charge-state designations are the result of an analysis based on the work of Cowan [30], which also indicates that the feature at $2.6-2.65\text{\AA}$ is attributable to the generation of multiple $2p$ vacancies.

Figure 2

The plane-wave collision cross-sections σ for the ejection of $2p$, $3s$, $3p$, and $3d$ electrons with ionization potentials of 8keV, 3.3keV, 2.8keV, and 1.8keV respectively as a function of the energy of the incident colliding electron (after McGuire [32]). For convenience, the cross-sections are normalized to the maximum cross-section for the ejection of a $2p$ electron at a incident collision energy of $\sim 30\text{keV}$. The shaded region indicates the 10-20keV energy of photoionized electrons returning to interact with their cluster of origin for laser irradiances of $10^{18}-10^{19}\text{W/cm}^2$.

Figure 3

The interaction geometry for the ejection of an electron from a bound state $\langle \mathbf{r}_1 | \phi_j \rangle$ via a Coulombic collision with a ponderomotively-driven photoionized electronic state $\langle \mathbf{r}_2, t | \psi \rangle$ displaced by \mathbf{R} from the target atom (or ion).

Figure 4

Comparison of the exact (solid curves) and hydrogenic (dashed curves) normalized radial wavefunctions $rR(r)$ for the $2p$, $3p$, and $4p$ orbital of Xe. The hydrogenic wavefunctions are obtained using effective nuclear charges of 50, 42, and 40 respectively.

Figure 5

The calculated value of $|M_{fi}(\mathbf{R} = 0)|^2$ as a function of the normalized expansion time t/τ and $\kappa = k_i \cos\beta$ for the coherent collisional ejection of (a) $2p$ and (b) $3p$ electrons in Xe by an expanding photoionized $4p$ state.

Figure 6

- a) The value of $|M_{fi}(R=0)|^2$ as a function of the normalized expansion time t/τ for the collisional ejection of a $2p$ electron with $\kappa = 21\text{\AA}^{-1}$ (solid line) and a $3p$ electron with $\kappa = 28\text{\AA}^{-1}$ (dashed line) in Xe by a photoionized $4p$ state. The vertical lines indicate the periods for 248nm UV and 800nm IR radiation.
- b) The ratio of $|M_{fi}(R=0)|^2$ for $2p$ versus $3p$ inner-shell electron ejection as a function of $\kappa = k_1 \cos\beta$ for a collision after one 0.8fs 248nm radiation period (solid line) and one 2.7fs 800nm radiation period (dashed line).

Figure 7

The calculated value of $|M_{fi}(R=0)|^2$ as a function of the normalized expansion time t/τ and $\kappa = k_1 \cos\beta$ for the coherent collisional ejection of (a) $1s$ and (b) $2s$ electrons in Kr by an expanding photoionized $3s$ state.

Figure 8

The value of $|M_{fi}(R=0)|^2$ as a function of the normalized expansion time t/τ for the collisional ejection of a $1s$ electron with $\kappa = 14\text{\AA}^{-1}$ (solid line) and a $2s$ electron with $\kappa = 33\text{\AA}^{-1}$ (dashed line) in Kr by a photoionized $3s$ state. The vertical lines indicate the periods for 248nm UV and 800nm IR radiation.

RERFERENCE

- [1] McPherson A., Gibson G., Jara H., Johann U., Luk T.S., McKintyre I.A., Boyer K., and Rhodes C.K. 1987 Studies of multiphoton production of vacuum-ultraviolet radiation in rare gases *J. Opt. Soc. Am. B* **4** 595
- [2] Zhou J., Peatross J., Murnane M., Kapteyn H., and Christov I. 1996 Enhanced high-harmonic generation using 25 fs laser pulses *Phys. Rev. Lett.* **76**, 752; Chang Z., Rundquist A., Wang H., Murnane M., and H. Kapteyn 1997 Generation of coherent soft x-rays at 2.7nm using high harmonics *Phys. Rev. Lett.* **79** 2967
- [3] Spielmann Ch., Burnett N.H., Sartania S., Koppitsch R., Schnürer M., Kan C., Lenzner M., Wobrauschek P., and Krausz F. 1997 Generation of coherent x-rays in the water window using 5-femtosecond laser pulses *Science* **278** 661; Schnürer M., Spielmann Ch., Wobrauschek P., Streli C., Burnett N.H., Kan C., Ferencz K., Koppitsch R., Cheng Z., Brabec T., and Krausz F. 1999 Coherent 0.5-keV x-ray emission from helium driven by a sub-10-fs laser *Phys. Rev. Lett.* **80** 3236
- [4] Macchietto C.D., Benware B.R., and Rocca J.J. 1999 Generation of millijoule-level soft-x-ray laser pulses at a 4-Hz repetition rate in a highly saturated tabletop capillary discharge amplifier *Opt. Lett.* **24** 1115
- [5] Matthews D. L., Hagelstein P. L., Rosen M. D., Eckart M. J., Ceglio N. M., Hazi A. U., Medscki H., MacGowan B. J., Trebes J. E., Whitten B. L., Cambell E. M., Hatcher C. W., Hawryluk A. M., Kauffman R. L., Pleasance D. L., Rambach G., Scofield J. H., Stone G., and Weaver T. A. 1985 Demonstration of a soft x-ray amplifier *Phys. Rev. Lett.* **54**, 110
- [6] Zhang J., Key M. H., Norreys P. A., Tallents G. J., Behjat A., Danson C., Demir A., Dwivedi L., Holden M., Lewis C. L. S., MacPhee A. G., Neely D., Pert G. J., Ramsden S. A., Rose S. J., Shao Y. F., Thomas O., Walsh F., and You Y. L. 1995 Demonstration of high gain in a recombination XUV laser at 18.2 nm driven by a 20 J, 2 ps glass laser *Phys. Rev. Lett.* **74**, 1335
- [7] Da Silva L. B., London R. A., MacGowan B. J., Mrowka S., Matthews D. L., and Craxton R. S. 1994 Generation of a 45-ps-duration 15.5-nm x-ray laser *Opt. Lett.* **19**, 1532
- [8] Lemoff B. E., Lin G. Y., Gordon III C. L., Barty C. P. J., and Harris S. E. 1995 Demonstration of a 10-Hz femtosecond-pulse-driven XUV laser at 41.8 nm in XE IX *Phys. Rev. Lett.* **74**, 1574
- [9] Kim D., Toth C., and Barty C.P.J. 1999 Population inversion between atomic inner-shell vacancy states by electron-impact ionization and Coster-Kronig decay *Phys. Rev. A* **59** R4129
- [10] Duguay A. and Rentzepis P.M. 1967 Vacuum u.v. and x-ray lasers *Appl. Phys. Lett.* **10** 350

- [11] Moribayashi K., Sasaki A., and Tajima T. 1999 X-ray emission by ultrafast inner-shell ionization from vapors of Na, Mg, and Al *Phys. Rev. A* **59** 2732
- [12] Schoenlein R. W., Leemans W. P., Chin A. H., Volfbeyn P., Glover T. E., Balling P., Zolotorev M., Kim K.-J., Chattopadhyay S., and Shank C. V. 1996 Femtosecond x-ray pulses at 0.4 Å generated by 90° Thomson scattering: A tool for probing the structural dynamics of materials *Science* **274**, 236; Leemans W. P., Schoenlein R. W., Volfbeyn P., Chin A. H., Glover T. E., Balling P., Zolotorev M., Kim K. J., Chattopadhyay S., and Shank C. V. 1996 X-ray based subpicosecond electron bunch characterization using 90-degrees Thomson scattering *Phys. Rev. Lett.* **77**, 4182
- [13] Solem J. C. and Baldwin G. C. 1982 Microholography of living organisms *Science* **218**, 229; Solem J. C. and Chapline G. F. 1984 X-ray biomicroholography *Opt. Eng.* **23**, 3; Haddad W. S., Cullen D., Solem J. C., Boyer K., and Rhodes C. K. 1988 X-ray Fourier-transform holographic microscope *Proceedings of the OSA Topical Meeting - Short Wavelength Coherent Radiation: Generation and Applications*, p.284, North Falmouth, MA (Optical Society of America); Boyer K., Solem J. C., Longworth J. W., Borisov A. B., and Rhodes C. K. 1996 Biomedical three-dimensional holographic microimaging at visible, ultraviolet and x-ray wavelengths *Nature Medicine* **2**, 939
- [14] Tillman C., Persson A., Wahlstrom C. G., Svanberg S., and Herrlin K. 1995 Imaging using hard x-rays from a laser-produced plasma *Appl. Phys. B* **61**, 333; Tillman C., Mercer I., Svanberg S., and Herrlin K. 1996 Elemental biological imaging by differential absorption with a laser-produced x-ray source *J. Opt. Soc. Am. B* **13**, 209; Gratz M., Tillman C., Mercer I., and Svanberg S. 1996 X-ray generation for medical applications from a laser-produced plasma *Appl. Sur. Sci.* **96-8**, 443
- [15] Jiang Z., Ikhlef A., Kieffer J.-C., Ráksi F., and Wilson K. R. 1996 Chemical reaction observed by ultrafast x-ray absorption *Springer Series in Chemical Physics* **62 - Ultrafast Phenomena X**, p.274, eds. P. F. Barabara, J. G. Fujimoto, W. H. Knox, and W. Zinth (Springer-Verlag, Berlin)
- [16] Rose-Petrucci C., Jimenez R., Guo T., Cavalleri A., Siders C.W., Ráksi F., Squier J.A., Walker B.C., Wilson K.R., and Barty C.P.J. 1999 Picosecond milli-angstrom lattice dynamics measured by ultrafast x-ray diffraction *Nature* **398** 310
- [17] Yang J., Washio M., Endo A., and Hori T. 1999 Evaluation of femtosecond x-rays produced by Thomson scattering under linear and nonlinear interactions between a low-emittance electron beam and an intense polarized laser light *Nucl. Inst. Meth. A* **428** 556
- [18] McPherson A., Thompson B. D., Borisov A. B., Boyer K., Rhodes C. K. 1994 Multiphoton-induced x-ray emission at 4-5 keV from Xe atoms with multiple core vacancies *Nature* **370**, 631

- [19] See for example, Protopapas M., Keitel C. H. ,and Knight P. L. 1997 Atomic physics with super-high intensity lasers *Rep. Prog. Phys.* **60**, 389
- [20] Portella M.T., Bigot J.-Y., Schoenlein R.W., Cunningham J.E., and Shanck C.V. 1992 k -space carrier dynamics in GaAs *Appl. Phys. Lett.* **60** 2123
- [21] Becker P.C., Fragnito H.L., Brito Cruz C.H., Fork R.L., Cunningham J.E., Henry J.E., and Shank C.V. 1988 Femtosecond photon echoes from band-to-band transitions in GaAs *Phys. Rev. Lett.* **61** 1647
- [22] Borisov A. B., McPherson A., Boyer K., and Rhodes C. K. 1996 Intensity dependence of the multiphoton-induced Xe(L) spectrum produced by subpicosecond 248 nm excitation of Xe clusters *J. Phys. B: At. Mol. Opt. Phys.* **29**, L43
- [23] Borisov A. B., McPherson A., Boyer K., and Rhodes C. K. 1996 Z- λ imaging of Xe(M) and Xe(L) emissions from channelled propagation of intense femtosecond 248nm pulses in a Xe cluster target *J. Phys. B: At. Mol. Opt. Phys.* **29**, L113
- [24] Kondo K, Borisov A. B., Jordan C., Boyer K., McPherson A., Schroeder W. A., and Rhodes C. K. 1997 Wavelength dependence of multiphoton-induced Xe(M) and Xe(L) emissions from Xe clusters *J. Phys. B: At. Mol. Opt. Phys.* **30**, 2707
- [25] Schroeder W.A., Omenetto F.G., Borisov A.B., Longworth J.W., McPherson A., Jordan C., Boyer K., Kondo K, and Rhodes C. K. 1998 Pump laser wavelength-dependent control of the efficiency of kilovolt x-ray emission from atomic clusters *J. Phys. B: At. Mol. Opt. Phys.* **31**, 5031
- [26] Bouma B., Luk T. S., Boyer K., and Rhodes C. K. 1993 High-brightness subpicosecond terawatt KrF* system driven with a frequency converted self-mode-locked pulse-compressed Ti:Al₂O₃ laser *J. Opt. Soc. Am. B* **10**, 1180
- [27] McPherson A., Luk T. S., Thompson B. D., Borisov A. B., Shiryaev O. B., Chen X., Boyer K., and Rhodes C. K. 1994 Multiphoton induced x-ray emission from Kr clusters on M-shell ($\sim 100\text{\AA}$) and L-shell ($\sim 6\text{\AA}$) transitions *Phys. Rev. Lett.* **72**, 1810
- [28] Boyer K., Thompson B. D., McPherson A., and Rhodes C. K. 1994 Evidence for coherent motions in multiphoton x-ray production from Kr and Xe clusters *J. Phys. B: At. Mol. Opt. Phys.* **27**, 4373
- [29] Borisov A.B., McPherson A., Thompson B.D., Boyer K., and Rhodes C.K. 1995 Ultrahigh power compression for x-ray amplification: multiphoton cluster excitation combined with non-linear channelled propagation *J. Phys. B: At. Mol. Opt. Phys.* **28** 2143
- [30] Cowan R. D. 1982 *The Theory of Atomic Structure and Spectra* (Berkley, CA: University of California Press)
- [31] Powell C. J. 1976 Cross sections for ionization of inner-shell electrons by electrons *Rev. Mod. Phys.* **48**, 33

- [32] McGuire E. J. 1977 Scaled electron cross sections in the Born approximation *Phys. Rev. A* **16**, 73
- [33] Boyer K. and Rhodes C. K. 1985 Atomic inner-shell excitation induced by coherent motion of outer-shell electrons *Phys. Rev. Lett.* **54**, 1490
- [34] Boyer K. and Rhodes C. K. 1994 Superstrong coherent multi-electron intense-field interaction *J. Phys. B: At. Mol. Opt. Phys.* **27**, L633
- [35] See for example, Merzbacher E. 1970 *Quantum Mechanics* 2nd edition (John Wiley & Sons, New York)
- [36] Brabec T., Ivanov M. Y., and Corkum P. B. 1996 Coulomb focusing in intense field atomic processes *Phys. Rev. A* **54**, R2551
- [37] Bethe H. 1930 Zur Theorie des Durchgangs schneller Korpuskularstrahlen durch Materie *Ann. Phys.* **5**, 325
- [38] Briggs J.S. and Taulbjerg K. 1978 *Theory of inelastic atom-atom collisions* in Structure and collisions of ions and atoms Ed. Sellin I.A. Topics in Current Physics no. 5 (Springer-Verlag, New York) 105
- [39] Clark M.W., Schneider D., Dewitt D., McDonald J.W., Bruch R., Safronova U.I., Tolstikhina I.Yu., and Schuch R. 1993 Xe *L* and *M* x-ray emission following Xe⁴⁴⁻⁴⁸⁺ ion impact on Cu surfaces *Phys. Rev. A* **47** 3983
- [40] Borisov A.B., Shi X.M., Karpov V.B., Korobkin V.V., Shiryaev O.B., Solem J.C., McPherson A., Boyer K., and Rhodes C.K. 1994 Stable self-channeling of intense ultraviolet pulses in underdense plasma, producing channels exceeding 100 Rayleigh lengths *J. Opt. Soc. Am. B* **11** 1941
- [41] Borisov A.B., McPherson A., Thompson B.D., Boyer K., and Rhodes C.K. 1996 Multielectron motions induced in clusters and molecules in self-trapped channels *Multiphoton Processes 1996*, Proceedings of the 7th International Conference on Multiphoton Processes, eds. P. Lambropoulos and H. Walther (Inst. Phys. Conf. Ser. No. 154, IOP Publishing, Bristol and Philadelphia 1997) p.1.
- [42] Rose-Petrucci C., Schafer K. J., and Barty C. P. J. 1995 Possible ionization "ignition" in laser driven plasmas *Applications of Laser Plasma Radiation II (SPIE 2532)* eds. M. C. Richardson and G. A. Kyrala (Bellingham: SPIE), p.272; Rose-Petrucci C., Schafer K. J., Wilson K. R., and Barty C. P. J. 1997 Ultrafast electron dynamics and inner shell ionization in laser driven plasmas *Phys. Rev. A* **55**, 1182; Rose-Petrucci C., Schafer K. J., Wilson K. R., and Barty C. P. J. 1997 Simulation of ionization ignition and inner atom shell ionization in ultrafast laser driven clusters *Proc. Application of High Field and Short Wavelength Sources* (Santa Fe, NM).

- [43] Saradrik E. S. and Schappert G. T. 1970 Classical theory of the scattering of intense laser radiation by free electrons *Phys. Rev. D* **1**, 2738
- [44] Volkov D.M. (1935(34?)) Über eine klasse von lösungen der Diracschen gleichung *Z. Phys.* **94** 250
- [45] *See, for example*, Wang H., Backus S., Chang Z., Wagner R., Kim K., Wang X., Umstadter D., Lei T., Murnane M., and Kapteyn 1999 Generation of 10-W average-power, 40-TW peak-power, 24-fs pulses from a Ti:sapphire amplifier system *J. Opt. Soc. Am. B* **16**, 1790; Barty C. P. J., Guo T., Le Blanc C., Raski F., Rose-Petrucci C., Squier J., Wilson K. R., Yakovlev V. V., and Yamakawa K. 1996 Generation of 18-fs, multiterawatt pulses by regenerative pulse shaping and chirped-pulse amplification *Opt. Lett.* **21**, 668; Chambert J. P., C. Le Blanc C., Chériaux G., Curley P., Darpentigny G., Rousseau P., Hamoniaux G., Antonetti A., and Salin F. 1996 Generation of 25-TW, 32-fs pulses at 10 Hz *Opt. Lett.* **21**, 1921; Sullivan A., Bonlie J., Price D. F., and White W. E. 1996 1.1-J, 120-fs laser system based on Nd-glass-pumped Ti:sapphire *Opt. Lett.* **21**, 603; Beaud P. A., Richardson M., and Miesak E. J. 1995 Multi-terawatt femtosecond Cr:LiSAF laser *IEEE J. Quantum Electron.* **QE-31**, 317; Ditzmire T., Nguyen H., and Perry M. D. 1994 Design and performance of a multiterawatt Cr:LiSrAlF₆ laser system *J. Opt. Soc. Am. B* **11**, 580
- [46] *Data in Science and Technology*, Ed. in Chief R. Poerschke, *Semiconductors: Group IV Elements and III-V Compounds*, Ed. O. Madelung (Springer-Verlag, Berlin, 1991)
- [47] Jackson, J. D. 1975 *Classical Electrodynamics* 2nd edition (John Wiley & Sons, New York)
- [48] Kanter E.P., Dunford R.W., Krässig, Southworth S.H. 1999 Double K-vacancy production in molybdenum by x-ray photoionization *Phys. Rev. Lett.* **83**, 508
- [49] Herman F. and Skillman S. 1963 *Atomic Structure Calculations* (Prentice Hall, Englewood Cliffs, NJ)
- [50] Gibson G., Luk T.S., McPherson A., Boyer K., and Rhodes C.K. 1989 Observation of a new inner-orbital molecular transition at 55.8nm in N₂²⁺ produced by multiphoton coupling *Phys. Rev. A* **40** 2378
- [51] Nelson T.R., Borisov A.B., Cameron S., Longworth J.W., Schroeder W.A., Santoro J., VanTassle A.J., and Rhodes C.K. 1999 Hollow atom production by a shell-selective collisional ejection process in clusters and solids: Xe(L) and Ba(L) *18th International Conference on X-ray and Inner-Shell Processes (Chicago, IL)* paper D60
- [52] Borisov A. B., Borovskiy A. V., Shiryaev O. B., Korobkin V. V., Prokhorov A. M., Solem J. C., Luk T. S., Boyer K., and Rhodes C. K. 1992 Relativistic and charge-displacement self-channeling of intense ultrashort laser pulses in plasmas *Phys. Rev. A* **45**, 5830

- [53] Borisov A.B., Longworth J.W.L., Boyer K., and Rhodes C.K.R. 1998 Stable relativistic/charge-displacement channels in ultrahigh power density ($\approx 10^{21} \text{W/cm}^2$) plasmas *Proc. Natl. Acad. Sci.* **95**, 7854
- [54] Raoult F., Boscheron A.C.L., Husson D., Rouyer C., Sauteret C., and Migus A. 1999 Ultrashort intense ultraviolet pulse generation by efficient frequency tripling and adapted phase matching, *Opt. Lett.* **25**, 354

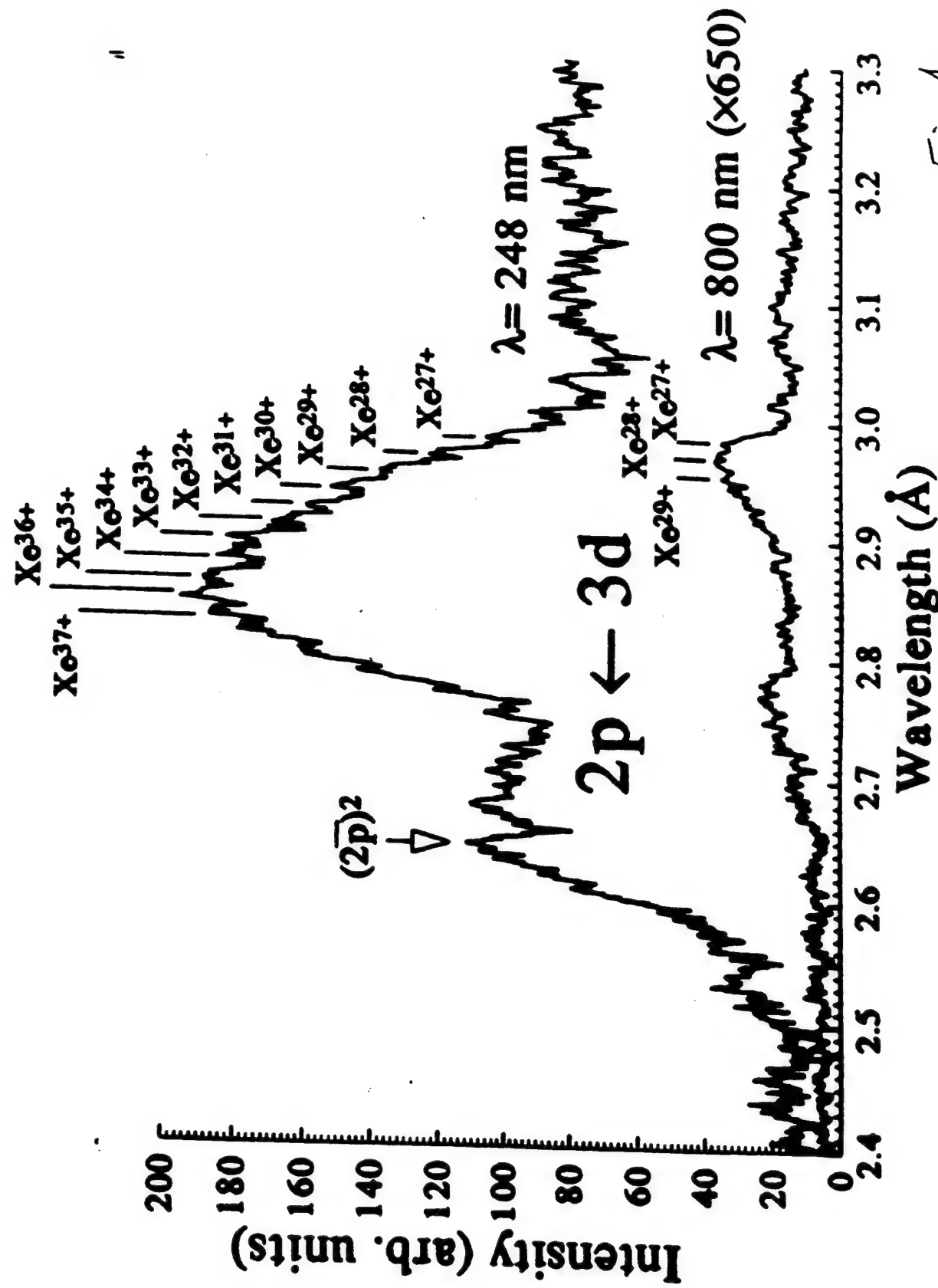
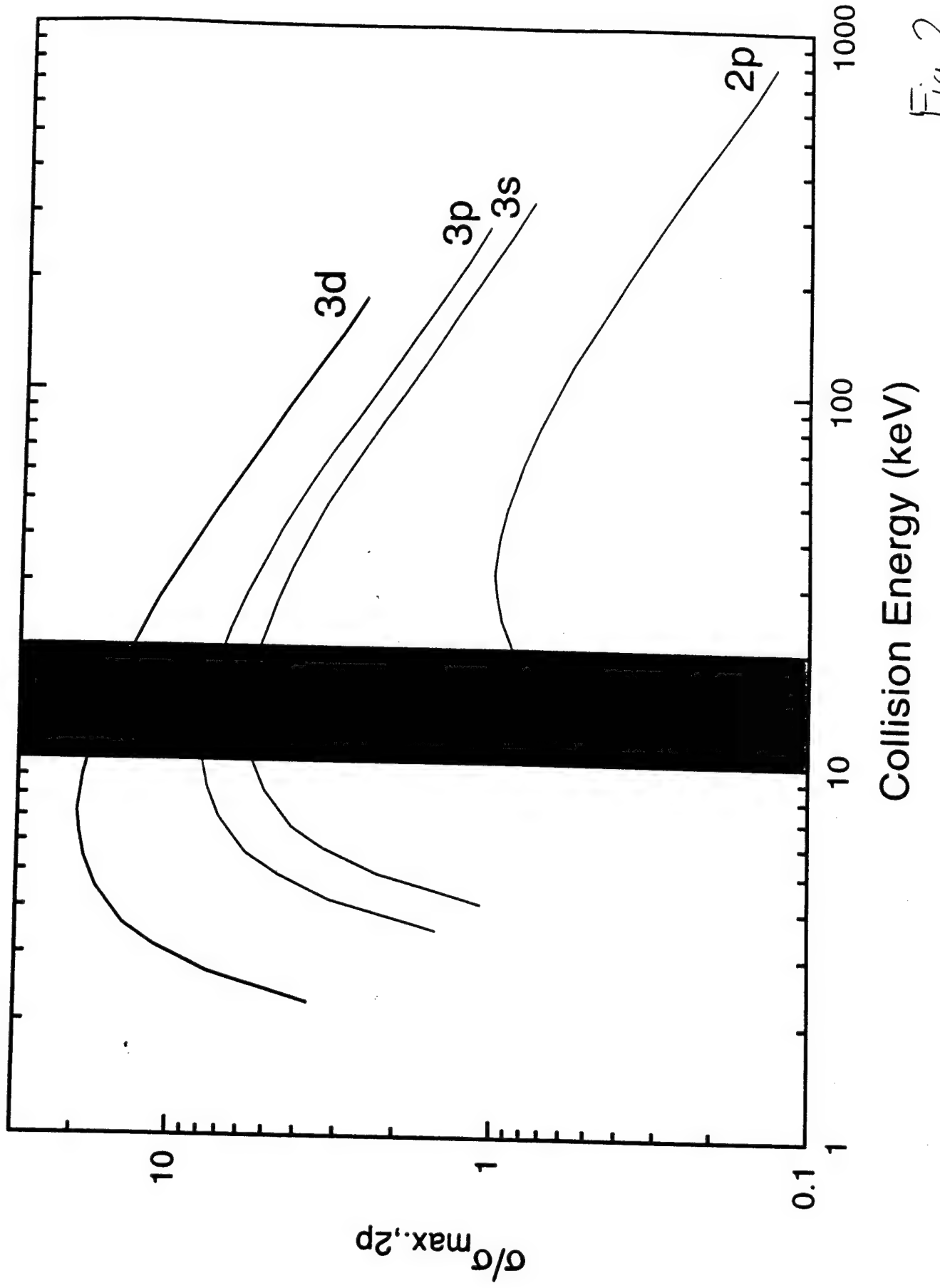


Fig. 1



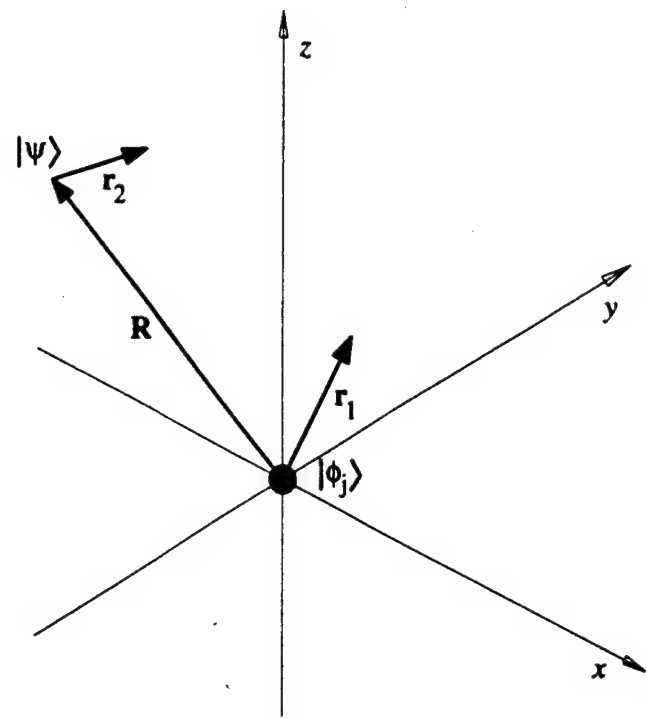


Figure 3

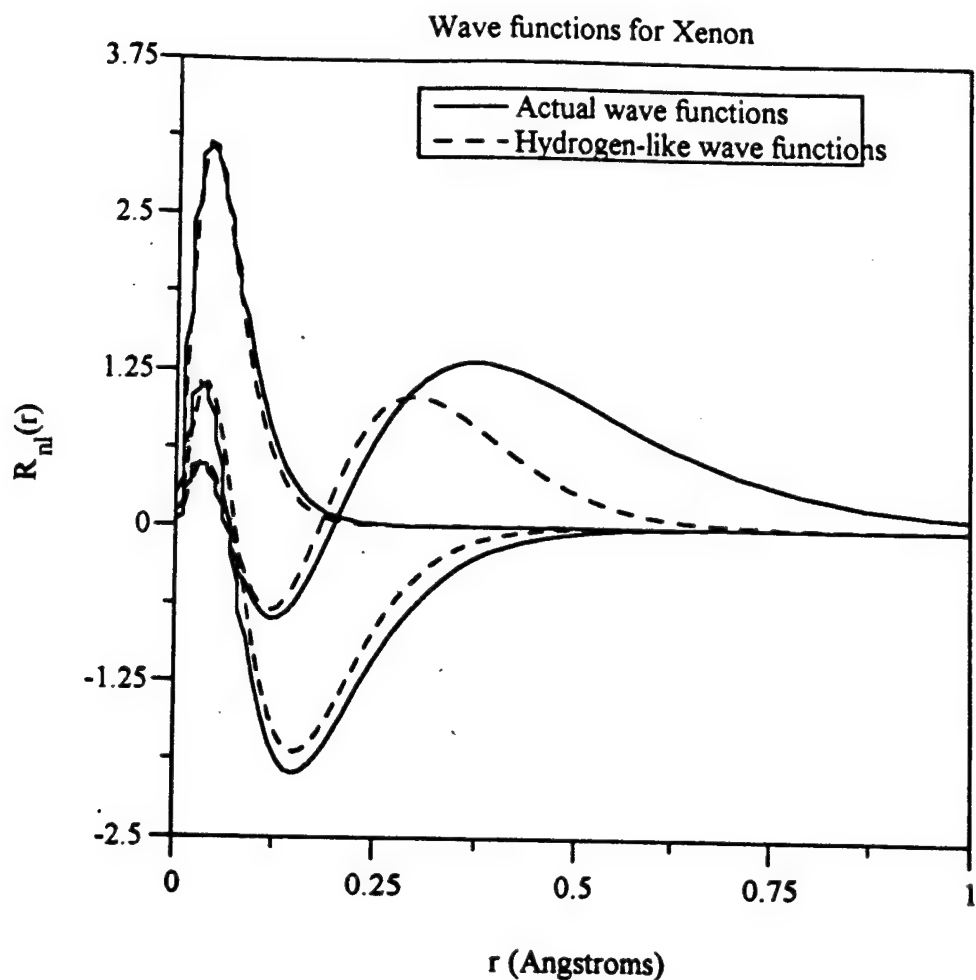


Fig. 4

$|M_{24}(t, \kappa)|^2$

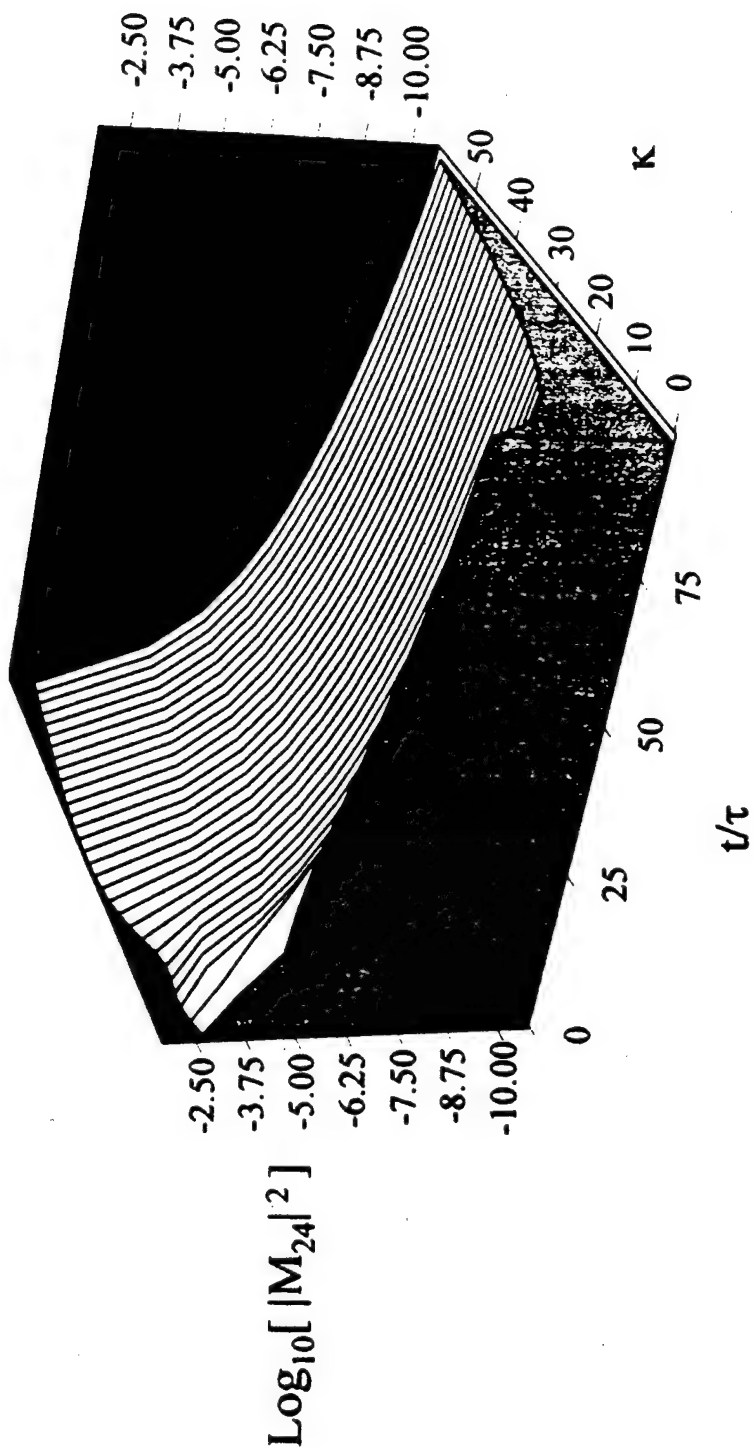


Fig 5(a)

$|M_{34}(t, \kappa)|^2$

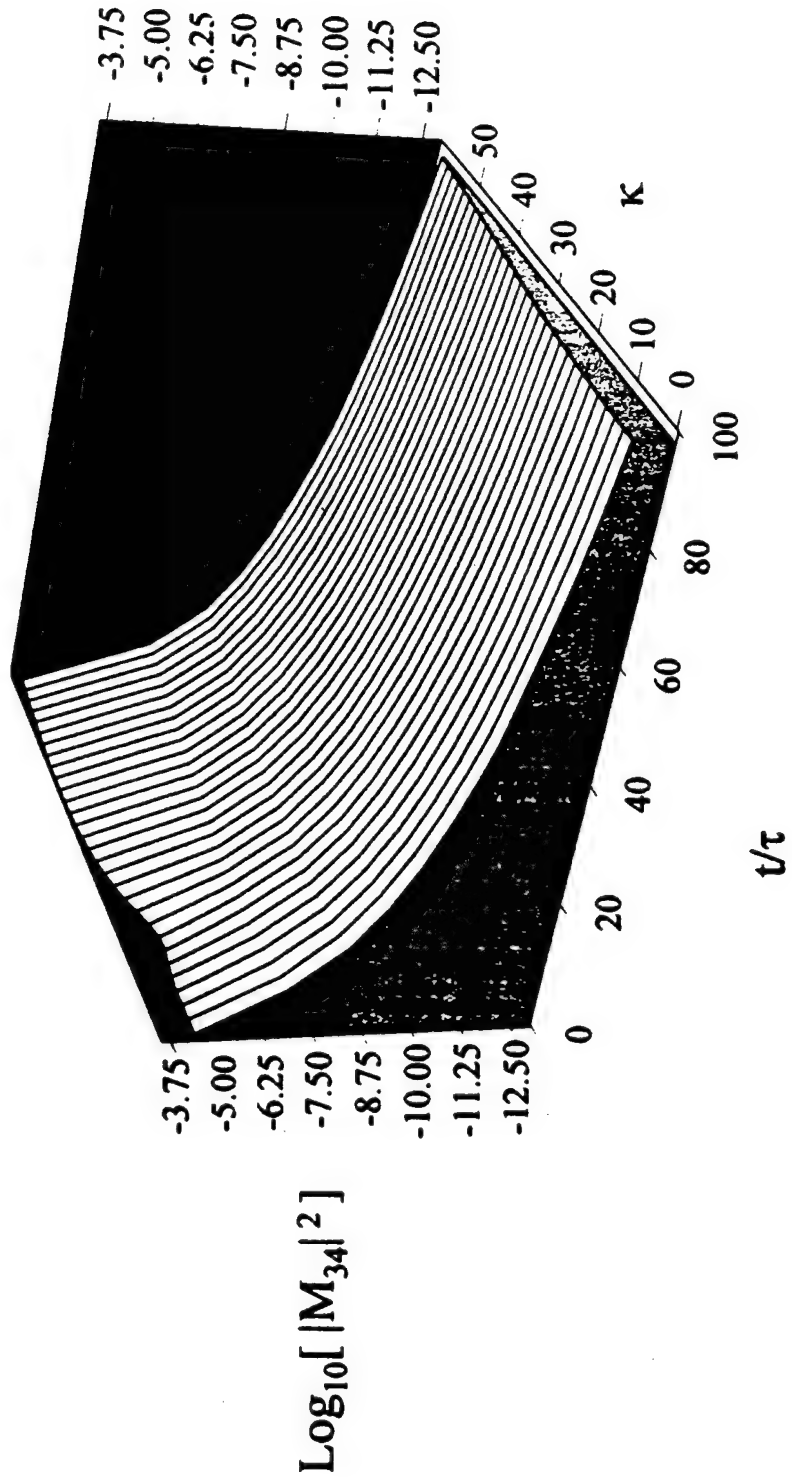


Fig. 5(b)

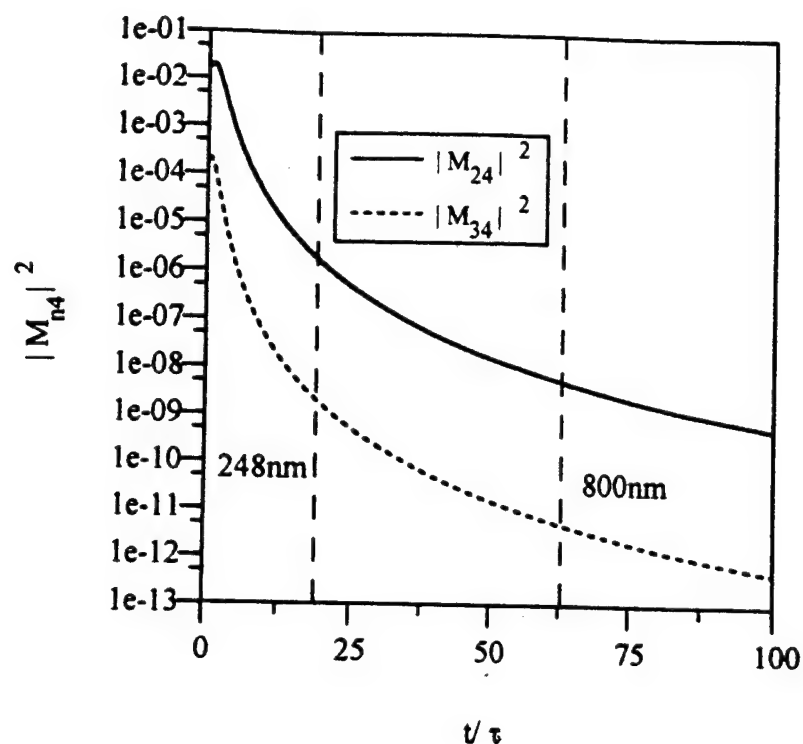
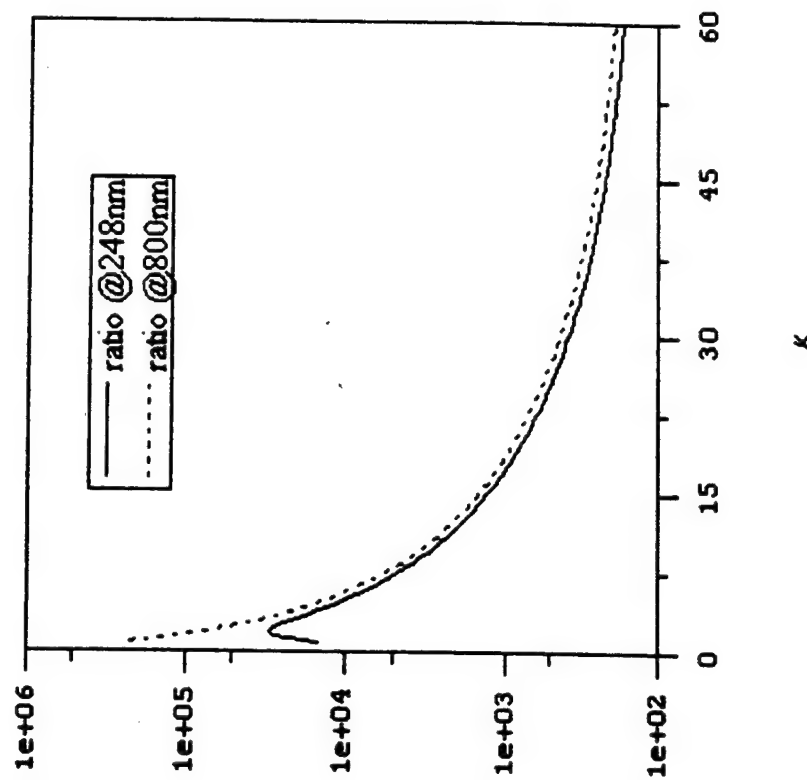


Fig. 6 (a)

Fig. 6 (b)



$|M_{13}(t, \kappa)|^2$

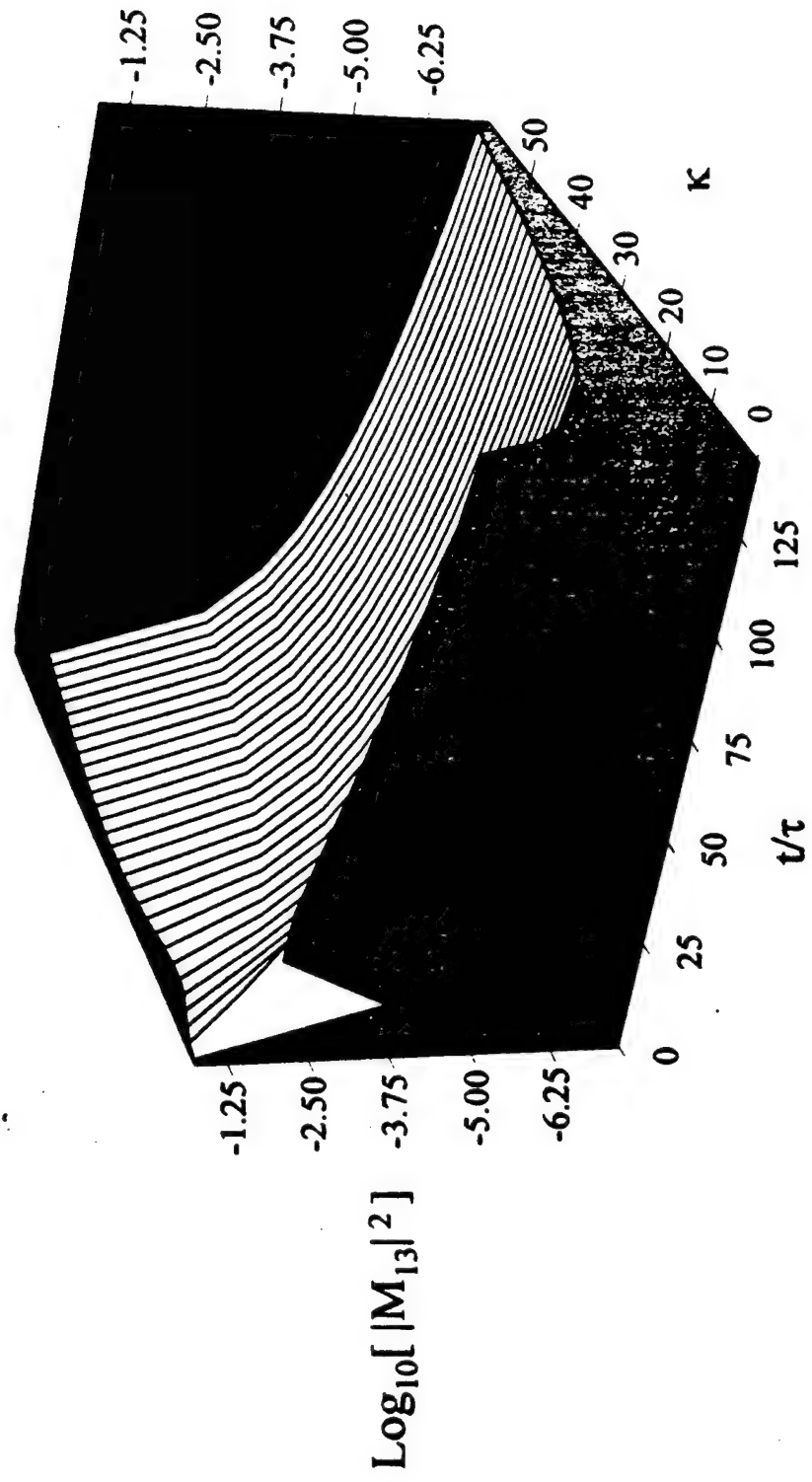
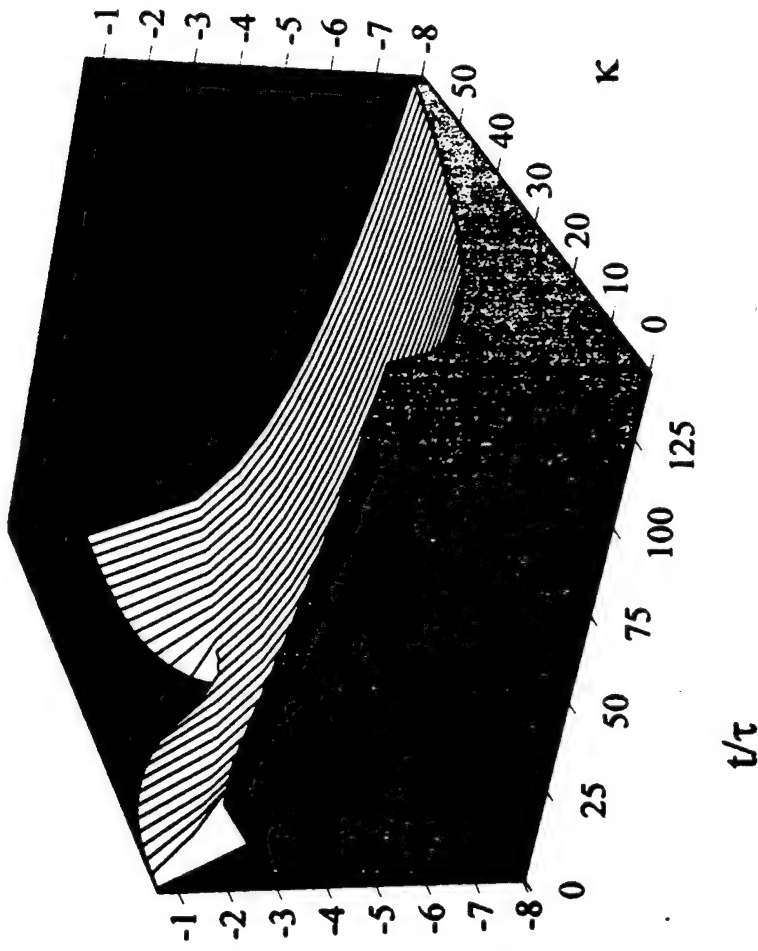


Fig. 7(a)

$|M_{23}(t, \kappa)|^2$



$\text{Log}_{10}[|M_{23}|^2]$

Fig. 7(b)

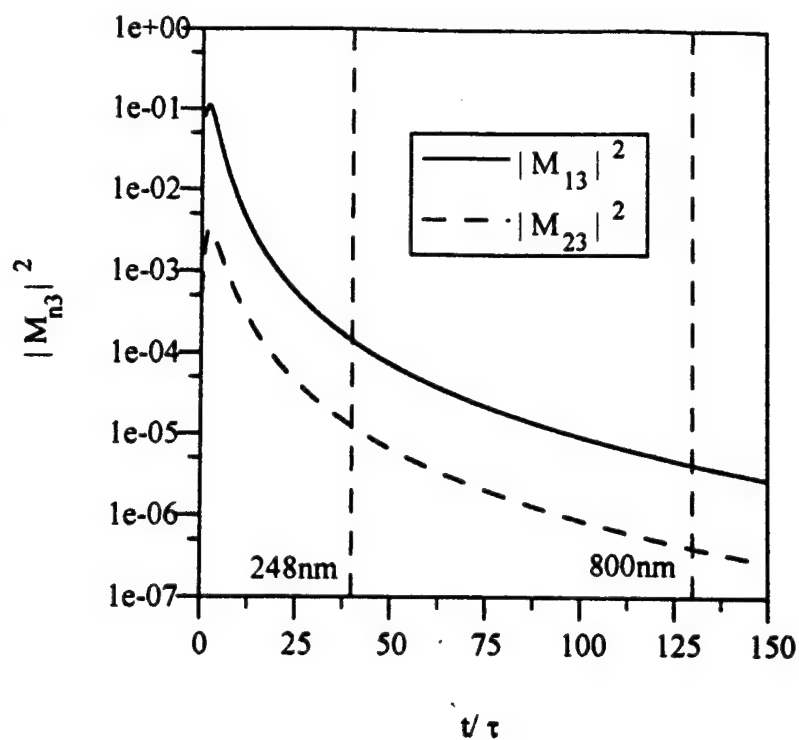


Fig. 8

Appendix 5

L-shell emission from high-Z solid targets by selective inner-shell collisional electron ejection

T.R. Nelson^{1, 2}, A. B. Borisov¹, K. Boyer¹, S. Cameron², J. W. Longworth³, T.S. Luk², A. McPherson⁴, W. A. Schroeder¹, J. Santoro¹, A.J. Van Tassle¹ and C. K. Rhodes¹.

1. *Department of Physics (M/C 273), University of Illinois at Chicago,
845 W. Taylor Street, Chicago, IL 60607-7059, USA*
2. *Sandia National Laboratories, Albuquerque, NM 87185*
3. *Illinois Institute of Technology, Chicago, IL 60616-3793*
4. *Argonne National Laboratory, Argonne IL, 60439-4800*

Abstract

Evidence of highly efficient (1.2% yield) Ba(L) (2.4 – 2.8Å) and Gd(L) (1.7 – 2.1Å) x-ray emission produced from extensively ionized atoms in laser-excited plasmas in BaF₂ and Gd solid targets is presented. An analysis describing a *shell-selective, coherent* collisional ionization mechanism is given in order to explain the observed highly efficient hollow atom production in solids. The L-shell spectra were observed as a result of intense irradiation (peak intensities of 10¹⁸–10¹⁹W/cm²) generated by a sub-picosecond ultraviolet (248nm) terawatt (10¹²W) laser system driven by a hybrid Ti:Sapphire/KrF* laser system. A mica-crystal von Hamos spectrograph equipped with Kodak RAR 2492 x-ray film and appropriate filters was used to collect the spectra emitted by the targets. We discuss the limitations on producing this type of radiation imposed by the laser system used in the experiments and propose a method for surpassing this limitation with little or no additional effort or expense in order to produce L-shell radiation on the order of 15–17 keV from targets as heavy as Uranium.

I. Introduction

Recent studies have reported the efficient production of multi-kilovolt x-ray radiation resulting from inner-shell transitions in rare gas clusters [1-6] as a result of intense irradiation with a subpicosecond ultraviolet (248nm) laser. In particular, the spectra of these emissions were highly anomalous; $2p$ vacancies were being readily produced while the outer subshells remained largely *unperturbed*. This property seems extremely promising for achieving population inversion in these rare gas clusters and could lead to the *coherent amplified emission* of these highly energetic x-rays.

In an attempt to explain the properties of this anomalous x-ray generation, Schroeder et al. [7,8] proposed a new collisional ionization process in which the ponderomotively-driven electrons retained a substantial portion of their phase and symmetry (i.e. coherence) from their original atomic state for a brief period of time after ionization. In reference [8], the authors found it necessary to consider the quantum mechanical wavefunctions of the ionized $4p$ electrons when examining the ionization cross sections for the ejected $2p$ electrons. This is due to the fact that although it has been shown that a conventional collisional ionization process may produce large ionization rates in rare gas clusters for sufficiently high intensities [20], this approach fails to explain both the anomalous nature of the observed spectrum as well as the observed wavelength scaling of the production of the Xe(L) radiation from clusters [6]. In fact, a calculation of the plane wave collisional cross sections for the specific electron orbitals yields a cross section for the ionization of a $3s$ electron that is an order of magnitude *greater* than that for the $2p$ electrons [7,21]. This does not agree with the observations published in [1,6], which show large radiative yields from electronic states with $2p$ vacancies where the $3s$ subshell is largely intact.

In reference [7], the distinctive quantum mechanical treatment of the laser-driven electrons resulted in the collisional ionization dynamics being altered in such a way as to yield a significant n -state and l -state selectivity. In the case of Xe(L) radiation, the assertion was made that it was the previously ionized $4p$ electrons which were acting to generate the $2p$ vacancies. However, the theory outlined in references [7,8] is based upon the supposition that the ponderomotively driven photoionized electron subshell is able to propagate unperturbed by external interactions until it returns to the cluster or ion of origin. In the case of a solid material, this assumption is not valid due to the increased density of atoms in the vicinity of the parent ion.

In this paper, we extend the model of references [7,8] to hollow atom L-shell spectra from 2 solid targets, Ba(L) and Gd(L). The spectra provide evidence of this shell-selective collisional ionization mechanism in solid density targets. Two Gd(L) spectra observed under different laser intensities will serve as the basis to establish an upper bound on the hollow atom x-ray generation based on the peak laser irradiance. A method of extending this limit with the current laser source will be examined.

II. Experimental Setup

The laser system used for the generation of the spectra presented in this paper is a Ti:Sapphire/KrF* hybrid system which is similar to that outlined in reference [9], with the exception that the infrared amplification stage has been replaced by a Ti:Sapphire regenerative amplifier [10]. The system produces pulses with an average energy of 400mJ and pulse duration of 230fs. An f/2 parabolic mirror was used to focus the 248nm laser pulse onto the solid target for a resultant focal intensity of $\sim 10^{19}\text{W/cm}^2$. The spectra were recorded using a mica-crystal von H  mos spectrograph in 3rd order and Kodak RAR 2492 film. A 100  m Kapton (polyimide) filter was used in front of the spectrometer to block lower energy (M-shell) photons. The target materials used were a BaF₂ optical flat (to generate the Ba(L)), and a 100  m thick Gd foil mounted on an Al substrate (to generate the Gd(L)). Since Al(K) radiation is below 2keV, any radiation from the Al substrate that could contaminate the measured spectrum was removed by the Kapton filter.

III. Experimental Data

Figure 1 shows the recorded Ba(L) spectrum. The spectrum was produced under intense irradiation by a pulse energy of 320mJ, corresponding to an average laser power of 1.4TW and a focal irradiance of $\sim 10^{19}\text{W/cm}^2$. As can be seen from the figure, the broad double-peaked structure characteristic of the 3d \rightarrow 2p transition manifold [11] is present, with charge states ranging up to 38+ at the peak of the spectrum, as labeled in Figure 1. By comparison with the Xe(L) spectrum described in reference [1], transitions ranging from (2p⁶3d⁹ \leftarrow 2p⁵3d¹⁰) to (2p⁶ \leftarrow 2p⁵3d) are present in the spectrum. In addition, the Ba spectrum displays the prominent characteristic transitions L_{  1}, L_{  2} and L_{  3} from weakly ionized (0 – 10+) Ba atoms.

To determine the efficiency of the x-ray yield, a calibrated diamond photoconductive semiconductor device (PCD) was used to record the yield from the BaF_2 target. A trace from this detector is shown in Figure 2. The temporal width of the signal is limited by the response of the detector. The risetime of the detector signal is on the order of 100ps, with a $<200\text{ps}$ decay, which is limited by the response of the detector and oscilloscope (Tektronix SCD5000). A filter consisting of $0.1\mu\text{m}$ thick Al on a $7.6\mu\text{m}$ thick Kapton substrate was used to block radiation from Ba(M). The signal shown in Figure 2 corresponds to a total energy of $\sim 4.9\text{mJ}$, assuming a uniform 2π distribution. This translates into a conversion efficiency of $\sim 1.2\%$. The radiative lifetime from this solid target is in stark contradiction to the observations of Ditmire, et al., which showed a long lived emission on the order of $\sim 1\text{ns}$ [5,20] from Kr clusters. The PCD signal supports the conclusion that the Xe(L) emission is prompt; indeed, due to the radiative rate of these charge state configurations, the emission could be as short as the lifetime of the laser pulse. However further experiments with greater temporal resolution (i.e. fast x-ray streak camera measurements) are required to prove this assertion.

Shown in Figure 3(a) and 3(b) are two Gd(L) spectra taken under identical experimental conditions, with the exception of the peak laser intensity. As in the Ba(L) spectrum, Figure 3(a) shows a hollow atom spectrum characterized by the two broad spectral features with charge states ranging up to $40+$, in addition to the lines $L_{\alpha 1}$, $L_{\beta 1}$ and $L_{\beta 2}$ from weakly ionized Gd atoms. The incident laser pulse energy was 350mJ , corresponding to an average laser power of 1.5TW (irradiance of $\sim 10^{19}\text{W/cm}^2$). In Figure 3(b), the hollow atom spectrum is absent, leaving only the characteristic lines. Here, the laser pulse energy was 200mJ , a factor of 0.6 lower. As will be discussed in the next section, these two spectra provide crucial evidence to support the theory presented in this paper and in reference [8].

IV. Solid Target Shell-Selective Collisional Ionization Theory

As indicated in section I, the theory outlined in reference [8] makes the assumption that the ponderomotively driven 4p electron subshell is unperturbed by external collisions until it returns and collides with the parent ion or cluster. The cross-section for this interaction is proportional to the modulus square of the matrix element M_{fi} associated with the interaction mechanism. It was shown in reference [8] that M_{fi} may be expressed as

$$M_{fi}(\mathbf{R} = 0) = \iint d^3\mathbf{r}_1 d^3\mathbf{r}_2 \frac{\phi_j(\mathbf{r}_1)\psi(\mathbf{r}_2, t)}{r_1 r_2 |\mathbf{r}_1 - \mathbf{r}_2|} \exp[-i\mathbf{k}_1 \cdot (\mathbf{r}_1 - \mathbf{r}_2)], \quad (1)$$

where $\phi_j(\mathbf{r}_1)$ is the wavefunction of the electrons to be collisionally ionized, located at coordinate \mathbf{r}_1 around the atom, $\psi(\mathbf{r}_2, t)$ is the wavefunction of the ponderomotively driven electrons, located at coordinate \mathbf{r}_2 about the center of the photoionized electron cloud, \mathbf{k}_1 is the wave vector of the ejected electron after the collision, and \mathbf{R} is the displacement vector between the atom and the electron cloud.

In reference [8], the value of M_{fi} was evaluated and compared for UV (248nm) and IR (800nm) wavelengths, based on the assumption that the collisional ionization occurred after one laser period. This assumption was reasonable because of two points. First, it was demonstrated in reference [7] that it was kinematically possible, for sufficiently high laser intensities, that a previously ionized electron may collide with the cluster of origin with more than enough kinetic energy to ionize a $2p$ electron from Xenon (~ 8 keV). Second, it was estimated that the inter-cluster separation in the target gas jet was large enough that the electrons could be accelerated back into the parent cluster unperturbed by collisions with other clusters.

In a solid density material, the assertion of a collisional ionization occurring in the parent atom is not generally valid because the inter-atomic spacing is much less than the electron excursion. Since the theory governing the ionization of the electron wave packet is unaffected by the target density, it is still reasonable to assert that the $4p$ electrons retain their previous quantum mechanical radial and angular distribution for some period of time after ionization. The primary difference introduced by the density of the solid target is that in this case, the dephasing time could be much shorter, due to the fact that it is possible for the electron wave packet to be dephased by electron-ion collisions in addition to internal electron-electron scattering. However, the crucial point to be made here is that in general, there is *no reason* why the $2p$ vacancies must be created in the *same ion from which the 4p electrons originated*. That is, *this enhanced coupling is not dependent on the specific ion of origin*, only the quantum mechanical nature of the two electron wave-packets. Differences between ions, such as actual ionization state will have a small effect on the specific bound $2p$ wave functions. However, this will only change the magnitude of $|M_{fi}|^2$ by a modest amount; the physics governing the interaction remains unchanged. Compared to the gas cluster case, the coupling should be *greater* in solid targets due

to the fact that the electron orbital will have had less time to dephase due to internal electron-electron collisions. Also, the overlap of the wavefunctions should be greater because the intrinsic spreading of the wave packet will not be as progressed.

To determine if this shell-selective collisional ejection theory may be applied to solid targets, the only issue remaining to be considered is whether the ponderomotively driven electrons will have enough kinetic energy to eject a 2p electron from the target ion. In order to answer this question, two pieces of information are required: the kinematics of the ponderomotively driven electrons (i.e. the kinetic energy as a function of position or time) and the approximate distance between ions. The first point listed above has been calculated in reference [7]. Specifically, the authors used a classical relativistic model to trace out both the position and kinetic energy of the ponderomotively driven electrons as a function of time. Figure 4 shows these curves as a function of the 248nm normalized laser period ct/λ . The calculations in Reference [7] were performed for Xe clusters. However, the numbers are sufficiently similar to those of Ba to be applicable; the ionization potentials differ only by ~5% and the Xe cluster radius r_c for the calculations was 5.3Å, while the lattice spacing in BaF₂ is ~6Å. For simplicity, all calculations performed here will be done for Xe, although qualitatively there will be little difference in the results for Ba and Gd.

To address the second point, one finds that measuring the distances between ions in the solid target of the expanding plasma, may be extremely complicated [12]. In order to quantify this parameter, detailed knowledge of the plasma density generated by the laser is required. In addition, due to the high density of neighboring ions near the ion of origin for the 4p electrons, a rigorous Monte-Carlo simulation must be done to approximate the average frequency of collisions. While these details are necessary in order to precisely estimate the magnitude of $|M_{fi}|^2$ for each solid target, they are not required to ascertain whether the theory may be applied. Continuing with the above comparison to Xe clusters, we approximate the distance between ions in the plasma as being on the order of a few times the spacing in Xe clusters.

The accuracy of this approximation can be determined by establishing realistic upper and lower limits for the ion separation in the laser-driven plasma. Clearly, a reasonable upper limit for the interaction distance is that of the gaseous target, which would have an inter-cluster spacing of ~100Å [7]. It has already been shown in reference [8] that the theory readily applies to this case. For a lower limit, a first approximation would be the actual lattice spacing of the

unperturbed solid. A typical number for this spacing is in the range of 5Å. As can be seen from Figures 4(a) and (b), an electron will reach a displacement of $1r/r_c$ (5.3Å) after ~ 0.03 laser periods, and at that point, will *not* have the required kinetic energy to ionize a 2p electron (8keV). However, from examining Figure 4, it is seen that the average atom separation need only increase by a *factor of two* ($r/r_c = 2$ in the figure) to allow the electrons sufficient time to accelerate to energies large enough to ionize a 2p electron. Therefore, using an ionic spacing on the order of 10-20Å as an extremely conservative lower bound is not only reasonable, but sufficient to demonstrate that the theory may be applied to the case of solid targets. This lower bound also gives an estimate of the delay between arrival of the laser pulse and emission of the L-shell radiation, as well as a time scale for the plasma formation.

In addition, the argument may be made that although there is a high density of atoms near the parent ion, the probability of the ponderomotively driven electrons interacting with a neighboring ion is less than unity. Therefore it is entirely possible that the electrons might not interact with the nearest neighbor ion, but the next-nearest neighbor. Under this condition of a 10 – 20Å separation in the plasma, clearly the electrons would have sufficient kinetic energy to eject the 2p electrons at the time of collision.

At this point, a qualitative estimate of the effects on $|M_{fi}|^2$ for a given solid target material may be made. Figure 5(a) and (b) show a plot of $|M_{fi}|^2$ for barium vs. t/τ , where τ is the characteristic time for the radial width of the 4p wavefunction's initial probability distribution to increase to $\sqrt{2}$ of its initial value after ionization [8]. As in reference [8], the matrix element is a function of the parameter κ , which is defined as $\kappa = -k_1 \cos \beta$, with β equal to the angle between the wave vector \mathbf{k}_1 and the vector $\mathbf{r}_1 - \mathbf{r}_2$. In figure 5, lower values of κ are used in generating the curve, ($\kappa = 9.9\text{\AA}^{-1}$ for the 2p case, and 16.2\AA^{-1} for the 3p case), than was used in the Xenon case of reference [8] to reflect the fact that in general, the electrons may have lower energy when incident on the target ion due to the reduced time from photoionization to the first collision. Qualitatively, it may be seen in figure 5a that as t/τ decreases, the value of $|M_{fi}|^2$ will increase, and that the value of $|M_{fi}|^2$ will be greater for an ultraviolet driving laser than for an infrared driving laser. Also, for very small ion separations, the actual time t before collision for the infrared case will move closer to that for the ultraviolet case. In the limiting case of the lowest possible time before collision, the laser wavelength dependence of $|M_{fi}|^2$ would be severely reduced, since the collision time would become primarily a function of the ion spacing, and not

the laser period. However, at this time there are no data for the infrared case in these solid targets to confirm this assertion.

V. Limitations on X-Ray Generation

Previously in section III.B, it was pointed out that the L-shell spectra for gadolinium serve to establish an upper bound for the ability to generate L-shell hollow atom spectra for the laser system used in this study. Figure 3 (a) and (b) show two Gd(L) spectra taken at laser intensities which differ by roughly a factor of 1.6. In case (a), the laser intensity is sufficient to produce the hollow atom spectrum, while in case (b), it is conspicuously absent. As is shown in Table I, a peak laser intensity of approximately $1.4 \times 10^{19} \text{ W/cm}^2$ is required to ionize the entire 4p subshell by ATI theory [14–16], as is given by equation (3),

$$I_{\text{ATI}} (\text{W/cm}^2) = \frac{4 \times 10^9 (I_p (\text{eV}))^4}{Z^2} \quad (3)$$

where I_p is the ionization potential of the electronic state to be ionized, and Z is the charge of the residual ion. This implies that the peak laser intensity must be greater than $1.4 \times 10^{19} \text{ W/cm}^2$.

An estimate of the laser focal intensity can be made from the laser parameters of an average power of 1.5TW and a measured $\sim 5 \mu\text{m}$ focal diameter (approximately twice diffraction limited). These numbers yield an approximate peak focal intensity of $1.5 \times 10^{19} \text{ W/cm}^2$, which is in agreement with the above result. Similarly, the peak laser intensity for figure 3b of $9 \times 10^{18} \text{ W/cm}^2$ is less than the ATI threshold shown in Table I.

A plot may be constructed showing the laser intensities required to produce a hollow-atom L-shell spectrum as a function of atomic number (Z). This plot is shown in Figure 6. The data points for the elements are plotted according to the laser intensity required to ionize the respective 4p subshells. Indicated on the lower half of the plot is the intensity limit of the laser system described in section II. According to the plot, hollow atom L-shell radiation can be produced for heavy atoms up to Gd, allowing for the production of x-ray photon energies of $\sim 6 \text{ keV}$.

Although this range of x-ray production can be extended by increasing the laser intensity by conventional means, it is more advantageous increase the laser intensity by focusing the laser

into an underdense plasma. The laser beam can be made to self-focus, creating a channel in which the laser peak intensity is on the order of 10^{21}W/cm^2 [17]. These channels have been readily observed in gas cluster targets [17,18]. Moreover, recently the authors of reference [19] used a pre-pulse consisting of $\sim 15\%$ of the total laser energy to create an underdense plasma in front of a solid target, allowing the main laser pulse to channel in the plasma. As a result of the increased laser intensity, the authors reported observing up to 2.5MeV photons produced by Bremsstrahlung as a result of the increased kinetic energy of the ponderomotively driven electrons. Alternatively, the solid target could be positioned behind a suitable gas cluster target (Kr or Xe) in order to form a channel before the solid target. Utilization of either of these techniques could increase the laser intensity by 2 orders of magnitude, thus allowing for the generation of hollow atom L-shell spectra as energetic as 15keV from a Uranium target, as is shown in Figure 6.

VI. Conclusion

In this paper we have demonstrated the generation of L-shell radiation with energies in excess of 5keV from Ba and Gd targets with efficiencies on the order of 1%. The mechanism attributed to this high efficiency is an inner-shell selective collisional ejection process in which the laser energy is coupled into the target at a rate in excess of 1W/atom. The two Gd(L) spectra shown provide direct support for this theory of collisional ejection when correlated with the ionization potentials for the Gd 4p electrons. Finally, this paper provides a means of predicting the ability to produce L-shell spectra from highly ionized plasmas as a function of laser intensity, and describes a simple method for producing hard x-rays from elements spanning the periodic table up to and beyond 15keV U(L) radiation.

VII. Acknowledgements

Support for this research was partially provided under contracts with the Army Research Office (DAAG55-97-1-0310), and Sandia National Laboratories and the United States Department of Energy (DE-AC04-94AL85000 and BB9131). Sandia is a multi-program laboratory operated by Sandia Corporation, a Lockheed Martin company, for the United States Department of Energy under contract DE-AC04-94AL85000. A. McPherson is supported by the United States Department of Energy, Office of Science, under contract #W-31-109-ENG-38.

References

1. McPherson A., Thompson B.D., Borisov A.B., Boyer K. and Rhodes C.K.: Multiphoton-induced x-ray emission at 4-5keV from Xe atoms with multiple core vacancies. Nature 370:631-634, 1994.
2. McPherson A., Luk T.S., Thompson B.D., Borisov A.B., Shiryaev O.B., Chen X., Boyer K. and Rhodes C.K.: Multiphoton-induced x-ray emission from Kr clusters on M-shell ($\sim 100\text{\AA}$) and L-shell ($\sim 6\text{\AA}$) transitions. Physical Review Letters 72:1810-1813, 1994.
3. McPherson A., Boyer K. and Rhodes C.K.: X-ray superradiance from multiphoton excited clusters. Journal of Physics B 27:L637-L641, 1994.
4. Ditmire T., Patel P.K., Smith R.A., Wark J.S., Rose S.J., Milathianaki D., Marjoribanks R.S. and Hutchinson M.H.R.: keV x-ray spectroscopy of plasmas produced by the intense picosecond irradiation of a gas of Xenon clusters. Journal of Physics B 31:2825-2831, 1998.
5. Ditmire T., Donnelly T., Falcone R.W. and Perry M.D.: Strong x-ray emission from the high temperature plasmas produced by intense irradiation of clusters. Physical Review Letters 75:3122-3125, 1995.
6. Kondo K., Borisov A.B., Jordan C., McPherson A., Schroeder W.A., Boyer K. and Rhodes C.K.: Wavelength dependence of multiphoton-induced Xe(M) and Xe(L) emissions from Xe clusters. Journal of Physics B 30:2707-2716, 1997.
7. Schroeder W.A., Omenetto F.G., Borisov A.B., Longworth J.W., McPherson A., Jordan C., Boyer K., Kondo K. and Rhodes C.K.: Pump laser wavelength-dependent control of the efficiency of kilovolt x-ray emission from atomic clusters. Journal of Physics B 31:5031-5051, 1998.
8. Schroeder W.A., Nelson T.R., Borisov A.B., Longworth J.W., Boyer K. and Rhodes C.K.: An efficient, selective collisional ejection mechanism for inner-shell population inversion in laser-driven plasmas. Submitted Journal of Physics B.
9. Omenetto F.G., Boyer K., Longworth J.W., McPherson A., Nelson T.R., Schroeder W.A., Rhodes C.K., Marowsky G. and Szamtari S.: High brightness terawatt KrF* (248nm) system. Applied Physics B 64:643-646, 1997.
10. Nelson T.R., Schroeder W.A., Rhodes C.K., Omenetto F.G. and Longworth J.W.: Short pulse amplification at 745nm in Ti:Sapphire with a continuously tunable regenerative amplifier. Applied Optics 36: 7752-7755, 1997.
11. Cowan, R.D.: The Theory of Atomic Structure and Spectra. Berkeley, CA, University of California Press, 1981.
12. Tsuda N. and Yamada J.: Physical properties of dense plasma produced by XeCl excimer laser in high-pressure Argon gases. Jap. J. Applied Physics Part 1 38:3712-3715, 1999.
13. Ditmire T., Springate E., Tisch J.W.G., Shao Y.L., Mason M.B., Hay N., Marangos J.P. and Hutchinson M.H.R.: Explosion of atomic clusters heated by high intensity femtosecond laser pulses. Physical Review A 57:369-382, 1998.
14. Protopapas M., Keitel C.H. and Knight P.L.: Atomic physics with super-high intensity lasers. Rep. Prog. Phys. 60:389, 1997.
15. Ammosov M.V., Delone N.B. and Krainov V.P.: Tunnel ionization of complex atoms and atomic ions in electromagnetic field. Sov. Phys. - JETP 64:1191, 1986.
16. Carlson T.A., Nestor C.W. Jr., Wasserman N. and McDowell J.D.: Calculated ionization potentials for multiply charged ions. Atomic Data 2:63-99, 1970.

17. Borisov A.B., Longworth J.W., Boyer K. and Rhodes C.K.: Stable relativistic/charge displacement channels in ultrahigh power density ($\sim 10^{21} \text{W/cm}^3$) plasmas. Proc. Natl. Acad. Sci. USA 95:7854-7859, 1998.
18. Borisov A.B., McPherson A., Thompson B.D., Boyer K. and Rhodes C.K.: Ultra-high power compression for x-ray amplification – multiphoton cluster excitation combined with nonlinear channeled propagation. Journal of Physics B. 28:2143–2158, 1995.
19. Gahn C., Pretzler G., Saemann A., Tsakiris G.D., Witte K.J., Gassmann D., Schätz T., Schramm U., Thirolf P. and Habs D.: MeV gamma-ray yield from solid targets irradiated with fs-laser pulses. Applied Physics Letters 73:3662-3664, 1998.
20. Ditmire T., Donnelly T., Rubenchik A.M., Falcone R.W., and Perry M.D.: Interaction of intense laser pulses with atomic clusters. Physical Review A 55:3379 – 3402, 1996.
21. McGuire E.J.: Scaled electron ionization cross sections in the Born approximation. Physical Review A. 16:73 – 79, 1977.

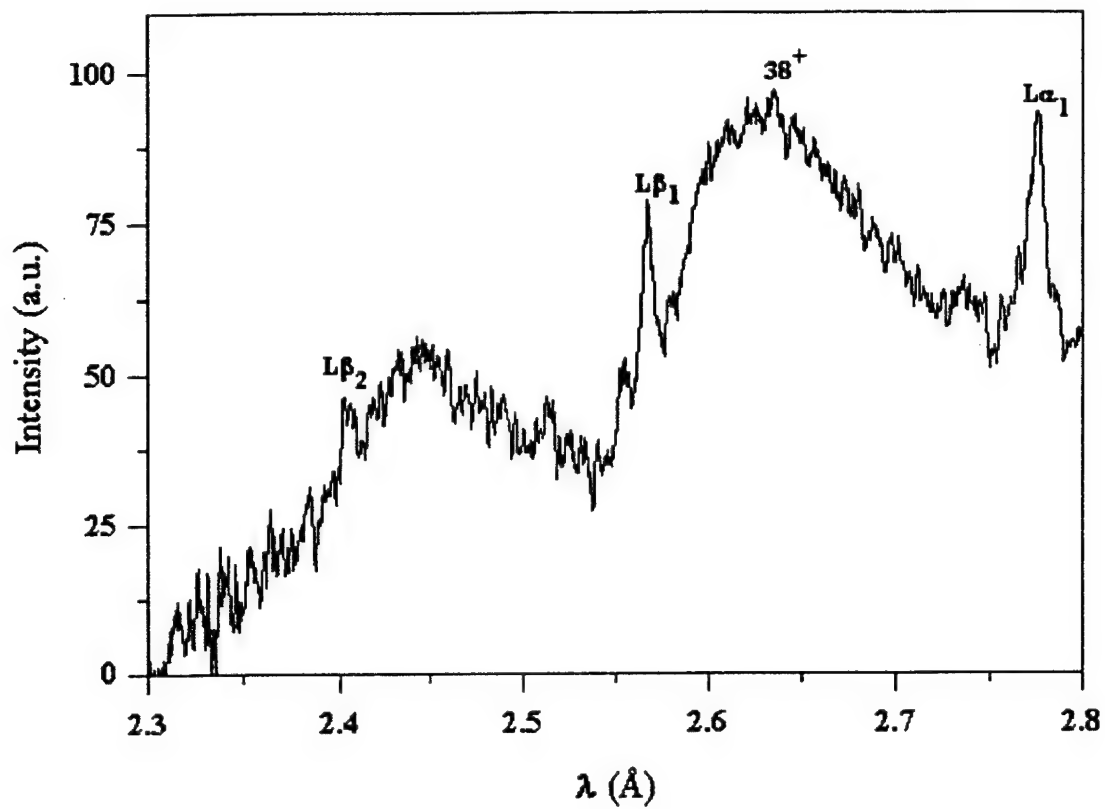


Figure 1

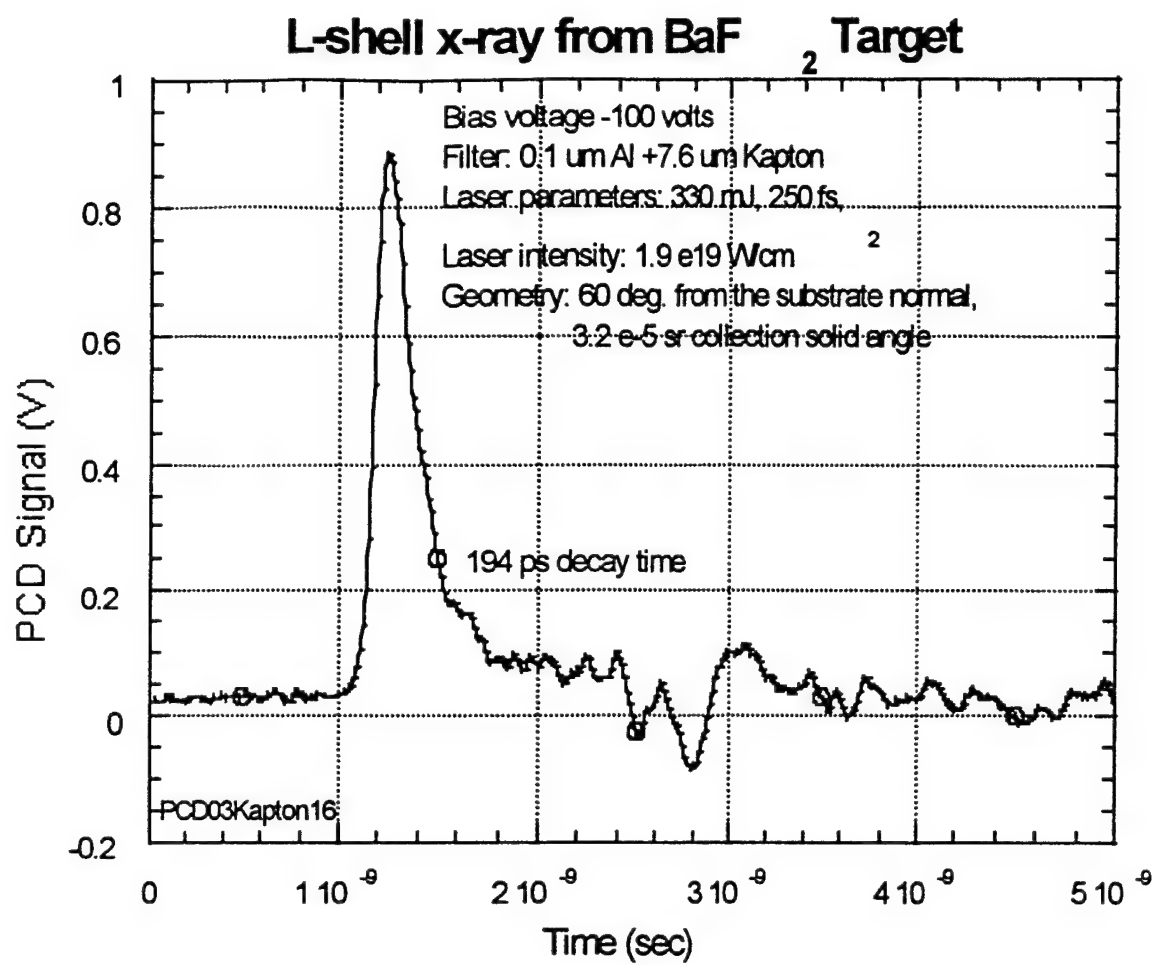


Figure 2

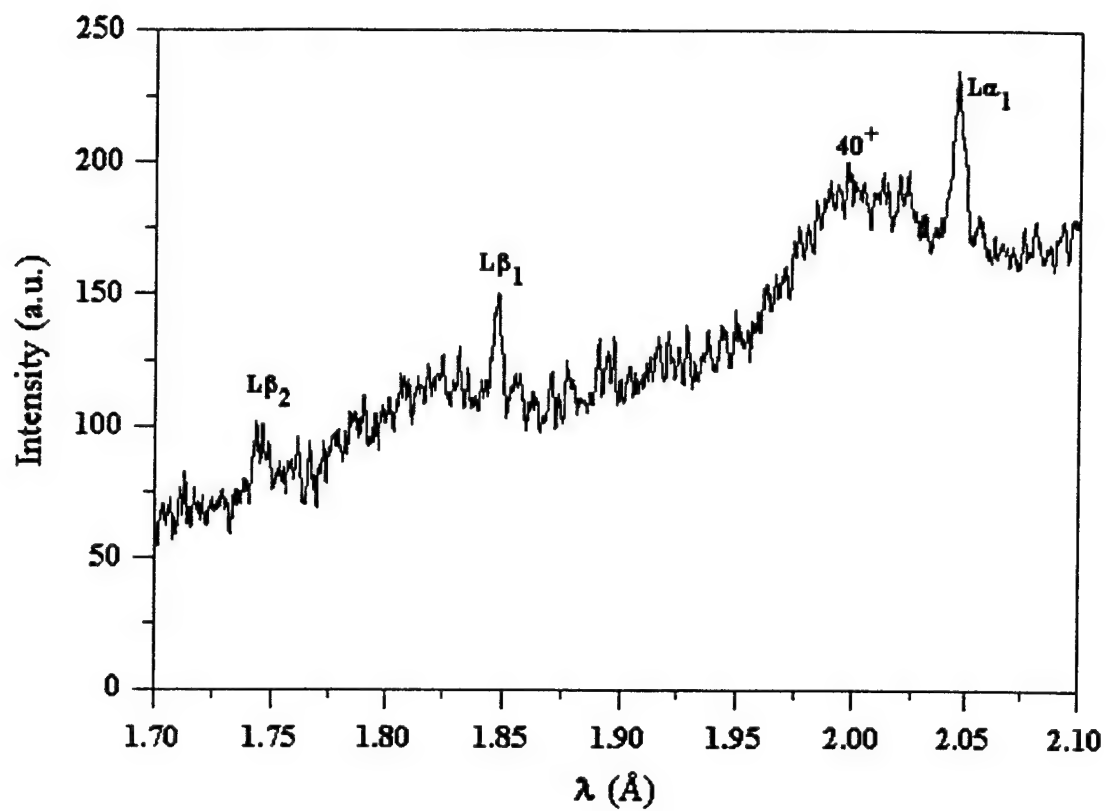


Figure 3a

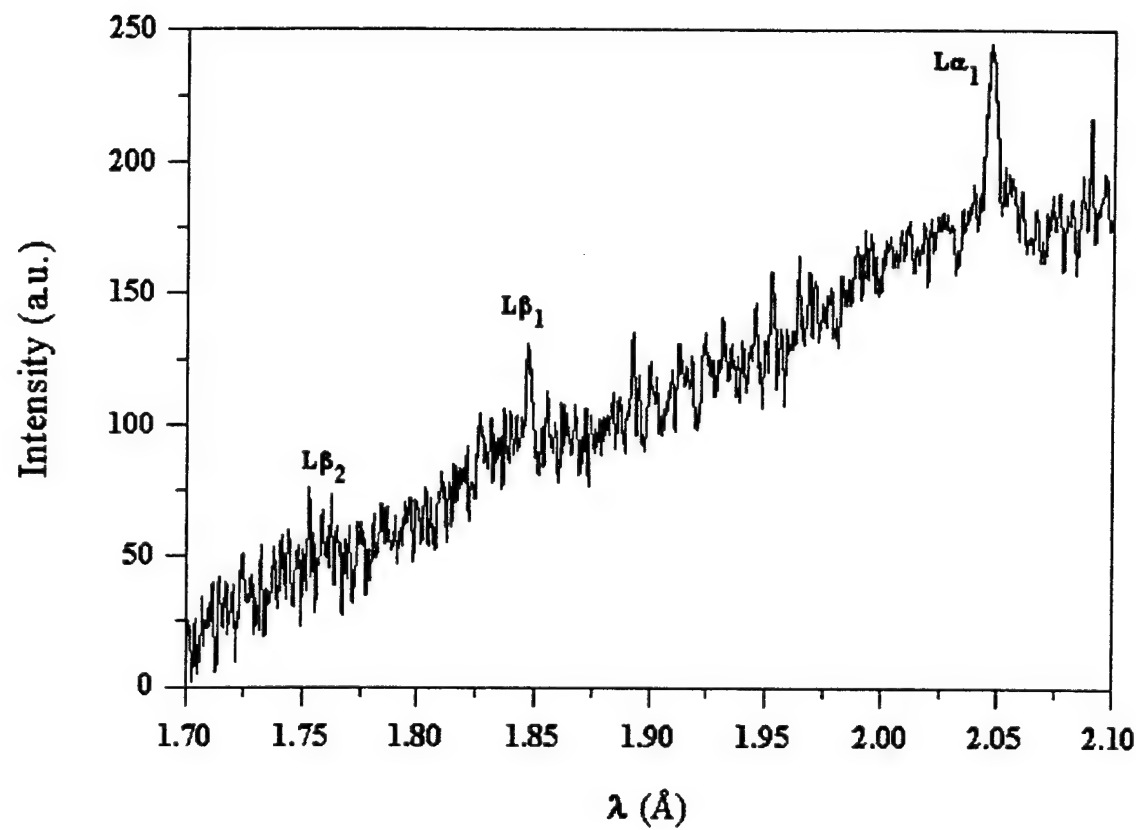


Figure 3b

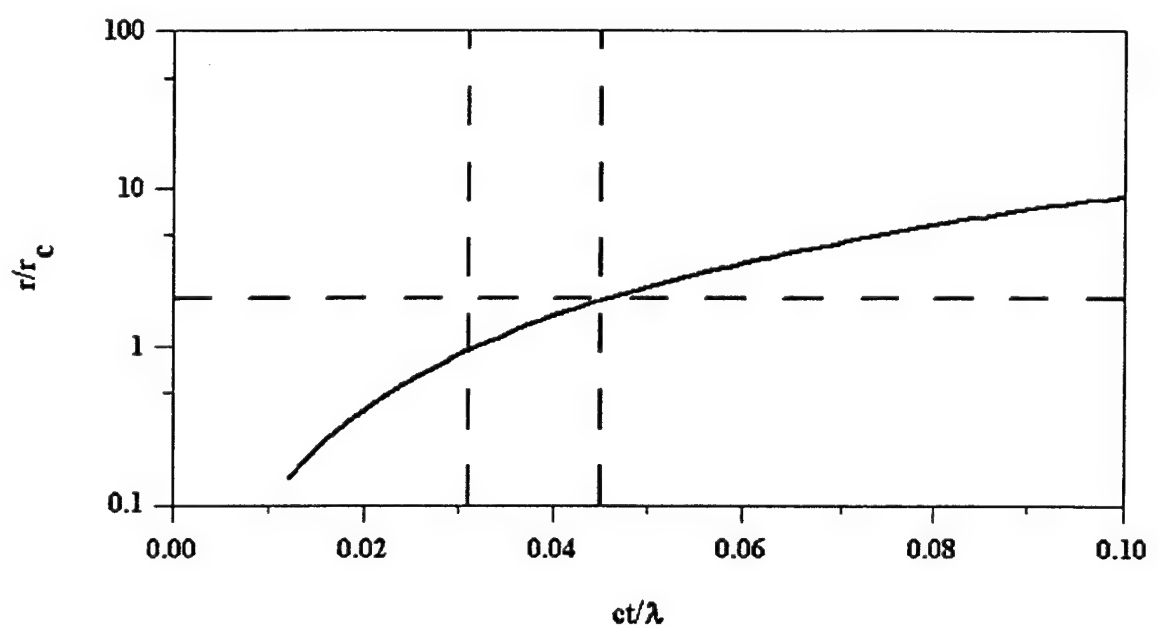


Figure 4a

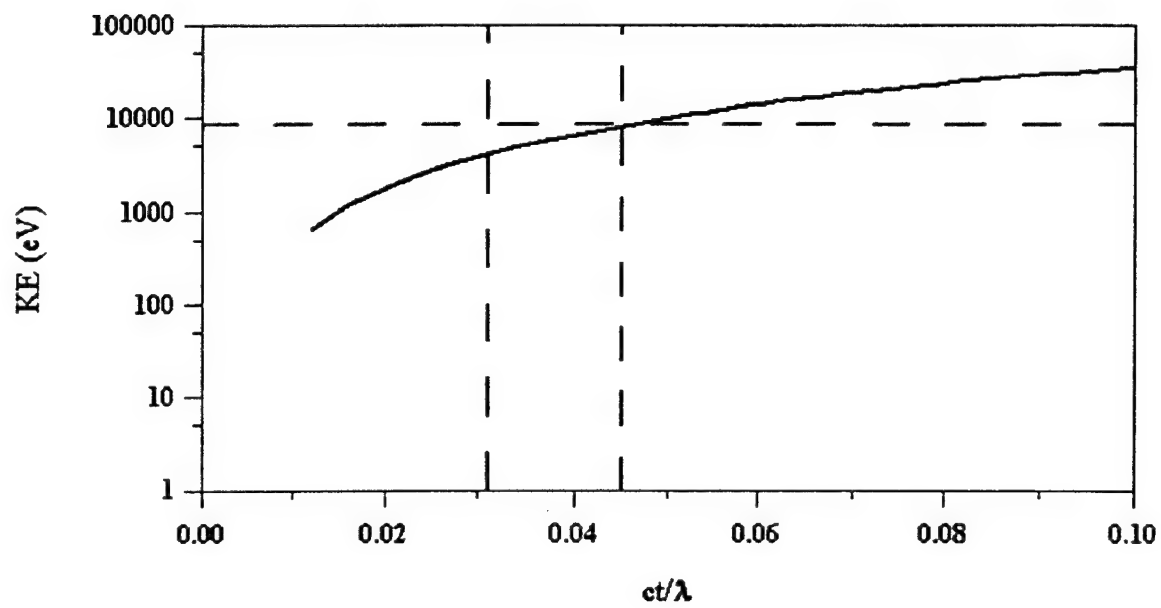


Figure 4b

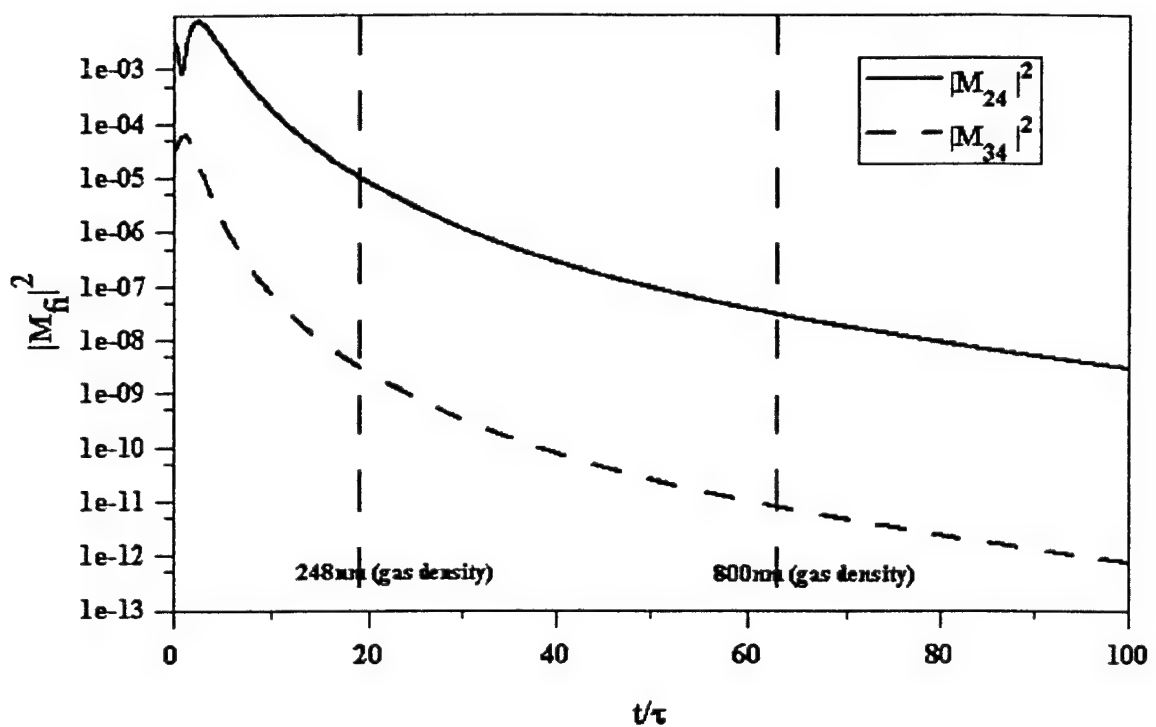


Figure 5a

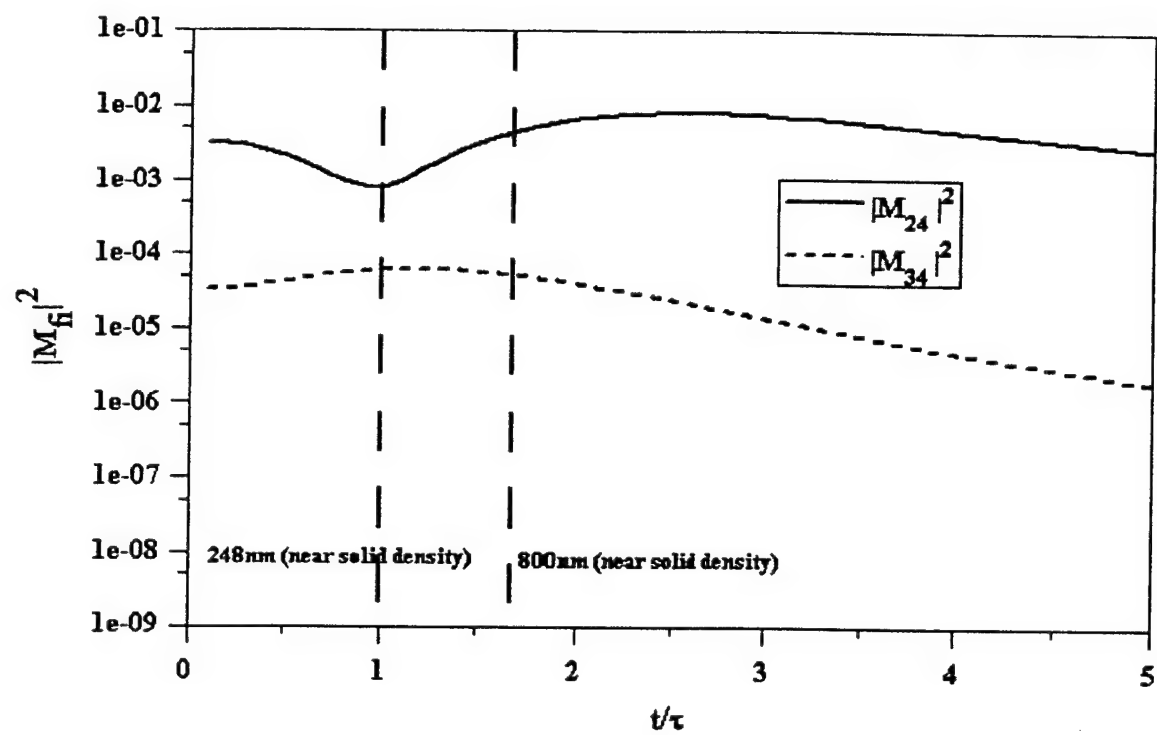


Figure 5b

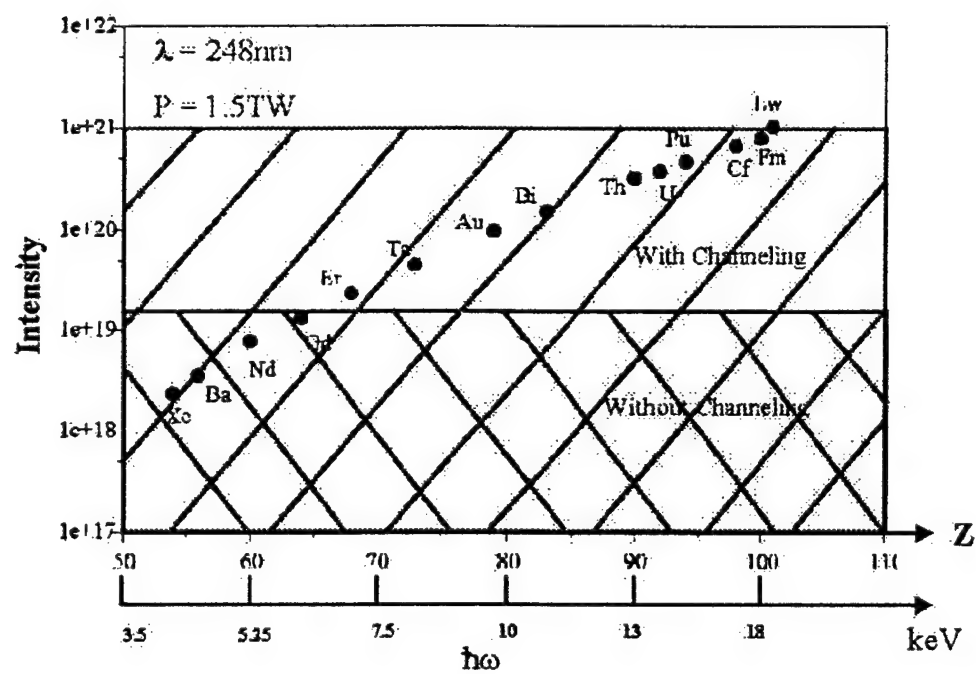


Figure 6

Material	Ionization Potential I_p (eV) For 4p electrons	Charge State	I_{ATT} (W cm ⁻²)
Ba	~ 670 - 880	$20^+ - 25^+$	4×10^{18}
Gd	~ 1100 - 1400	$28^+ - 33^+$	1.4×10^{19}
Ta	~ 1700 - 2100	$37^+ - 42^+$	4.4×10^{19}
Au	~ 2300 - 2700	$43^+ - 48^+$	9×10^{19}
U	~ 3700 - 4350	$56^+ - 61^+$	3.7×10^{20}

Table I

Figure Captions

Figure 1.

High charge state Ba(L) plasma spectrum with characteristic lines from weakly ionized ($< \sim 10^+$) Ba, produced by intense irradiation (10^{19} W/cm 2) of a BaF₂ target. The maximum intensity peak results from charge states as high as of 38⁺.

Figure 2.

Diamond PCD signal of the L-shell radiation from BaF₂. The trace shows a rise time of ~ 150 ps, which is the response time for the detector. The detector has a calibration of 160 μ A/W, which corresponds to 5.6mJ/V for the trace shown here, assuming a 2π radiation distribution. This yields a total energy of ~ 4.9 mJ of energy,

Figure 3

- (a.) High charge state Gd(L) plasma spectrum with characteristic lines from weakly ionized ($< \sim 10^+$) Gd ions, produced by intense irradiation (10^{19} W/cm 2) of a 100 μ m thick Gd foil.
- (b.) Gd(L) characteristic line spectrum only with a background due to Bremsstrahlung radiation, produced by peak laser intensities a factor of 0.6 less than figure 3(a).

Figure 4.

- (a.) Electron displacement vs. normalized laser period (ct/λ) for 248nm. Results are for the fully relativistic numerical simulation of the kinematic motion of an electron for an intensity of $I = 10^{19}$ W/cm 2 under the influence of the electric and magnetic fields

of 248nm (UV) radiation. Data is taken from Reference [7] by permission. Plot is in units of radius for a cluster of 13 Xe atoms ($r_c \approx 5.3\text{\AA}$). The horizontal line indicates $r/r_c = 2$, and the vertical lines indicate the points in the laser period where the electron reaches displacements of $r/r_c = 1$ and $r/r_c = 2$.

(b.) Electron Kinetic Energy vs. normalized laser period (ct/λ) for 248nm. Horizontal line corresponds to 8500eV, the approximate ionization potential for a 2p electron in Ba. The vertical lines in both plots indicate the times at which an electron reaches $r/r_c = 1$, and 2.

Figure 5.

Plot of $|M_{fi}|^2$ for Ba.

(a.) The long dashed vertical lines correspond to 248nm ($t/\tau = 19$) and 800nm ($t/\tau = 63$) laser illumination for a gas cluster target, illustrating the values of $|M_{fi}|^2$ for the case of the upper limit ($\sim 100\text{\AA}$) on the ion spacing.

(b.) The long dashed lines correspond to 248nm($t/\tau = 1$) and 800nm($t/\tau = 1.67$) laser illumination for the case where the average ion spacing is twice the lattice spacing, illustrating the lower limit ($\sim 5\text{\AA}$) on the ion separation. As can be seen, the wavelength dependence would be much less severe in this limit.

Figure 6.

Plot of required laser intensities to generate hollow atom L-shell spectrum for various elements. The second horizontal axis shows the photon energy for L-shell radiation from the respective elements.

Table I.

Ionization potentials and required laser intensities to ionize the $4p$ electrons by above threshold ionization (ATI) in various solid elements.